THE BELL SYSTEM
TECHNICAL JOURNAL

DEVOTED TO THE SCIENTIFIC AND ENGINEERING
ASPECTS OF ELECTRICAL COMMUNICATION

Volume 55 September 1976 Number 7

Traffic Capacity of a Probability-Engineered Trunk Group

By D. W. HILL and S. R. NEAL

(Manuscript received January 22, 1976)

The grade of service of a probability-engineered trunk group is defined to be the 20-day average blocking during the busy hour of the busy season. In this paper, an improved model for calculating grade of service is developed and used to increase the accuracy of the existing trunk-engineering procedures. Using the new model, new traffic-capacity tables and trunk-estimation algorithms have been designed for use in the Bell System.

I. INTRODUCTION

The grade of service for a probability-engineered trunk group is defined to be the average blocking observed in the time-consistent busy hour of the busy season.* The existing methods for predicting grade of service do not account for the effects of the finite length of the individual one-hour measurement intervals and thereby tend to underestimate trunk-group capacity.

In this paper, we develop an improved model for calculating average blocking that includes the two essential effects of the finite measurement interval. First, the current method for estimating the mean blocking for a single hour must be revised to remove an implicit assumption that the measurement interval is infinite. Second, the existing mathematical model for day-to-day variation of trunk-group

* Both the CCITT (International Telegraph and Telephone Consultative Committee) and the Bell System define grade of service as an unweighted average of busy-hour busy-season blocking values.

offered loads must be modified to account for statistical measurement error, which is also introduced by the finite measurement interval.

We develop a new model of day-to-day load variation in Appendix A and in Section II combine it with a new estimate of mean single-hour blocking to obtain our approximation for the average blocking. This new approximation is then compared with the existing approximation analytically and numerically; the accuracy of the new approach is established in the third section using data from a computer simulation. A summary is given in the last section.

II. AVERAGE BLOCKING

In this section, we develop an approximation for the average busy-season busy-hour blocking. Since the measured grade of service is determined from blocking measurements made over several hours, and since the busy-hour source loads vary from day to day, our analysis must account for the effects of such load variation. Accordingly, we first discuss day-to-day load variation and then describe our approximation for average blocking.

2.1 Day-to-day load variation

R. I. Wilkinson was the first author to study the impact of day-to-day variation in offered loads on trunk-engineering procedures.[1,2] He collected data from a number of trunk groups that indicated that the distribution of the observed loads could be approximated by a gamma distribution. The data also indicated that the variance, Var $(\hat{a})$, of the observed load, $\hat{a}$, was related to the mean $\bar{a}$ by

$$\text{Var}\ (\hat{a}) = 0.13\bar{a}^{\phi}, \tag{1}$$

where ϕ is a parameter whose value depends on local conditions.

Wilkinson's studies showed that Var $(\hat{a})$ tends to be relatively larger for overflow traffic than for first-routed (Poisson) traffic. Those results led to the specification of three values of ϕ (1.5, 1.7, and 1.84) to cover a reasonable range of engineering applications. The *level* of day-to-day variation is called low when $\phi = 1.5$ is appropriate, medium for $\phi = 1.7$, and high when $\phi = 1.84$.

In Appendix A, we show that the variance of the observed "single-hour" offered loads is a sum of two components:

$$\text{Var}\ (\hat{a}) = \frac{2\bar{a}z}{(t/h)} + \text{Var}\ (\alpha), \tag{2}$$

where α is the daily source load (a random variable), $\hat{a}$ is the observed load, $\bar{a} = E(\alpha)$ is the average busy-season load, z is the traffic peakedness, t is the observation interval (usually one hour), and h is the

mean holding time. The first term is an approximation for the variance arising from the finite measurement interval* and Var (α) is the variance of the daily source load.

Combining eqs. (1) and (2), we obtain a model relating the source-load variation to the observed load variation; i.e.,

$$\text{Var } (\alpha) = 0.13\bar{\alpha}^{\phi} - \frac{2\bar{\alpha}z}{(t/h)}. \tag{3}$$

For certain combinations of the various parameters, $2\bar{\alpha}z/(t/h)$ can exceed $0.13\bar{\alpha}^{\phi}$, indicating that the observed load variation is entirely due to random measurement error resulting from the finite measurement interval. For our application, we will assume that

$$\text{Var } (\alpha) = \max\left\{0,\ 0.13\bar{\alpha}^{\phi} - \frac{2\bar{\alpha}z}{(t/h)}\right\}. \tag{4}$$

2.2 The approximation

Consider a service system with c servers having exponentially distributed service times with mean h and serving traffic under a blocked-calls-cleared service discipline. The system is observed during n disjoint measurement intervals $I_1, \cdots, I_n$, each of length t. During I_k, the interarrival times are independent and identically distributed (iid) with mean $1/\lambda_k$. The peakedness, z, of the traffic is assumed to be the same during all the intervals.† The system is in statistical equilibrium during each interval and the initial point of each interval is a stationary (random) point for the arrival process. The loads $\alpha_i = \lambda_i h$, $i = 1, \cdots, n$, are independent and identically distributed according to the distribution function $\Gamma(\alpha|\bar{\alpha}, v_d)$ with mean $\bar{\alpha}$ and variance $v_d = \text{Var } (\alpha)$ (the day-to-day source-load variance). [We assume that $\Gamma(\alpha|\bar{\alpha}, v_d)$ is a gamma distribution. Justification for the assumption is given below.]

We use $A_j(t)$ and $O_j(t)$ to denote, respectively, the number of arrivals (call attempts) and the number of blocked attempts (the overflows) during I_j; the (measured) observed blocking is $B_j = O_j(t)/A_j(t)$ provided $A_j(t) \neq 0$. If $A_j(t) = 0$, then $O_j(t) = 0$ and the ratio is not defined. However, if no arrivals occur during I_j, it seems appropriate to say that no blocking occurred; i.e., we define $B_j = 0$ whenever $A_j(t) = 0$. The sample average of the observed blocking (the observed grade of service) is

$$\bar{B}_n = \frac{1}{n}\sum_{j=1}^{n} B_j.$$

* This is an extension of the formula given by Riordan in Ref. 3.

† Traffic studies have shown that the peakedness of the traffic offered to a final trunk group does not change significantly from day to day during the busy hour of the busy season.

Since $\alpha_1, \cdots, \alpha_n$ are iid, $B_1, \cdots, B_n$ are also iid. Consequently, the average blocking $\bar{B}$ is given by

$$\bar{B} = E(\bar{B}_n) = E(B_1). \tag{5}$$

The hourly measurement B_1 represents a random sample of observed blocking corresponding to a load population with mean α_1. The parameter α_1 is a random variable with mean $\bar{\alpha}$ and distributed according to $\Gamma(\alpha_1 | \bar{\alpha}, v_d)$. Thus,

$$\bar{B} = \int_0^\infty E\left\{ \frac{O_1(t)}{A_1(t)} \middle| \alpha_1 \right\} d\Gamma(\alpha_1 | \bar{\alpha}, v_d). \tag{6}$$

Dropping the subscripts, the conditional mean in (6) is given by

$$E\left\{ \frac{O(t)}{A(t)} \middle| \alpha \right\} = \Pr\{A(t) > 0 | \alpha\} E\left\{ \frac{O(t)}{A(t)} \middle| \alpha, A(t) > 0 \right\},$$

where $\Pr(X)$ denotes the probability of the event X. Let $\bar{A} = E\{A(t) | \alpha\}$ and $\bar{O} = E\{O(t) | \alpha\}$. Also, for nonnegative m and n,

$$E\{[O(t)]^m [A(t)]^n | \alpha, A(t) > 0\} = \frac{E\{[O(t)]^m [A(t)]^n | \alpha\}}{\Pr\{A(t) > 0 | \alpha\}}.$$

Using these relations, an approximation for the conditional expectation is obtained by expanding the function x/y in a two-dimensional Taylor Series about the point $(x_0, y_0) = (E\{O(t) | \alpha, A(t) > 0\}, E\{A(t) | \alpha, A(t) > 0\})$. Taking the appropriate conditional expectation and retaining only the terms up through second order, we have the approximation

$$\begin{aligned} E\left\{ \frac{O(t)}{A(t)} \middle| \alpha, A(t) > 0 \right\} \approx{} & \frac{\bar{O}}{\bar{A}} + \frac{\bar{O}}{\bar{A}} \left(\frac{\Pr\{A(t) > 0 | \alpha\}}{\bar{A}} \right)^2 \\ & \cdot \left[\frac{E\{[A(t)]^2 | \alpha\}}{\Pr\{A(t) > 0 | \alpha\}} - \left(\frac{\bar{A}}{\Pr\{A(t) > 0 | \alpha\}} \right)^2 \right] \\ & - \left(\frac{\Pr\{A(t) > 0 | \alpha\}}{\bar{A}} \right)^2 \\ & \cdot \left(\frac{E\{A(t) O(t) | \alpha\}}{\Pr\{A(t) > 0 | \alpha\}} - \frac{\bar{A}\bar{O}}{(\Pr\{A(t) > 0 | \alpha\})^2} \right). \end{aligned} \tag{7}$$

Denoting the call congestion $\bar{O}/\bar{A}$ by $B(c, \alpha, z)$ and noting that $E\{A(t) | \alpha\} = \alpha t/h$, eq. (7) reduces to

$$\begin{aligned} E\left\{ \frac{O(t)}{A(t)} \middle| \alpha, A(t) > 0 \right\} \approx{} & B(c, \alpha, z) + \frac{\Pr\{A(t) > 0 | \alpha\}}{(\alpha t/h)^2} \\ & \cdot [B(c, \alpha, z) \operatorname{Var}\{A(t) | \alpha\} - \operatorname{Cov}\{A(t), O(t) | \alpha\}], \end{aligned}$$

where all of the statistical moments are functions of α, z, and c. Thus,

$$E\left\{\frac{O(t)}{A(t)}\middle|\alpha\right\} \approx \Pr\{A(t) > 0|\alpha\}B(c, \alpha, z) + \left(\frac{\Pr\{A(t) > 0|\alpha\}}{\alpha t/h}\right)^2 \cdot [B(c, \alpha, z) \operatorname{Var}\{A(t)|\alpha\} - \operatorname{Cov}\{A(t), O(t)|\alpha\}]. \quad (8)$$

Formulas for computing the moments are given in Ref. 4. An expression for $\Pr\{A(t) > 0|\alpha\}$ is given in Appendix B. Numerical experimentation has shown that $\Pr\{A(t) > 0|\alpha\} \approx 1$ for $\alpha t/h > 10$; i.e., that term can be ignored except for very small loads or short measurement intervals. Combining eqs. (6) and (8), we have

$$\bar{B} \approx \int_0^\infty \Pr\{A(t) > 0|\alpha\}B(c, \alpha, z)d\Gamma(\alpha|\bar{\alpha}, v_d) + \int_0^\infty R(c, \alpha, z)d\Gamma(\alpha|\bar{\alpha}, v_d), \quad (9)$$

where

$$R(c, \alpha, z) = \left(\frac{\Pr\{A(t) > 0|\alpha\}}{\alpha t/h}\right)^2 \cdot [B(c, \alpha, z) \operatorname{Var}\{A(t)|\alpha\} - \operatorname{Cov}\{A(t), O(t)|\alpha\}].$$

The approximation is complete when Γ is specified.

Numerical experimentation has shown that $\bar{B}$ is not very sensitive to the shape of $\Gamma(\alpha|\bar{\alpha}, v_d)$ for fixed values of $\bar{\alpha}$ and v_d. Accordingly, following Refs. 1 and 2, we have assumed that $\Gamma(\alpha|\bar{\alpha}, v_d)$ is a gamma distribution with mean $\bar{\alpha}$ and variance v_d, where $v_d = \operatorname{Var}(\alpha)$ is given by eq. (4). With these assumptions, the integrals in (9) can be computed numerically using a 51-point compound Simpson's rule. The accuracy of the approximation is discussed in Section III. In Section 2.3, we compare this approximation with the existing procedure.

2.3 The existing procedure

The existing approximation for average blocking is[1,2]

$$\bar{B}_e(c, \bar{\alpha}, z) \approx \int_0^\infty B(c, \alpha, z)d\Gamma(\alpha|\bar{\alpha}, v), \quad (10)$$

where

$$v = \operatorname{Var}(\hat{\alpha}) = 0.13\bar{\alpha}^\phi.$$

Consequently, there are two essential differences between the present method (10) and our approximation (9).

First, the existing method neglects the random component of load variation and assumes that all of the variation in the observed loads is due to day-to-day changes in the source load; i.e., the assumed load variation is too large by an amount $2\bar{\alpha}z/(t/h)$. The integral in (10) is an increasing function of v in the range of engineering interest (less

than 5 percent average blocking) and, hence, $\bar{B}_e$ is larger than it would be if v_d were used in place of v.

Comparing (9) and (10), we see the second difference. The existing procedure implicitly uses $E\{\lceil O(t)/A(t)\rceil | \alpha\} \approx B(c, \alpha, z)$ and neglects the term $R(c, \alpha, z)$. Numerical experimentation has shown that $R(c, \alpha, z)$ is negative in the range of engineering interest and that $|R(c, \alpha, z)|$ is an increasing function of z. For z near 1, $R(c, \alpha, z)$ is negligible. However, for $z \geq 2$ $R(c, \alpha, z)$ becomes significant. Consequently, $B(c, \alpha, z)$ is larger than $E\{\lceil O(t)/A(t)\rceil | \alpha\}$, and the difference increases with z.

The two differences combine to cause $\bar{B} < \bar{B}_e$ in all regions of engineering interest; i.e., the average of the observed single-hour blocking probabilities is less than that predicted by the existing method (10). Quantitative comparisons are made in Section III.

III. NUMERICAL RESULTS

To determine the accuracy of our approximation (6) relative to the existing procedure (10), a computer simulation was constructed for a full-access trunk group satisfying the assumptions specified in Section 2.2. The simulation was run for a large range of the system parameters c, $\bar{\alpha}$, z, and ϕ covering the regions of engineering interest ($B \approx 0.01$, $c \geq 2$, $1 \leq z \leq 7$). Generally, a mean holding time of 180 seconds was used (although both smaller and larger values were used for sensitivity tests)* and 20-day averages were generated. All statistics are based on a sample size of 50; i.e., 1000 simulated hours.

3.1 Simulation output

Typical results from the simulation are summarized in Tables I and II. First consider Table I. The first four columns are the input parameters for the simulation. In order, they are the peakedness z, the offered load $\bar{\alpha}$, the trunk-group size c, and the conventional exponent ϕ defining the level of day-to-day variation. [That is, Var (α) was adjusted so as to produce the desired ϕ, as discussed in Section 2.2.] The next three columns give the simulated 20-day average blocking $\bar{B}_o$, the variance v_α of the daily offered source loads, and the (total) variance $v_{\hat{\alpha}}$ of the observed loads. The measurement variance $v_{\tilde{\alpha}}$ is then computed as $v_{\tilde{\alpha}} = v_{\hat{\alpha}} - v_\alpha$, and is compared with $2\bar{\alpha}z/(t/h)$ in the last two columns. In the cases shown, $2\bar{\alpha}z/(t/h)$ is an adequate approximation of the variance introduced by a finite measurement interval. The other

* The holding time was varied from 100 to 360 seconds and a small effect was observed. The effect is negligible for most engineering applications. Based on a survey of observed holding times, AT&T has requested that $h = 225$ seconds be used for the new traffic tables.

Table I — Simulation results

Simulation Input				Observed Data				
Peakedness (z)	Mean Load ($\bar{\alpha}$)	Trunks (c)	Variation Parameter (ϕ)	Average Blocking ($\bar{B}_o$)	Input Variance (v_α)	Observed Variance ($v_{\hat{\alpha}}$)	Residual Variance ($v_{\tilde{\alpha}}$)	Theoretical Variance $\left(\frac{2\bar{\alpha}z}{t/h}\right)$
1.0	4.01	10	1.5	0.0083	0.72	1.03	0.31	0.40
4.0	17.80	40	1.5	0.0084	4.81	12.54	7.73	7.12
4.0	9.80	30	1.7	0.0049	3.60	6.61	3.01	3.92
7.0	9.75	40	1.84	0.0046	1.76	8.96	7.10	6.82

test cases indicated that the accuracy of the approximation generally increases as $\bar{\alpha}$ increases (as one would expect from the asymptotic nature of the approximation).

3.2 *Existing approximation*

The data in the first seven columns of Table II illustrate the size of the bias in the existing method. The first five columns of the table are the same as those in Table I. The next column $\bar{B}_e$ represents the computed average blocking corresponding to the source load, peakedness, trunk-group size, and respective day-to-day variance used in the simulation. The next column $\hat{c}_e$ gives the corresponding estimate (using the existing method) of the trunk-group size necessary to achieve the simulated blocking for the given input load, peakedness, and day-to-day variation parameter ϕ.

First, note the difference between $\bar{B}_0$ and $\bar{B}_e$. The existing approximation $\bar{B}_e$ is always larger than the actual average blocking $\bar{B}_o$, and the relative difference increases as z increases. The bias in $\bar{B}_e$ will cause the engineering estimates of trunks required (to meet objective

Table II — Engineering methods

Simulation					Engineering Methods			
Input				Output	Existing Method		New Method	
Peakedness (z)	Mean Load ($\bar{\alpha}$)	Trunks (c)	Variation Parameter (ϕ)	Simulated Average Blocking ($\bar{B}_o$)	Blocking Estimate ($\bar{B}_e$)	Trunk Estimate ($\hat{c}_e$)	Blocking Estimate ($\bar{B}$)	Trunk Estimate ($\hat{c}$)
1.0	4.01	10	1.5	0.0083	0.0100	10.24	0.0078	9.91
4.0	17.80	40	1.5	0.0084	0.0145	42.83	0.0083	39.97
4.0	9.80	30	1.7	0.0049	0.0103	32.96	0.0054	30.31
7.0	9.75	40	1.84	0.0046	0.0106	44.71	0.0045	39.93

service) to be too large. The bias in the trunk estimates is illustrated by comparing c with $\hat{c}_e$.*

In all the cases we considered, the bias was primarily a function of z. For $z = 1$, the bias was generally less than one trunk. For $z = 2$, $\hat{c}_e - c$ was usually between one and two trunks, and, for $z = 4$, the bias ranged between three and five trunks. The corresponding relative errors $(c - \hat{c}_e)/c$ were largest at the smaller values of c.

3.3 New approximation

The relative accuracy of the new approximation is illustrated in the last two columns of Table II. In these cases, the new approximation for $\bar{B}$ is much closer to the simulated blocking $\bar{B}_o$. The relative differences are quite small, especially when compared with the corresponding errors in the existing approximation. Since the estimate of $\bar{B}$ is good, the corresponding estimate $\hat{c}$ of trunks required to achieve $\bar{B}_o$ is quite close to c, the number actually required.

Similar results were obtained in all the other test cases. Accordingly, we conclude that the existing approximation (10) is biased, but the bias is essentially removed by using the new approximation (9).

Based on these results, the new approximation has been used to generate new trunk-engineering tables and algorithms for use by the Bell System.

IV. SUMMARY AND CONCLUSIONS

By combining a new model for day-to-day load variation with a new estimate of mean single-hour blocking, a new approximation was obtained for estimating the grade of service for probability-engineered trunk groups. Using this result, it has been possible to improve the accuracy of the presently recommended trunk-engineering procedures and thereby realize an increase in predicted trunk-group capacities. The increases are smaller for trunk groups serving Poisson traffic, but become substantial as the peakedness and level of day-to-day variation increase. The new approximation has been used to develop new trunk-engineering tables and algorithms that will soon be introduced into the Bell System.

APPENDIX A

Day-to-Day Load Variation

Let S denote a $GI/M/\infty$ service system which is observed over k disjoint intervals of time $\{I_1, \cdots, I_k\}$, each of length t.† The inter-

* Refer to Section 2.3 for a discussion of the individual components of the difference.
† The infinite server system is a standard model for traffic engineering. It is used to characterize a traffic process in terms of only interarrival times and service times.

arrival times during I_j are independent and identically distributed (iid) according to the probability distribution function F_j with mean

$$\frac{1}{\lambda_j} = \int_0^\infty t dF_j(t).$$

The arrival rates $\{\lambda_1, \cdots, \lambda_k\}$ are iid with mean $E(\lambda)$ and variance Var (λ). The peakedness (variance-to-mean ratio) of the arrival process is constant for all intervals. The service times are iid according to a negative-exponential distribution with mean h. The system is assumed to be operating in statistical equilibrium at the beginning of each interval; i.e., the initial point of each interval is a stationary point for the arrival process (see Ref. 3).

Let N_j be the number of arrivals during I_j and let ξ_{ij} denote the service time of the ith arrival in I_j. The average usage during $I = \sum_{j=1}^{k} I_j$ is estimated by*

$$\hat{u}_k = \frac{1}{k} \sum_{j=1}^{k} \sum_{i=1}^{N_j} \xi_{ij}. \tag{11}$$

(We assume the edge effects are negligible since S is in equilibrium during each interval I_j.) The corresponding estimate of average offered load is

$$\hat{a}_k = \frac{1}{t} \hat{u}_k. \tag{12}$$

In this section, we obtain the mean and variance of $\hat{a}_k$.

From Ref. 5 and eqs. (11) and (12), we have

$$\begin{aligned} E(\hat{a}_k) &= \frac{1}{kt} \sum_{j=1}^{k} \underset{N_j}{E} \left\{ E \left\{ \sum_{i=1}^{N_j} \xi_{ij} | N_j \right\} \right\}, \\ &= \frac{1}{kt} \sum_{j=1}^{k} \underset{N_j}{E} \{hN_j\} \\ &= \frac{h}{kt} \sum_{j=1}^{k} E\{N_j\}. \end{aligned} \tag{13}$$

Since the beginning of each interval is a stationary point for the arrival process, it follows that $E\{N_j | \lambda_j\} = \lambda_j t$ (see Ref. 6). Thus, for the arrival process, it follows that

$$\begin{aligned} E\{N_j\} &= \underset{\lambda_j}{E} \{E\{N_j | \lambda_j\}\} \\ &= \underset{\lambda_j}{E} \{\lambda_j t\} \\ &= E\{\lambda\} t \end{aligned}$$

* Our studies have shown that the additional measurement variance caused by discretely sampling the usage with a 100-second-scan Traffic Usage Recorder was negligible when compared with the variance caused by the load variation.

and so from (13) we have

$$E\{\hat{\alpha}_k\} = E\{\lambda\}h.$$

Since the ξ_{ij} are independent, eqs. (11) and (12) yield

$$\text{Var}\,(\hat{\alpha}_k) = \frac{1}{(kt)^2}\sum_{j=1}^{k}\text{Var}\left\{\sum_{i=1}^{N_j}\xi_{ij}\right\}, \tag{14}$$

and from Ref. 5,

$$\text{Var}\left\{\sum_{i=1}^{N_j}\xi_{ij}\right\} = \underset{\lambda_j}{E}\left\{\underset{N_j}{\text{Var}}\left\{\sum_{i=1}^{N_j}\xi_{ij}|\lambda_j\right\}\right\} + \underset{\lambda_j}{\text{Var}}\left\{\underset{N_j}{E}\left\{\sum_{i=1}^{N_j}\xi_{ij}|\lambda_j\right\}\right\}. \tag{15}$$

We first expand

$$\begin{aligned}\underset{N_j}{\text{Var}}\left\{\sum_{i=1}^{N_j}\xi_{ij}|\lambda_j\right\} &= \underset{N_j}{\text{Var}}\left\{E\left\{\sum_{i=1}^{N_j}\xi_{ij}|N_j,\lambda_j\right\}\right\} \\ &\qquad + \underset{N_j}{E}\left\{\text{Var}\left\{\sum_{i=1}^{N_j}\xi_{ij}|N_j,\lambda_j\right\}\right\} \\ &= \underset{N_j}{\text{Var}}\{N_jh|\lambda_j\} + \underset{N_j}{E}\{N_jh^2|\lambda_j\} \\ &= h^2\lambda_jt\left(1 + \frac{\text{Var}\{N_j|\lambda_j\}}{E\{N_j|\lambda_j\}}\right).\end{aligned} \tag{16}$$

Let z denote the traffic peakedness (which is constant over I). Then from Ref. 7, we have the approximation

$$\frac{\text{Var}\{N_j|\lambda_j\}}{E\{N_j|\lambda_j\}} \approx 2z - 1; \tag{17}$$

the approximation has been found to be quite good for $\alpha > (z-1)$ and $t \geqq 10h$ (and probably acceptable for engineering purposes for $t \geqq 5h$). Substituting (17) into (16), we obtain

$$\underset{N_j}{\text{Var}}\left\{\sum_{i=1}^{N_j}\xi_{ij}|\lambda_j\right\} = 2zh^2t\lambda_j. \tag{18}$$

Expanding the second term in (15) in the same manner as in eq. (13) yields

$$\underset{N_j}{E}\left\{\sum_{i=1}^{N_j}\xi_{ij}|\lambda_j\right\} = ht\lambda_j. \tag{19}$$

Substituting (18) and (19) in (15) provides

$$\text{Var}\left\{\sum_{i=1}^{N_j}\xi_{ij}\right\} = 2zh^2tE\{\lambda\} + (ht)^2\,\text{Var}\,\{\lambda\}, \tag{20}$$

which, with eq. (14), implies that

$$\text{Var}\,(\hat{\alpha}_k) = \frac{1}{k}\left(\frac{2zhE\{\lambda\}}{t/h} + h^2\,\text{Var}\,\{\lambda\}\right). \tag{21}$$

The offered load during I_j is $\alpha_j = \lambda_j h$. Hence, $E\{\alpha_j\} = hE\{\lambda\}$ and Var $\{\alpha_j\} = h^2$ Var $\{\lambda\}$. Dropping the subscript j, we have

$$\text{Var } \{\hat{\alpha}_k\} = \frac{1}{k}\left(\frac{2zE\{\alpha\}}{t/h} + \text{Var } \{\alpha\}\right). \tag{22}$$

Equation (22) has a simple interpretation. The first term $(2zE\{\alpha\})/(t/h)$ represents the component (of the observed variation) which is due to a finite measurement period. The second component Var $\{\alpha\}$ is the "true" (day-to-day) variation of the offered source load. The factor k results from averaging k observations. Setting $k = 1$ and $\bar{\alpha} = E\{\alpha\}$, we have the variance of the single-hour load estimate

$$\text{Var } \{\hat{\alpha}\} = \frac{2z\bar{\alpha}}{t/h} + \text{Var } \{\alpha\}, \tag{23}$$

where the individual terms have the interpretations noted above.

APPENDIX B

Probability of an Arrival

In this appendix, we derive an expression for Pr $\{A(t) > 0|\alpha\}$. We assume that the interarrival times are independent and identically distributed according to the distribution function F. We further assume that F is a mixture of exponentials, with the parameters chosen so that F approximates the interarrival distribution of an overflow process with load α and peakedness z (see Ref. 8); that is,

$$F(t) = 1 - k_1 e^{-r_1 t} - k_2 e^{-r_2 t}.$$

Now, Pr $\{A(t) > 0|\alpha\}$ is just the probability that the first arrival after a random entry point (i.e., a stationary point for the arrival process) will occur before t units of time have elapsed. Thus, from Ref. 9, we have

$$\begin{aligned}\text{Pr } \{A(t) > 0|\alpha\} &= \alpha \int_0^t [1 - F(x)]dx \\ &= \alpha\left(\frac{k_1}{r_1} + \frac{k_2}{r_2} - \frac{k_1}{r_1} e^{-r_1 t} - \frac{k_2}{r_2} e^{-r_2 t}\right).\end{aligned}$$

Since $\int_0^\infty [1 - F(x)]dx = 1/\alpha$, it follows that

$$\text{Pr } \{A(t) > 0|\alpha\} = 1 - \alpha\left(\frac{k_1}{r_1} e^{-r_1 t} + \frac{k_2}{r_2} e^{-r_2 t}\right),$$

where the parameters k_i and r_i are functions of α and z as specified in Ref. 8.

REFERENCES

1. R. I. Wilkinson, "A Study of Load and Service Variations in Toll Alternate Route Systems," Proc. Second International Teletraffic Congress, The Hague, July 7–11, 1958, Document No. 29.
2. R. I. Wilkinson, "Nonrandom Traffic Curves and Tables for Engineering and Administrative Purposes," Traffic and Operator Services Center, Bell Laboratories, 1970.
3. J. Riordan, "Telephone Traffic Time Averages," B.S.T.J., *30* (October 1951), pp. 1129–1144.
4. S. R. Neal and A. Kuczura, "The Accuracy of Call-Congestion Measurements for Loss Systems with Renewal Input," B.S.T.J., *51* (December 1972), pp. 2197–2208.
5. H. H. Panjer, "On the Decomposition of Moments by Conditional Moments," Amer. Statist., *27* (October 1973), pp. 170–171.
6. J. M. Hammersley, discussion of paper by W. L. Smith, "Renewal Theory and Its Ramifications," J. Roy. Statist. Soc., Ser-B, *20* (1958), pp. 289–295.
7. D. L. Jagerman, "Peakedness of Batched Renewal Processes," unpublished work, October 1, 1973.
8. A. Kuczura, "The Interrupted Poisson Process as an Overflow Process," B.S.T.J., *52* (March 1973), pp. 437–448.
9. J. Riordan, *Stochastic Service Systems*, New York: John Wiley, 1962, p. 12.

THE BELL SYSTEM TECHNICAL JOURNAL
Vol. 55, No. 7, September 1976
Printed in U.S.A.

Analysis of Toll Switching Networks

By R. S. KRUPP

(Manuscript received December 26, 1975)

Two techniques are introduced for extending C. Y. Lee's method of switching network analysis to cases of toll-type networks. The methods avoid certain inconsistent independence assumptions which would otherwise be a source of inaccuracies. One method partitions the Lee graph in a special way, while the other uses a lemma that characterizes the generating function of an average network property. Examples are worked for three-stage networks and a model of the No. 4 ESS.

I. INTRODUCTION

In a well-known 1955 article,[1] C. Y. Lee introduced simplified methods for the analysis of switching network characteristics, such as blocking probability. Using a probability linear-graph (hereafter called Lee graph) to represent the network and an assumption of independent link occupancies, he described ways to quickly obtain approximate expressions in many cases of interest. As an example of possible inaccuracy, Lee pointed out a three-stage network that is known to be nonblocking but is assigned a nonzero blocking probability by his method.

The present work introduces two different techniques for extending Lee's method to avoid certain inconsistent independence assumptions, which are the source of the inaccuracies he noted. The extended methods will, for instance, reproduce M. Karnaugh's more accurate expression[2] for blocking probability of a three-stage network, but with less mathematical labor. When applied to a "generalized" three-stage network that can model the No. 4 ESS,[3] the techniques yield formulas that greatly simplify expressions currently in use. The appendix lists a computer routine to calculate blocking for the case of generalized three-stage networks.

II. FIRST METHOD

2.1 Generalized three-stage switching network

Consider first a "generalized" three-stage switching network, as indicated schematically in Fig. 1. The solid circles in the first and last

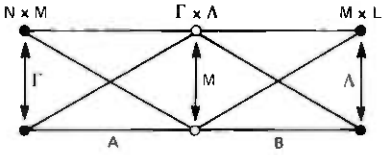

Fig. 1—Generalized three-stage switching network.

stages denote ordinary nonblocking switches, of sizes $N \times M$ and $M \times L$, respectively, such as crosspoint arrays or time-slot interchangers. The open circles in the middle stage, however, stand for switches that could block. Such a switch might, at a given time, have only a probability, rather than a certainty, of being able to connect a given pair of A- and B-links incident on it. This could model additional stages of switching network, such as the time-shared space-division stages in the No. 4 ESS.[3] An independent blocking probability Q is assigned to each middle-stage switch. We use the notation $\bar{Q} \equiv 1 - Q$ to indicate the corresponding transmission probability. The overbar denotes the probabilistic complement in all formulas that follow.

The Lee[1] graph in Fig. 2 shows all paths of the three-stage network that might be used to connect one call between a specified pair of terminations. Besides that pair, there are $E \equiv N - 1$ other input terminations at the first-stage switch and $F \equiv L - 1$ other output terminations at the last-stage switch. If we assign occupancy probabilities P and R, respectively, to input and output terminations other than the designated pair, the A- and B-links will have average occupancies $P_0 \equiv PE/M$ and $R_0 \equiv RF/M$.

If the first stage is a concentrator with $E > M$, it would be mathematically inconsistent to assume that the termination occupancies P were independent. In fact, that would imply a nonzero probability P^E of handling E calls on only M links. It would not be inconsistent to assume *a priori* that the A-link occupancies P_0 were independent when $E \geqq M$. A similar discussion applies to the last stage for the case $F > M$. Assuming that all probabilities P_0, Q, and R_0 are independent, the transmission probability for any single path becomes a product $\bar{P}_0\bar{Q}\bar{R}_0$ of transmission probabilities for each of its portions.

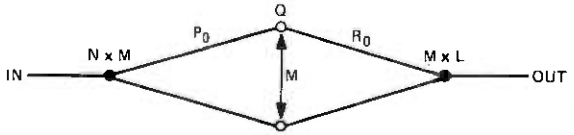

Fig. 2—Lee graph of generalized three-stage network.

Then the blocking probability for the network is just the product of blocking probabilities for each of the M independent paths.

$$\pi_B = (1 - \bar{P}_0\bar{Q}\bar{R}_0)^M = \overline{P_0QR_0}^M. \tag{1}$$

If there is expansion in the first stage, with $M > E$, it would be mathematically inconsistent to assume that the link occupancies P_0 were independent. Indeed, that would imply a nonzero probability P_0^M of busying all M links with at most E calls. It would not be inconsistent to assume that the termination occupancies P were independent when $M \geqq E$. A similar discussion applies to the last stage for the case $M > F$. In the boundary case $E = M$, assuming random connections through the switch, we find that each kind of independence assumption (link or termination) implies the other with $P = P_0$, and neither is inconsistent. Whether either assumption agrees with observed behavior of traffic is a difficult question that will not be explored here.

2.2 Toll-neutral case

To shorten our terminology, we will name the case $E > M$ "local," the case $E < M$ "toll," and the case $E = M$ "neutral." To emphasize the distinction, we cite the celebrated "Clos-type" network. Clos[4] showed that a pure three-stage network (the case $Q = 0$) will be nonblocking when $M > E + F$. But (1) can vanish only when P_0 and R_0 do. The contradiction arises from using the link independence assumptions in a toll case. The local case will not be considered in this study.

No matter what assumptions are appropriate, the event of having K busy A-links is the same as that of K busy input terminations, whence they have equal probability. In the toll case this is

$$\pi_A = \binom{E}{K} P^K(1 - P)^{E-K}, \tag{2}$$

since there are $\binom{E}{K}$ ways to choose K busies plus $E - K$ idles among E terminations, and each arrangement occurs with probability $P^K(1 - P)^{E-K}$, when termination occupancies P are independent. Assuming that all probabilities P, Q, and R_0 are independent, transmission probability for any single path containing an idle A-link is $\bar{Q}\bar{R}_0$, and blocking probability for all $M - K$ idles becomes $(1 - \bar{Q}\bar{R}_0)^{M-K}$. Multiplying by the probability of $M - K$ idles (2) and summing over all $0 \leqq K \leqq E$ yield

$$\pi_B = \sum_K \binom{E}{K} P^K(1 - P)^{E-K}(1 - \bar{Q}\bar{R}_0)^{M-K}, \tag{3}$$

the network blocking probability for the "toll-neutral" case $E \leqq M = F$,

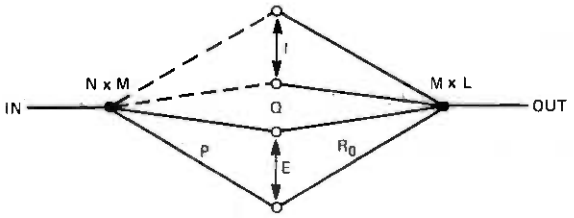

Fig. 3—Graph of toll-neutral network.

as opposed to the "neutral-neutral" case $E = M = F$ given by (1), in the form

$$\pi_B = (1 - \bar{P}\bar{Q}\bar{R})^M = \overline{\bar{P}\bar{Q}\bar{R}}^M. \tag{1a}$$

We have set $R_0 = R$ since $F = M$ and $P_0 = P$ since $E = M$.

By binomial theorem, the sum (3) is

$$\pi_B = (1 - \bar{Q}\bar{R}_0)^{M-E}(1 - \bar{P}\bar{Q}\bar{R}_0)^E, \tag{4}$$

but this may be derived by a more direct route. To see this, we note that there is a minimum of $I \equiv M - E$ idle A-links, no matter what the status of the E input terminations. Let us set aside I such idle A-links in Fig. 3, denoting them by dashed lines. This partitions Fig. 2 into two parallel graphs, the upper one with I independent paths and all A-links idle, and the lower one with E independent paths. The lower graph is just the neutral case so that, *mirabile dictu*, its A-links have independent occupancies P if its input terminations do. Thus, blocking probability for the lower graph is given by (1), with P_0 replaced by P and M by E. Blocking for the upper graph is just $(1 - \bar{Q}\bar{R}_0)^I$, as noted before (3). Network blocking (4) is then the product of these two terms.

2.3 Toll-toll case

There remains only the "toll-toll" case $E \leqq M \geqq F$, with the assumption of independent occupancies P and R for input and output terminations. The argument leading to (2) may be repeated to yield the probability

$$\pi_{AB} = \binom{E}{X}\binom{F}{Y} P^X(1 - P)^{E-X}R^Y(1 - R)^{F-Y} \tag{5}$$

of having X busy A-links and Y busy B-links.

The pure three-stage switch ($Q = 0$) blocks only if none of the $M - X$ idle A-links matches any of the $M - Y$ idle B-links. There are $\binom{M}{Y}$ ways to arrange the idle B-links, but only $\binom{M-X}{Y}$ of these match all $M - Y$ idles to the X busy A-links. Thus, assuming all arrangements

are equally probable, the mismatch blocking probability becomes

$$\pi_{XY} = \binom{X}{M-Y} \Big/ \binom{M}{Y} = X!Y!/M!(X+Y-M)! \qquad (6)$$

Multiplying (5) by (6) and summing over $0 \leqq X \leqq E$ and $0 \leqq Y \leqq F$ yields the overall network blocking probability

$$\pi_B = \sum_{X,Y} \pi_{AB}(X, Y)\pi_{XY}. \qquad (7)$$

Karnaugh[2] has performed this sum, using binomial theorem first on the X-sum to obtain

$$\pi_B = \binom{E}{M-F} \Big/ \binom{M}{F} \sum_Y \binom{E+F-M}{F-Y} P^{M-Y} R^Y (1-R)^{F-Y} \qquad (8)$$

and then on the Y-sum to yield the blocking

$$\pi_B = \frac{E!F!}{M!(E+F-M)!} P^{M-F} R^{M-E} (1-\bar{P}\bar{R})^{E+F-M} \qquad (9)$$

in closed form. Now π_B in (9) appears to be the product of a "combinatorial" factor $\binom{E}{M-F} / \binom{M}{F}$ and a "probabilistic" one. A direct derivation will help to bring out their origins.

Again, there are at least $I \equiv M - E$ idle A-links and $J \equiv M - F$ idle B-links. We set these aside in the Lee graph in Fig. 4, denoting them by dashed lines, as before. No matching of dashed A- and B-links is shown in the figure, since this could not correspond to a blocked state of the network. There are E solid A-links, corresponding to the neutral case, so that we can assume independent occupancies $P_0 = P$ for them. Similarly, the F solid B-links will have independent occupancies R.

Figure 4 clearly partitions Fig. 2 into three parallel graphs. The top graph has I independent paths and its blocking is obviously R^I. The bottom graph has J independent paths, and its blocking is P^J. The middle graph has $H \equiv M - I - J = E + F - M$ independent paths, each with transmission probability $\bar{P}\bar{R}$, so that its blocking is

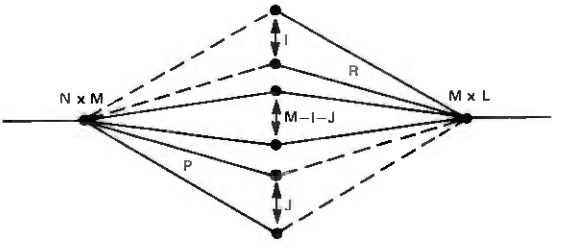

Fig. 4—Graph of toll-toll three-stage network.

$(1 - \bar{P}\bar{R})^{M-I-J}$. The product of these three blocking probabilities,

$$\pi_P = P^J R^I \bar{P}\bar{R}^{M-I-J}, \tag{10}$$

is the blocking for the network configuration in Fig. 4 and is also the "probabilistic" portion of π_B in (9).

There are $\binom{M}{J}$ ways to arrange the dashed B-links, but only $\binom{M-I}{J}$ of these match all J dashed B-links to solid A-links. If all arrangements are equally likely, the quotient $\binom{E}{J}/\binom{M}{J}$ is the probability of the "blockable" configuration in Fig. 4. This accounts for the "combinatorial" portion of π_B in (9), which is in fact the blocking at full occupancy $P = R = 1$. Note that, if $M > E + F$, then $(E + F - M)!$ is infinite and π_B vanishes in (9), consistent with Clos' result.

2.4 Generalized toll-toll case

Even if Z of the $M - X$ idle A-links match Z of the $M - Y$ idle B-links in (5), a generalized three-stage network may still block, with probability Q^Z, for P, Q, and R independent. There are $\binom{M}{Y}$ ways to arrange the $M - Y$ idle B-links, but only $\binom{M-X}{Z}\binom{X}{M-Y-Z}$ ways to match just Z of them to $M - X$ idle A-links and the rest to the X busy A-links. For equally likely arrangements, then, the probability of a Z-match becomes

$$\pi_Z = \binom{M-X}{Z}\binom{X}{M-Y-Z}\Big/\binom{M}{Y}. \tag{11}$$

The overall network blocking probability now is the sum over X, Y, and Z of the product of (5), (11), and Q^Z,

$$\pi_B = \sum_{X,Y,Z} Q^Z \pi_{AB}(X, Y)\pi_Z(X, Y). \tag{12}$$

As an example,[3] $M = 128$ and $L = N = 105$ in the No. 4 ESS so that $E = F = 104$ and $I = J = 24$. This makes π_B in (12) the sum of 302,845 nonzero terms.

As discussed previously, a more direct derivation of blocking probability π_B may be prosecuted for the generalized three-stage network. We set aside I idle A-links and J idle B-links as dashed lines in the Lee graph, Fig. 5. This time there may be some matching of V dashed A- and B-links, for $0 \leqq V \leqq I, J$. Figure 5 partitions Fig. 2 into four parallel graphs with $I - V$, V, $J - V$, and $H + V = M - I - J + V$ independent paths, respectively, to yield blocking probabilities of $(1 - \bar{Q}\bar{R})^{I-V}$, Q^V, $(1 - \bar{P}\bar{Q})^{J-V}$, and $(1 - \bar{P}\bar{Q}\bar{R})^{H+V}$ as discussed earlier.

There are $\binom{M}{J}$ ways to arrange the J dashed B-links but only $\binom{I}{V}\binom{E}{J-V}$ ways to match just V of them to the I dashed A-links and

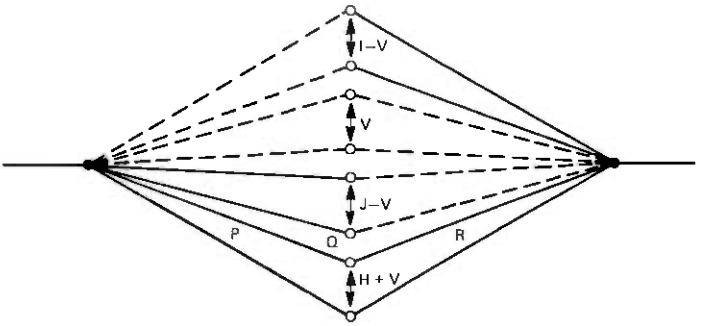

Fig. 5—Graph of toll-toll generalized three-stage network.

the rest to the E solid A-links. Thus, the probability of a V-match is

$$\pi_V = \binom{I}{V}\binom{E}{J-V}\Big/\binom{M}{J} = \frac{I!J!E!F!/M!V!}{(I-V)!(J-V)!(H+V)!} \quad (13)$$

if all arrangements have equal likelihood. This is multiplied by the blocking probability for a network with V matches, as in Fig. 5, and summed over V to yield the overall network blocking probability

$$\pi_B = \sum_V \pi_V Q^V (1 - \bar{P}\bar{Q})^{J-V}(1 - \bar{Q}\bar{R})^{I-V}(1 - \bar{P}\bar{Q}\bar{R})^{H+V}. \quad (14)$$

III. SECOND METHOD

For the example of the No. 4 ESS, π_B in (14) is the sum of 25 non-zero terms. It does not appear to be possible to perform the V-sum and reduce (14) to a single term; however, we shall see that π_B does have a simple one-term generating function, as well as one-term operator-product expressions.

3.1 The generating function

It is possible to perform the X-, Y-, and Z-sums in (12), and thus reduce π_B to the simpler form (14). While tedious, this exercise is also highly instructive. Writing out (5) and (11) at length in (12) yields

$$\pi_B = \sum_{X,Y,Z} P^X Q^Z R^Y \frac{(M-X)!}{(E-X)!}\alpha^{E-X}\frac{(M-Y)!}{(F-Y)!}\beta^{F-Y}\pi_{XYZ}, \quad (15)$$

where $\alpha \equiv \bar{P}$, and $\beta \equiv \bar{R}$ and the last factor is

$$\pi_{XYZ} \equiv \frac{E!F!/M!Z!}{(M-X-Z)!(M-Y-Z)!(X+Y+Z-M)!}$$
$$= \frac{E!F!}{M!^2}\binom{M}{Z}\binom{M-Z}{X}\binom{X}{M-Y-Z}. \quad (16)$$

Substituting the following identities into (15),

$$\frac{(M-X)!}{(E-X)!}\,\alpha^{E-X} = \partial_\alpha^{M-E}\alpha^{M-X} = \partial_\alpha^{I}\alpha^{M-X} \tag{17}$$

$$\frac{(M-Y)!}{(F-Y)!}\,\beta^{F-Y} = \partial_\beta^{M-F}\beta^{M-Y} = \partial_\beta^{J}\beta^{M-Y}, \tag{18}$$

where ∂_α and ∂_β are the α- and β-derivatives, yields

$$\pi_B = \frac{E!F!}{M!^2}\,\partial_\alpha^I\partial_\beta^J \sum_{X,Z} P^X Q^Z \binom{M}{Z}\binom{M-Z}{X} S_Y \alpha^{M-X} \tag{19}$$

$$S_Y \equiv \sum_Y \binom{X}{M-Y-Z} R^Y \beta^{M-Y}. \tag{20}$$

We should note that, formally, α and β are independent variables, which are set equal to $\bar{P}$ and $\bar{R}$ only after all differentiations are performed. Thus, ∂_α and ∂_β do not act on P and R.

By binomial theorem, the sum in (20) is just

$$S_Y = \beta^Z R^{M-X-Z}(\beta + R)^X,$$

which reduces (19) to

$$\pi_B = \frac{E!F!}{M!^2}\,\partial_\alpha^I\partial_\beta^J \sum_Z Q^Z\beta^Z \binom{M}{Z} S_X \tag{21}$$

$$S_X \equiv \sum_X \binom{M-Z}{X} P^X \alpha^{M-X} R^{M-X-Z}(\beta + R)^X. \tag{22}$$

Similarly, the sum in (22) may be performed to get $S_X = \alpha^Z\gamma^{M-Z}$ for $\gamma \equiv \alpha R + \beta P + PR$ and reduce (21) to

$$\pi_B = \frac{E!F!}{M!^2}\,\partial_\alpha^I\partial_\beta^J \sum_Z \binom{M}{Z} \alpha^Z\beta^Z Q^Z \gamma^{M-Z}. \tag{23}$$

The sum in (23) is just $(\alpha\beta Q + \gamma)^M$, by a third application of binomial theorem, whence it becomes

$$\pi_B = \frac{E!F!}{M!^2}\,\partial_\alpha^I\partial_\beta^J(\alpha\beta Q + \alpha R + \beta P + PR)^M$$

$$= \frac{E!}{M!}\,\partial_\alpha^I(\alpha Q + P)^J(\alpha\beta Q + \gamma)^F. \tag{24}$$

The forms (24) are about the closest we can get π_B to a simple closed expression. Leibniz' rule for the derivatives of a product will give (24) the form

$$\pi_B = \sum_V \pi_V Q^V(\alpha Q + P)^{J-V}(\beta Q + R)^{I-V}(\alpha\beta Q + \gamma)^{H+V}, \tag{25}$$

with π_V as in (13). Substituting $\alpha = \bar{P}$ and $\beta = \bar{R}$ will now reduce (25) to (14), since, for example,

$$\alpha Q + P = \bar{P}(1 - \bar{Q}) + 1 - \bar{P} = 1 - \bar{P}\bar{Q} \tag{26}$$

$$\begin{aligned}\alpha\beta Q + \gamma &= \beta(\alpha Q + P) + R(\alpha + P) \\ &= \bar{R}(1 - \bar{P}\bar{Q}) + 1 - \bar{R} = 1 - \bar{P}\bar{Q}\bar{R}.\end{aligned} \tag{27}$$

What is particularly illuminating in the preceding calculation is step (24). It says that $\pi_B(I, J)$, the blocking probability for a network with I excess A-links and J excess B-links, is a differential coefficient of "something." To make this idea more precise, we construct the corresponding generating function G. Multiplying (24) by $\binom{M}{I} U^I \binom{M}{J} W^J$ and then summing over all $0 \leqq I, J \leqq M$ yield the form

$$\begin{aligned}G &= \sum_{I,J} \binom{M}{I} U^I \binom{M}{J} W^J \pi_B(I, J) \\ &= \sum_{I,J} \frac{U^I}{I!} \frac{W^J}{J!} \partial_\alpha^I \partial_\beta^J (\alpha\beta Q + \alpha R + \beta P + PR)^M.\end{aligned} \tag{28}$$

By Taylor's theorem, the second line is just

$$\begin{aligned}G &= [(U + \bar{P})(W + \bar{R})Q + (U + \bar{P})R + (W + \bar{R})P + PR]^M \\ &= [(U + 1)(W + 1) - (U + \bar{P})(W + \bar{R})\bar{Q}]^M \\ &= (U + 1)^M (W + 1)^M \left[1 - \left(1 - \frac{P}{U + 1}\right)\left(1 - \frac{R}{W + 1}\right)\bar{Q}\right]^M.\end{aligned} \tag{29}$$

Thus, $\pi_B(I, J)$ can be obtained by expanding (29) in powers of U and W, then inspecting the coefficient of $U^I W^J$. In practice, we get the coefficient by differentiating I times in U and J times in W, then setting $U = W = 0$. But this is exactly equivalent to the steps leading from (24) to (14).

3.2 Fundamental lemma

In the preceding section, it was shown that blocking probability π_B could be obtained quickly and directly from a generating function G, rather than through an argument involving a four-way partition of the Lee graph. If we could now obtain G directly, without steps (5), (11), (12), and (15) to (24), a great deal of effort might be saved. The structure of G is indeed determined by the following lemma, which has surprisingly little to do with switching networks.

We idealize the network as a "black box," as in Fig. 6, on which a certain set of M "trunks" are terminated. These are assumed to have

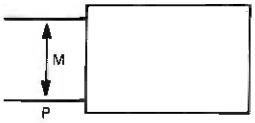

Fig. 6—Network idealized as black box.

independent occupancy probabilities P, except that some number $I \leqq M$ of the trunks are "dead" or disconnected, with zero occupancies. Associate with the black box some quantity $\Lambda(K)$, a function of the number K of busy terminations among the $E = M - I$ "active" trunks. By using (2), we find the average value of Λ to be

$$\pi(I, P) \equiv \sum_K \binom{M-I}{K} P^K (1-P)^{M-I-K} \Lambda(K). \tag{30}$$

We have assumed that the M trunks are interchangeable, in the sense that Λ, and hence π, does not depend on which I of the M are dead.

Fundamental Lemma: *The generating function for* $\pi(I, P)$ *is written in terms of* $\pi(0, P)$ *as*

$$G \equiv \sum_I \binom{M}{I} U^I \pi(I, P) = (U+1)^M \pi\left(0, \frac{P}{U+1}\right). \tag{31}$$

Formal Proof: Substitute (30) into (31) and use binomial theorem to perform the sum over $0 \leqq I \leqq M$.

Informal Proof: Suppose that each trunk has an independent probability λ of being active, and hence $\bar{\lambda} = 1 - \lambda$ of being dead. Then the average value of π is just

$$\hat{\pi} = \sum_I \binom{M}{I} \lambda^{M-I} (1-\lambda)^I \pi(I, P). \tag{32}$$

On the other hand, each trunk carries an average load of λP erlangs, independent of the others, so that $\hat{\pi} = \pi(0, \lambda P)$. We now define $U \equiv \bar{\lambda}/\lambda$, which yields $\lambda = 1/(U+1)$, and set $G = (U+1)^M \hat{\pi}$ to transform (32) into (31). The model of "dead trunks" is invoked only to validate the mathematical relation (31), of course, and need not accord with observed behavior.

An obvious application of the lemma is to let the black box be a switching network and π be its blocking probability π_B for some pair of terminations. As an example, consider the "toll-neutral" case of the generalized three-stage network, with $E \leqq M = F$. Let the M trunks be terminated on the same first-stage switch as the input

termination of the pair whose blocking is sought. Then $I = 0$ corresponds to the neutral case $E = M$, for which (1) is valid with $P_0 = P$. Now the generating function becomes

$$G = (U+1)^M \left[1 - \left(1 - \frac{P}{U+1}\right)\bar{Q}\bar{R}_0\right]^M$$
$$= [U + 1 - (U + \bar{P})\bar{Q}\bar{R}_0]^M. \tag{33}$$

Differentiating I times at $U = 0$ yields the blocking

$$\pi_B(I, P) = \partial_U^I G/I! \binom{M}{I}$$
$$= (1 - \bar{Q}\bar{R}_0)^I (1 - \bar{P}\bar{Q}\bar{R}_0)^{M-I}, \tag{34}$$

which is the same formula as (4). A bare minimum of knowledge about the network structure, just formula (1), was thus sufficient to determine blocking probability.

The "toll-toll" case, $E \leqq M \geqq F$ of the generalized three-stage network, requires an iterated form

$$G \equiv \sum_{I,J} \binom{M}{I} U^I \binom{\mu}{J} W^J \pi(I, P; J, R)$$
$$= \sum_I \binom{M}{I} U^I \pi\left(I, P; 0, \frac{R}{W+1}\right)(W+1)^\mu$$
$$= (U+1)^M (W+1)^\mu \pi\left(0, \frac{P}{U+1}; 0, \frac{R}{W+1}\right) \tag{35}$$

of the lemma. For $\mu = M$ trunks terminated on the same last-stage switch as the output termination of the pair whose blocking is sought, we see that $I = J = 0$ is the neutral case $E = M = F$, with π_B given by (1a). Thus, substituting (1a) into (35) yields a generating function

$$G = (U+1)^M (W+1)^M \left[1 - \left(1 - \frac{P}{U+1}\right)\left(1 - \frac{R}{W+1}\right)\bar{Q}\right]^M, \tag{36}$$

which is the same as (29). The blocking becomes

$$\pi_B = \partial_U^I \partial_W^J G/I! \binom{M}{I} J! \binom{M}{J} = \partial_W^J g/J! \binom{M}{J} \tag{37}$$

$$g = (W+1)^M \left[1 - \left(1 - \frac{R}{W+1}\right)\bar{Q}\right]^I$$
$$\cdot \left[1 - \bar{P}\left(1 - \frac{R}{W+1}\right)\bar{Q}\right]^{M-I}, \tag{38}$$

and applying Leibniz' rule for the derivatives at $W = 0$ again yields (14).

Another approach is to observe that we have already "differentiated off" I terminations in the "toll-neutral" case. Applying the lemma once more to (34), we can construct the generating function g in (38) at once and then "remove" the J spare output terminations as in (37) to obtain blocking probability (14). Again, only (1) was needed to specify the particular network under consideration.

3.3 Operator formulation

Lemma (31) may be "solved" for $\pi(I, P)$ by making a formal expansion of its right side in terms of ∂, the P-derivative. Observing that

$$e^{aP\partial}P^n = \sum_l \frac{(aP\partial)^l}{l!} P^n = \sum_l \frac{(an)^l}{l!} P^n = (e^a P)^n \tag{39}$$

and hence $A^{P\partial}f(P) = f(AP)$, the generating function is

$$G = (U + 1)^{M-P\partial}\pi(0, P) = \sum_{I=0}^{\infty} \binom{M - P\partial}{I} U^I \pi(0, P). \tag{40}$$

Equating powers of U in (31) and (40) yields the identity

$$\pi(I, P) = \binom{M - P\partial}{I} \pi(0, P) \Big/ \binom{M}{I}, \tag{41}$$

which we write out as an operator product

$$\begin{aligned}\pi(I, P) &= \left(1 - \frac{P\partial}{M - I + 1}\right) \cdots \left(1 - \frac{P\partial}{M - 1}\right)\left(1 - \frac{P\partial}{M}\right) \pi(0, P) \\ &= \left(1 - \frac{P\partial}{M - I + 1}\right) \pi(I - 1, P).\end{aligned} \tag{42}$$

This has a simple and natural interpretation: "deloading operator" $1 - P\partial/E$ serves to "remove" one of the E remaining terminations represented in the expression $\pi(M - E, P)$ for any average network property π.

Of course, the validity of the mathematical manipulations above must still be demonstrated. This hinges upon establishing convergence of the operator expansion in (40), and hence the sum in I. But we note that each factor of the form $n - P\partial$ will annihilate the corresponding power P^n in $\pi(0, P)$. Thus, if π is a polynomial of degree M at most, as in (30), it is annihilated completely in all terms of (40) for which I exceeds M, and the expansion indeed converges, since the sum is finite. In practical calculations of blocking probabilities or other

formulas, the operator formulation (42) may not be as convenient to use as direct differentiation of the generating function.

IV. SUMMARY AND DISCUSSION

Two techniques are introduced to extend C. Y. Lee's method to switching networks of "toll" types defined in the text. Basically, these have some expansion in the first stage or concentration in the last stage, or both. The link independence assumptions of Lee's method are inconsistent in such cases, which causes some inaccuracy.

The first of the two extension techniques partitions the Lee graph into two or more smaller graphs, so that the independence assumptions will be consistent within various portions. This is done by setting apart the proper number of links that are known to be idle. The first technique is applied to examples of three-stage networks, yielding a result of Karnaugh's and a simplification of the expression used for computing blocking for the No. 4 ESS. To focus attention on the methods, all examples worked out are blocking probabilities, but other network averages may be treated similarly.

The second, and more general, technique makes use of a lemma that characterizes the generating function of an average property for a whole family of networks. In a sense, this technique is a counterpart of the first, since it operates by attaching a sufficient number of idle "phantom" terminations to the network to make the link independence assumptions valid, instead of setting aside idle links. Then the generating function can be constructed from the resulting "neutral" case, and the lemma, or an equivalent operator formulation, allows removal of the excess terminations. Two of the three-stage network examples are reworked to make a comparison of the two techniques.

V. ACKNOWLEDGMENTS

The author is grateful for comments and suggestions from Thomas J. Cieslak, Frank K. Hwang, Elena M. Johnson, Joseph G. Kappel, and Mary N. Youssef, and for assistance from Sheila R. Wiggins in testing the program for calculating blocking probabilities.

APPENDIX

The FORTRAN subroutine listed in Table I calculates the blocking probability π_B given by (14) for the "toll-toll" case of the generalized three-stage switching network. Cancelling among the nine factorials in (13) yields an efficient calculation and minimizes the chance of underflow or overflow. The routine is accessed by:

CALL BLOCK (I, P, J, R, M, Q, PI)

Table I — Blocking probability subroutine

```
      SUBROUTINE BLOCK (I, P, J, R, M, Q, PI)
      K = M - I - J
      L = MAX0(0, I + J - M)
      PQ = 1.0 - (1.0 - P)*(1.0 - Q)
      RQ = 1.0 - (1.0 - R)*(1.0 - Q)
      SQ = 1.0 - (1.0 - R)*(1.0 - Q)*(1.0 - P)
      A = 1.0
      IF(L.GT.0) A = Q**L
      A = A*PQ**(J - L)*RQ**(I - L)*SQ**(K + L)
      B = A
      C = Q*SQ/(PQ*RQ)
      D = 1.0
      LOW = L + 1
      LIM = MIN0(I, J)
      IF(LIM - L) 30, 20, 10
   10 DO 15 N = LOW, LIM
      A = A*C*FLOAT((I - N + 1)*(J - N + 1))/FLOAT((K + N)*N)
      B = B + A
   15 D = D*FLOAT(K + L + N)/FLOAT(M + N - LIM)
   20 PI = B*D
   30 RETURN
      END
```

and, referring to Fig. 1, the arguments are:

- $I = M - E = M - N + 1$ minimum number of idle A-links
- $J = M - F = M - L + 1$ minimum number of idle B-links
- M number of center-stage switches
- P average occupancy probability of input terminations
- Q blocking probability of center-stage switches
- R average occupancy probability of output terminations
- PI returns the calculated value of π_B.

Independence is assumed for all P, Q, and R.

REFERENCES

1. C. Y. Lee, "Analysis of Switching Networks," B.S.T.J., *34*, No. 6 (November 1955), 1287–1315.
2. M. Karnaugh, unpublished work, August 1954.
3. H. E. Vaughan, "An Introduction to No. 4 ESS," paper presented at the International Switching Symposium, Cambridge, Massachusetts, June 6, 1972.
4. C. Clos, "A Study of Non-Blocking Switching Networks," B.S.T.J., *32*, No. 2 (March 1953), 406–424.

THE BELL SYSTEM TECHNICAL JOURNAL
Vol. 55, No. 7, September 1976
Printed in U.S.A.

Test Facility for a Message-Switching System

By W. E. BRACKER and E. R. SEARS

(Manuscript received October 8, 1975)

This paper describes the development and use of a test facility for a computer-based store-and-forward message-switching system. The test facility provides a close approximation to actual operating environments, allowing the system to be tested in a realistic environment. The facility provides a vehicle for many essential system studies including performance monitoring and measurement, load testing, certification, and validation of various simulation and forecasting models. A wide range of tools is used in this facility—hardware and software monitors, terminal and network simulators, and data reduction and analysis packages. One version of the system is used to drive and thus test another version. A language for creating a set of test data is defined and is used to present various parameters to the switching system.

I. INTRODUCTION

A comprehensive test environment is important in the development and maintenance of any large computer system. In particular, when dealing with a message-switching system, special attention must be given to message loading, traffic mixes, and network configuration variables. Two methods of controlling these variables to test the system are:

(*i*) The use of real terminals and operators to drive the system, or
(*ii*) Simulation of terminal and operator system interactions to exercise the system as though it were in live operation.

The second method was used in our approach because it leads to more comprehensive, more controlled, and easily repeatable tests.

We describe the concept of "using the system to test the system"—a test facility is created from an existing system configuration. The system described is BISCOM,* a large-scale, computer-based, store-and-forward message switcher.

* Business Information Systems Communication System

Early in the development of BISCOM, the need for a comprehensive facility was recognized. The important factor in the creation of the facility was the need for a controlled test environment—one in which the operation of BISCOM could be observed and measured.

II. BISCOM OVERVIEW

Figure 1 illustrates a typical BISCOM installation. For reliability reasons, BISCOM is configured as a dual system with two central processing units (CPUs), each CPU having a complete set of peripheral units. One system serves as the Active (primary) message switcher while the other system acts as the Recover (backup) system in case of a failure in the Active system. This division is purely logical; either of the two systems may be the primary or recovery system (the communication network interfaces are attached to the machine serving as the active message switcher). BISCOM is designed to operate on a Xerox* Sigma-5 computer with core memory sizes up to 128,000, 32-bit words.

During Active system operation, all significant events are logged as follows:

Message Journals

(*i*) All User Input Messages
(*ii*) All System Internally Generated Messages
(*iii*) Messages Fetched or Delivered From System Data Files.

Logging Functions

(*i*) Input Start of Message
(*ii*) Input End of Message
(*iii*) Output Start of Message
(*iv*) Output End of Message
(*v*) On-line Network Changes
(*vi*) Disk File Transaction Data
(*vii*) Periodic Terminal Handler Statistics
(*viii*) Disk Retry and Parity Error Statistics.

The complete text of all switched messages are journalized (recorded) on magnetic tape. These tapes are input to a set of programs that keep the Recover system up to date with the Active system (e.g., they record the current state of the data base, network configuration, undelivered messages, etc.).

In the event of an Active system hardware or software failure, the Recover system becomes the Active system. At the present time this

* Xerox is a trademark of the Xerox Corporation.

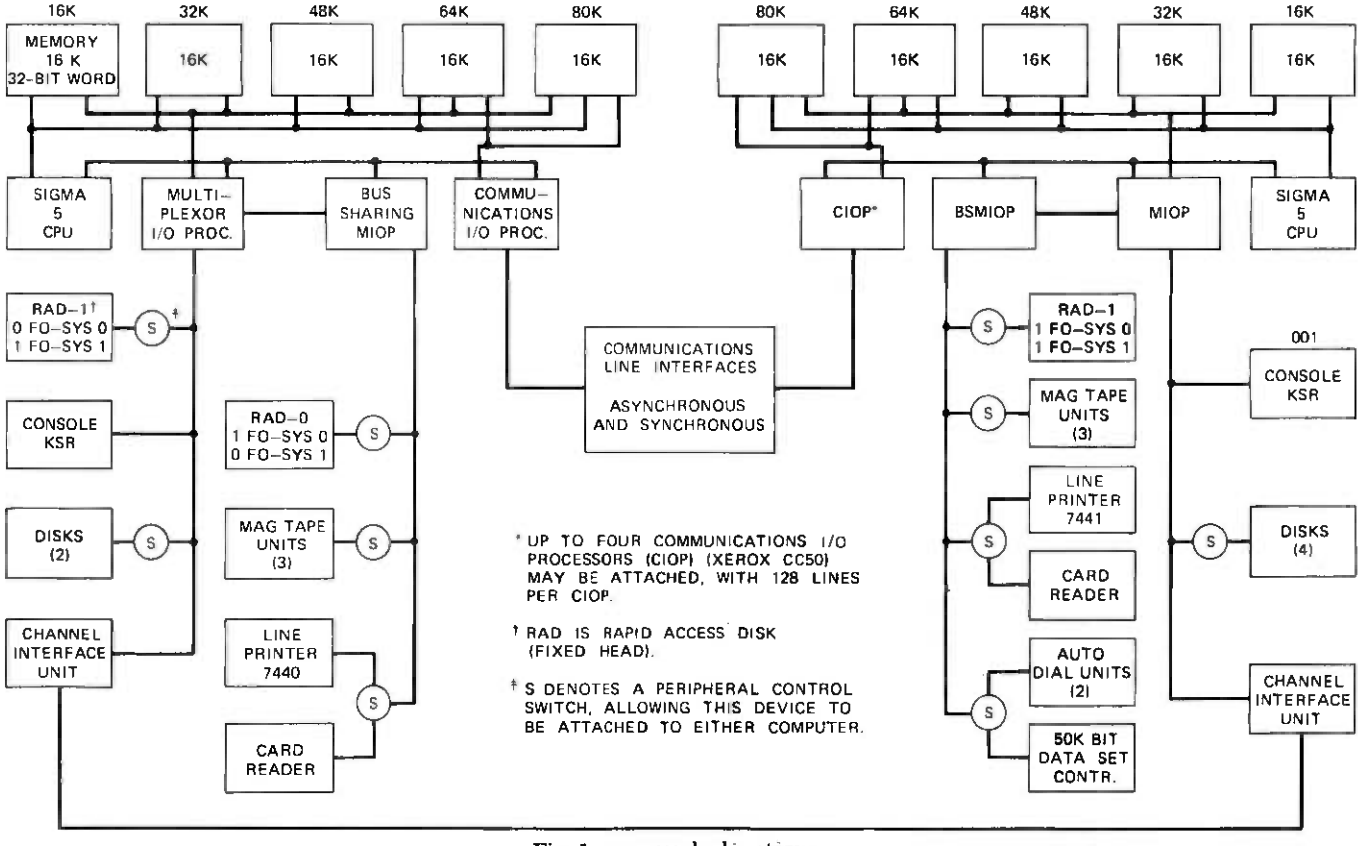

Fig. 1—BISCOM dual system.

process is manual, although testing of an automatic switch-over in case of failure is underway. In future versions of BISCOM, logs and message journals will be sent directly from the active to the backup system over a channel-interface unit.

BISCOM uses access arrangements including data-link control procedures that agree with those contained in Standard X3.28 (1971) published by the American National Standards Institute. These access arrangements include low and medium speeds, asynchronous and synchronous, respectively; switched and dedicated access lines; and remote computer access at speeds up to 50 kilobits/second.

Messages to be switched by BISCOM consist of a header and text; message framing is accomplished by three control characters: start of header (SOH), start of text (STX), and end of text (ETX). The system is text transparent in that only header information is scanned and validated, although illegal characters in the text are recognized. Information in the header specifies the actions BISCOM is to take with respect to the message. If the header is invalid or incomplete, delivery

Table I — Message mix and traffic loads for a typical busy hour

Type*	Input (Msg/Hour)	Length†	Deliveries‡			Output (Msg/Hour)
			Low	Med	Other	
POSM	125	100	1			125
SMST	1200	425				0
SMDL	200	500		1		200
SMFT	3000	25				3000
SMRD	700	440		1		700
SMRD§	500	440		3		1500
SMRD	100	440	3			300
SMRD	400	700	1			400
SMRD	600	700		1		600
SMRD	200	440	2			400
SMSD	1240	440		2	1	3720
SMSD	320	440		4		1280
SMSD‖	30	600	7			210
SMCL	125	25				0
SMRP#	625	425				0
Total Input	9365				Total Output	12,435

* See Appendix A (POSM = straight switched).
† Bytes.
‡ Low—110 baud, 150 baud terminals; med—2400 baud terminals.
§ 500 messages in the SMF file will be replaced with 440-byte messages. The new messages are delivered to three medium-speed terminals.
‖ 30 messages of 600 bytes each are stored in the SMF file and delivered to seven low-speed terminals.
625 messages of 425 bytes each will replace an equal number of messages already in the SMF file.

will not be attempted and the originating station is notified. If the header is acceptable, the message is switched to the designated location(s) and/or stored in one of the system data files. Appendix A provides a description of the message syntax accepted by BISCOM.

A BISCOM message mix is determined by the types of messages input during a given hour, while message load is determined by the number of input and output messages processed during this period. Table I shows a typical busy-hour message mix and traffic load for a sample BISCOM installation. The BISCOM busy hour is defined as a fixed percentage of the theoretical upper limit of input and output messages that can be processed during a selected peak 60-minute period.

III. TEST FACILITY OVERVIEW

The test facility is comprised of three major components: terminal and network simulators, hardware monitors, and software monitors. The logical configuration is shown in Fig. 2.

The terminal and network simulators drive the Active system; a set of real communication lines in the Active system is attached to simulated terminals in the Driver. In conjunction with a test message format handler in the Driver, the simulators respond to polling and selection sequences from BISCOM, and transmit and receive traffic.

Hardware monitors are attached to the Active system to monitor physical resource utilization through test points that include the CPU hardware and peripheral subsystem. Output from the monitors is

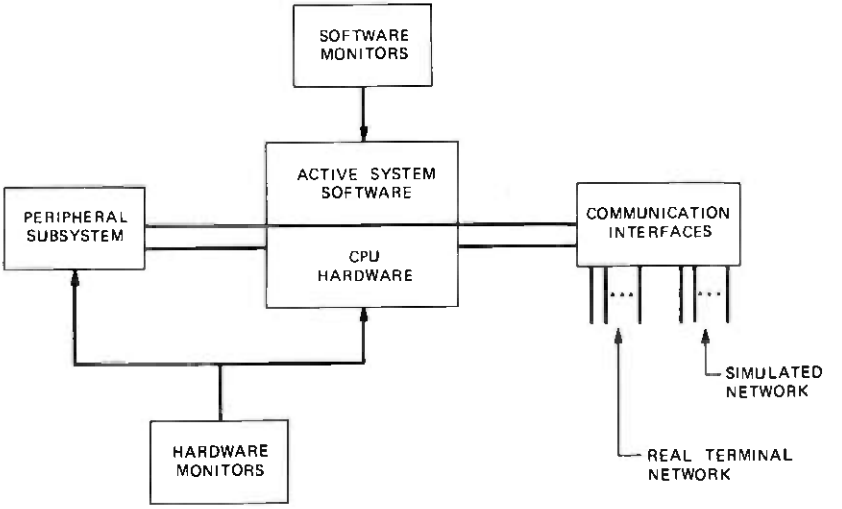

Fig. 2—The test facility.

stored on magnetic tape and forms input to a set of data-reduction routines.

The software monitors, which are incorporated in the code of both the Active system and the Driver, serve to measure system physical and logical resource utilization. The Active system outputs statistics every three minutes to a Reports terminal, and also logs significant system events onto magnetic tape; the Driver periodically outputs communication line profiles to a line printer.

IV. TEST FACILITY DETAILS

To examine the test facility in detail, we discuss

(*i*) Terminal, network, and traffic simulations.
(*ii*) Test messages.
(*iii*) Measurement tools.

4.1 Terminal, network, and traffic simulation

To create the Driver portion of the test environment, the normal recovery system is replaced with load Driver software, as shown in Fig. 3. The Active and Driver computers are connected by transmission lines that terminate in low- and medium-speed data sets. The network and corresponding communication lines are defined in both the Active and Driver systems by a network-generation program. This definition consists of core memory tables that characterize the lines in terms of speed, character code, and access arrangement.

The Active network consists of a set of lines terminating in real terminals and simulated terminals; the Driver consists of a set of

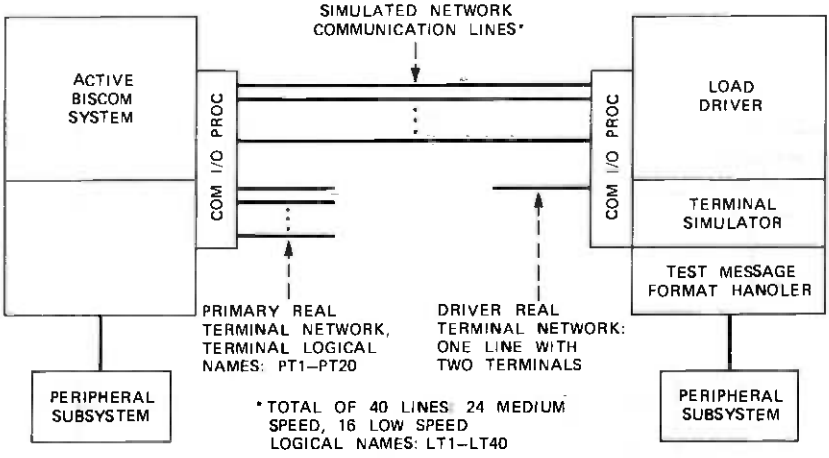

Fig. 3—Example of the active and load-driver configuration.

real terminals and terminal simulators. Active simulated terminals are connected to the Driver via low- and medium-speed data-set connections. During the course of a test run, traffic is received from a subset of driver terminals and directed to primary network real and simulated terminals and the various BISCOM data files.

To the Active system, the simulated terminals appear real—no software changes are made in the Active system to distinguish between the simulated and real portions of the network.

The Driver software represents a slightly modified BISCOM. Existing BISCOM software is used to perform support functions, such as message queuing, and special software is added that communicates with the primary system to generate a flow of traffic. This special software consists of two terminal simulators and a test-message format handler. One of the simulators handles medium-speed (2400–4800 bits/second, synchronous) communication lines; the other simulator handles low-speed (110 bits/second, asynchronous) communication lines. A Format Handler program intercepts test traffic queued to the Driver simulators and restructures the traffic for transfer to the Active system.

As far as the Driver software is concerned, simulators are identical to normal terminals. It is this concept which permits the BISCOM system itself to be employed as the Driver. When activated, a simulator makes the decision, when polled, whether to send a message, and, when selected, whether to receive a message. The simulators may also respond negatively to polls or selections for a predetermined length of time.

Driver test traffic input may come from one of two sources: (*i*) real terminals defined in the Driver network or (*ii*) a tape file. Messages that have been created by an off-line process and stored on the tape file may be sent by the Driver to the Active system and switched as if they were coming from actual terminals; of course, such messages must conform to valid BISCOM syntax. Prior to a test run, a tape is generated representing a specific load test; for example, it may be desirable to perform a 1-hour test representing a load of 40 percent of an hour's traffic mix for a particular installation. The necessary parameters are input to a PL/1 program (SIMGEN) which generates an appropriate test tape (see Fig. 4). Currently, a library of test tapes is maintained, representing many different loads, message mixes, and test durations.

4.2 Test messages

Message-load and message-mix data is jointly forecasted by a Bell System operating telephone company and Bell Laboratories. This data determines specific message inputs that are made available to the

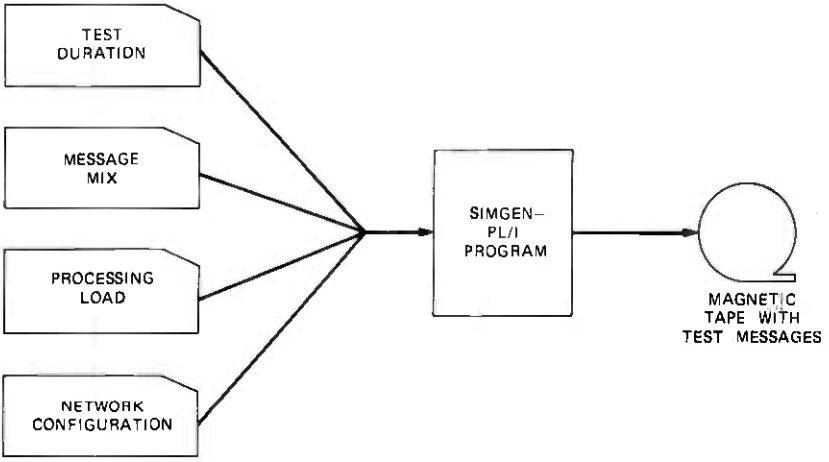

Fig. 4—Process of creating test-message tape.

driver system. These inputs are associated with the simulated terminals, and the driver system sends these messages to BISCOM at a controlled rate. Conversely, the messages sent to the primary system will stimulate activity and responses (i.e., deliveries of messages to simulated and real terminals); therefore, the rate at which the driver accepts messages from BISCOM must also be controlled. By establishing this control on the transmission and receipt of messages associated with the primary system, a load capability is created.

4.2.1 Test message format

A BISCOM message has the format

(SOH) Header (STX) Text (ETX).

This syntax does not change in the load driver although message processing is modified by the terminal simulators and format handlers.

The basic BISCOM format is expanded within the text portion to form the syntax of the test message

$$(\text{SOH})\ \frac{\text{DH}}{\text{HEADER}} \qquad (\text{STX})\ \frac{\text{CS}}{\text{*POL p}\quad \text{*SEL s}}\ \frac{\text{PH}}{\text{*SOH HEADER}}$$

$$\frac{\text{PT}}{\text{*REP r *STX TEXT *PAD d}}\ (\text{ETX}).$$

The test message is broken into four major sections: DH (Driver Header), CS (Control Section), PH (Primary Header), and PT (Primary Text). These message sections (*i*) direct test messages to driver-simulated terminals, (*ii*) control the responses of these terminals to

BISCOM polling and selection, and (*iii*) define the text patterns sent when positive poll responses are desired. Examples of various test messages are given in Appendix B.

4.2.2 DH (driver header) section

This section designates a simulated terminal in the load-driver network. Normal BISCOM mechanisms are used to queue the test message to a simulated terminal; however, instead of its normal delivery of the message to a real terminal, BISCOM releases all control over the message and activates the appropriate terminal simulator. The simulator, as part of its operation, will call the test-message format handler which reconstructs the message for delivery to the primary system.

4.2.3 CS (control section)

The test-message control section controls the response of the simulated terminals to poll and select sequences from the primary system. By regulating the time between positive polling or selection responses, it is possible to present any desired message-transfer rate to the primary system.

The *POL p and *SEL s subsections specify that a delay is to be introduced before either a positive *polling* response or a positive *selection* response is given. Polling and selection response delays stay in effect until reset by another test-message control section.

4.2.4 PH (primary header) section

Entries in this field may represent any valid BISCOM header information, as shown in Appendix A. When a terminal simulator is ready to give a positive response to a primary polling sequence, the *SOH will be converted to the (SOH) control character. The header has no processing performed on it and must correspond to valid primary network terminals and/or data-base operations.

4.2.5 PT (primary text) section

This section defines the text portion of the test message. As in the case of *SOH, the test message format handler converts the *STX to the (STX) control character and performs other operations on the TEXT subsection if specified by the *REP subsection. *REP r operates on the PT section and on the PH section simultaneously, *r* specifying how many times this particular message is to be repeated before the simulator releases it and goes to the next test message. The *REP subsection is also used in conjunction with a special character '#', which is used for sequence numbering.

The TEXT section may be alphanumeric strings of any length. *PAD d specifies how many repetitions of a 20-character "filler" sequence are to follow the TEXT subsection. In this manner, messages of varying lengths may be transferred to the Active system without the need to supply all the characters in the test message.

4.3 Measurement tools

The measurement tools available in the BISCOM test facility may be grouped into three categories:

(*i*) Hardware monitors
(*ii*) Software monitors
(*iii*) Logging analysis programs.

The use of these tools along with their advantages and shortcomings are discussed in the next section.

4.3.1 Hardware monitors

COMRESS Corporation's Dynaprobe® hardware monitors, models 7900 and 8000, are currently used in the test facility. These monitors are used to collect data concerning system hardware component activities; for example, they measure the number of seeks, reads, and writes performed by the disk subsystem; the amount of disk controller and disk pack utilizations; the amount of Central Processor utilization; and the amount of magnetic tape controller activity. The hardware monitors also have the capability of monitoring instruction-execution activity as a function of instruction address, making possible the production of "maps" of instruction activity by memory location (see Fig. 5). This capability has been particularly useful in locating anomalous program loops and in selecting program modules as candidates for code optimization.

A hardware monitor does not perturb the system being measured and thus does not bias the measurements made. In addition, hardware monitors have a certain amount of flexibility and provide a way to make measurements that are not readily attainable by other means, e.g., measuring instantaneous CPU utilization, core usage, and interrupt enable/disable times.

The data gathered by the hardware monitor is used in the validation of various simulation and forecasting models of BISCOM. There are, however, many software-related measurements that cannot be obtained by this method. For example, it is difficult to measure buffer utilizations, message processing times, and task activations. Software monitors must be used to measure this activity.

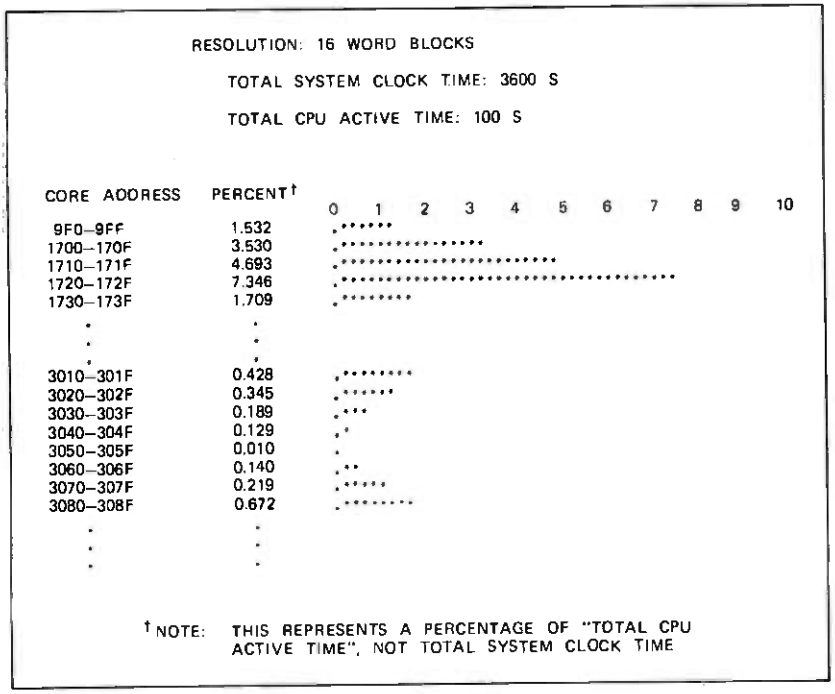

Fig. 5—Typical reduced output of hardware monitor.

4.3.2 Software monitors

There is limited software monitoring capability built into the Active system and Driver. The Driver software contains a statistics-gathering routine that periodically prints statistics on the network interactions with the Active BISCOM system. There is also an Active system software monitor routine that collects data on buffer pool utilizations, queue lengths for various processing tasks, and the number of messages entering and leaving the system during specified time intervals.

Significant system events are also logged on magnetic tape for use by the Recover system. In the test environment, these log tapes serve as inputs to an analysis program. This analysis program outputs statistics on message volumes and switch time (Table II); future plans call for reporting data-base activity and network performance through expanded system logging. Such logging is part of normal BISCOM operation, and the test facility makes use of already available data.

Two of the major advantages of software monitors over hardware monitors are the wider range of system attributes that can be measured and the greater flexibility in the control of data collection. One

Table II — Typical log analysis output

Message Type	Number of Messages	Average Resp-Time (s)	Average Chars In	Average Chars Out	Messages Delivered/ Cleared
POSM*	5	0.06	89.00	89.00	5
SMST	68	0.57	422.29	0.00	0
SMSD	64	1.89	424.87	424.87	152
SMRP	25	0.72	415.40	0.00	0
SMRD	103	1.32	530.04	530.04	146
SMCL	3	0.82	25.00	0.00	3
SMFT	129	0.52	25.00	516.25	129
SMDL	6	0.87	28.00	563.66	6

Window times: 02:55.34–03:00.34; window length: 5.00 minutes
No. messages = 403; 99.3% load; 100% input-message load = 4860 msgs/hr

* Straight switched messages.

of the disadvantages is that a software monitor interacts with normal system operation and thus uses some of the system's resources. Another disadvantage is that special data-reduction-and-analysis software must be developed for a software monitor.

Note that one use made of the hardware monitor is to estimate the impact of the software monitor operation on normal system processing; in particular, it is possible to determine how much CPU time the software monitor is using.

V. SOFTWARE TEST ACTIVITY AND SYSTEM CERTIFICATION

The tools comprising the test facility are being employed for software test purposes as well as for performance measurement and evaluation studies. The most heavily used aspect of the test-facility tool is the load-test capability. Whereas a load test is performed on *each release* of BISCOM prior to site installation, a measurement-and-evaluation effort is only applied to *selected releases* of the system. There are two major reasons for this:

(*i*) Data collection, reduction, and analysis is a costly process,
(*ii*) Software changes on a per-release basis usually do not warrant a complete measurement-and-evaluation effort. However, those releases that contain performance-affecting changes have full-scale measurement-and-evaluation procedures applied prior to site distribution.

The load test is the culmination of prerelease test activity on a given set of software changes. Prior to the load test, the software changes

are tested by the change originator for their functional correctness. The changes are then integrated into the BISCOM software, and the entire system is subjected to a standard test series. The final stage in the test procedure is the application of the load test.

As discussed in Section I, the load test has essentially three parameters: message mix, message load, and network. The message mix and related network configuration cause the software to react in different ways depending upon the processing requirements on a specific message type (designated by the message-header information). A message that requires a store into the data base has different requirements than a message that is switched directly from terminal to terminal. Likewise, messages that access different data files in the BISCOM system have different processing requirements. The message-load parameter allows an approximation to the message-processing load expected to be experienced in an actual operating environment. This processing load is jointly forecasted by a Bell System operating telephone company and Bell Laboratories. Beyond these parameters, system dependent variables can be stressed in a manner designed to cause system actions that are not normally met in a simple test. Typical variables stressed are buffer exhaustion and buffer boundary conditions.

The load test is the final test that is applied before release of the software product. Data analysis is performed and compared with the analysis of previously released systems in a search for any discrepancies that might point to a design flaw. This analysis also ensures that the system does not regress (from previously released systems) in load or functional capability.

After the software system is released, the load test is again used to exercise the released system on a continuous basis in search of design flaws or dormant software bugs. Exercising the system on a continuous basis involves activating the system and switching messages for several consecutive hours.

5.1 *Test results*

Test results to date can be classified into two categories, namely,

(*i*) Uncovering of software problems.
(*ii*) Certification of the system-load capacity.

The first category of test results includes an entire range of software problems. A typical example in this category was uncovered during system shutdown, the time during which the system cleans up traffic in progress, secures its data base, and transmits "good night" messages

to the terminal users. The system performed this function adequately when not under load; however, when shutdown was attempted in a loaded environment, it did not function properly. This condition was corrected before it occurred in a real environment.

Another example of category (*i*) is the saving of machine states when high-priority tasks preempt current system activity. The software associated with "state" saving and restoring operated correctly until stressed in a load-test environment. This condition was also corrected. Violations of reentrancy conditions in the data-management functions were also uncovered and corrected in the laboratory environment.

We also found that the load-test facility is capable of exercising the various hardware components to such an extent that it can cause the hardware (disk units, tape units, etc.) to fail and thus force the system to exercise its retry logic. This is highly important, since many hardware conditions and status responses are very difficult to create during normal system operation.

The second category of test results relates to the throughput or capacity of the system. The point has already been made that system capacity is dependent upon the three variables: message type and size, message load, and network configuration. The laboratory has a close approximation to these variables as they relate to several live installations. In this environment, it has been possible to certify the capability of the system to process future traffic loads for these installations. This has been very useful information for site planners, particularly as it affects plans for routing more traffic through the system.

VI. ACKNOWLEDGMENT

The work presented here has been the result of the efforts of many people associated with the BISCOM project. The authors wish to acknowledge all who have contributed to the design, development, and maintenance of this test facility.

APPENDIX A

Message Syntax

*A.1 Terminal-to-Terminal (Straight Switch)**

Messages may be sent between terminals, or to and from the message storage files. The general format of each message consists of heading and text sections framed by delimiters. The heading must be correctly structured, whereas the text section is "transparent" to BISCOM.

* This message type does not cause access of any system data files and is switched directly from an originating terminal to destination terminal or terminals.

(SOH) DAC1 DAC2 . . . DACn (STX) TEXT (ETX), where:

(1) DACi is any 1–8 alphanumeric terminal logical name.
(2) The DACs must be separated by blanks.
(3) The total number of characters between (SOH) and (ETX) must be less than 256.
(4) The total number of characters between (SOH) and (ETX) must be less than 6400.
(5) TEXT may be any string that does not include certain control characters [e.g., (SOH), (ETX), etc.].

A.2 Special Message File (SMF)

(SOH) SM**. DAC1 . . . DACn/MSGID/PAGE/DATE CONTROL MM-DD (STX) Text (ETX)

where ** indicates one of the following process codes:

ST—Store	FT—Fetch
SD—Store and Deliver	DL—Deliver
RP—Replace	CL—Clear
RD—Replace and Deliver	

MSGID (Message ID)

Associates a storage and retrieval key with the message in the data base, any alphanumeric string from 1 to 15 characters.

PAGE

Any number between 1 and 99; the last page is denoted by the suffix L (e.g., 10L); associates a multipage message with a single-message ID.

DATE CONTROL

D—Deliver on MM (month), DD (day) date, current year
P—Purge the message on the MM, DD date
C—Deliver and purge the message on MM, DD date.

Example:

Store a message in the SMF of one page under the key ID100, deliver this message to terminals 37ASR1, SAND1; purge the message on July 11 of the current year.

(SOH) SMSD. 37ASR1 SAND1/ID100/1L/P 7-11 (STX) TEXT (ETX)

Fetch the above message:

(SOH) SMFT. /ID100 (STX) (ETX) (The message will be delivered to the terminal initiating the fetch.)

The SMF is the most heavily used system data file. Other system files are: Authorized, Resend, Batch, Paging, and Error. They have syntax similar to the SMF.

APPENDIX B

Test Message Examples

Communication lines in a BISCOM system normally terminate in more than one terminal; however, it is assumed for purposes of this discussion that each line terminates in only one terminal with the logical names given in Fig. 3. Consider the following test messages queued to driver-simulated terminals; the # character specifies a field used by the driver for message-sequence numbering.

INPUT TO DRIVER TERMINAL LT1:

(SOH) LT1 (STX) *REP 100 *POL 350 *SEL 100 LT2 PT1 *STX Test A# # # (ETX).

Sent to BISCOM From Simulated Terminal LT1:

(SOH) LT2 PT1 (STX) Test A001 (ETX)
⋮ 350 ms between messages sent to BISCOM
(SOH) LT2 PT1 (STX) Test A100 (ETX).

Delivered to Simulated Terminal LT2:

(STX) Test A001 (ETX)
⋮ 100 ms between deliveries
(STX) Test A100 (ETX)

Delivered to Primary Real Terminal PT1:

(STX) Test A001 (ETX)
⋮
(STX) Test A100 (ETX).

The following example shows how a test message may be used for data base operations:

INPUT TO DRIVER TERMINAL LT1:

(SOH) LT1 (STX) *REP 9 *SOH SMSD. RT1 LT#/BTL# # *STX TEST # # (ETX):

Sent to BISCOM from Simulated Terminal LT1:

(SOH) SMSD . RT1 LT1/BTL01 (STX) TEST01 (ETX)
⋮
(SOH) SMSD . RT1 LT9/BTL09 (STX) TEST09 (ETX).

Stored in Primary System Special Message File (SMF):

TEST01 Stored under key BTL01

⋮

TEST09 Stored under key BTL09.

Delivered to Primary Real Terminal RT1:

(STX) TEST01 (ETX)

⋮

(STX) TEST09 (ETX).

Delivered to Simulated Terminals LT1–LT9:

(STX) TEST01 (ETX) to LT1

⋮

(STX) TEST09 (ETX) to LT9.

THE BELL SYSTEM TECHNICAL JOURNAL
Vol. 55, No. 7, September 1976
Printed in U.S.A.

Calculation of Multidisturber Crosstalk Probabilities—Application to Subscriber-Loop Gain

By P. M. LAPSA

(Manuscript received January 27, 1976)

The possibility that excessive crosstalk limits the application of gain to long voice-frequency loops was studied. This problem was examined by means of a probability model incorporating data on such random variables as activity coincidence of disturbing and disturbed subscribers, disturber volume level, coupling path loss, listener acuity, and various noise sources.

A new approach was used with regard to the probability distributions of random variables: the probability distributions were modelled in detail for the calculation of the necessary functions, sums, and functions of sums of random variables. Results showed that gain of 6 dB or less is acceptable, and 9 dB is unjustifiably excessive. The approach used provides the most accurate calculation possible with available data, and is anticipated to be convenient not only for similar crosstalk evaluations but also for other nongaussian probability problems.

I. INTRODUCTION

An important concern in speech transmission is the avoidance of crosstalk. When it is intelligible, it is a potential violation of the telephone subscriber's privacy; when not intelligible, it is nevertheless an annoyance, especially if syllabic in nature. In subscriber loop equipment, as a result of the permanent assignment of a pair to each customer, such crosstalk situations might tend to be dedicated to a specific disturbing talker and a specific disturbed listener, who might even be known to each other. Therefore, the random occurrences of intelligible crosstalk must be limited to a probability that is very small indeed.

On long voice-frequency subscriber loops, it is often desirable to overcome excessive attenuation of the voice signal by applying some gain at the central office. The higher signal level, however, increases the probability that intelligible crosstalk will be heard. The existing gain limit of 6 dB was suspected to be already the maximum possible

without risking excessive crosstalk probabilities. Therefore, desired increases to as much as 9 dB were considered problematic, and this analysis was undertaken to evaluate it.

Intelligible crosstalk results from a fortuitous combination of several random variables, such as the activity coincidence of disturbing and disturbed subscribers, disturber volume level, coupling path loss, listener acuity, and various noise sources. The ill-defined, stochastic nature of the problem has always necessitated various approximations. For the present analysis, an approach more exact than previously used was needed for two reasons. First, preliminary calculations with these conservative approximations yielded unfavorable results even for low values of gain. Second, the probabilities involved were extremely small. Therefore, if there was any way to justify more than 6-dB gain, the least conservative, most exact, calculation would be the most likely to do so.

Most of the complications in crosstalk problems arise from the difficulty of measuring and analyzing the probability distributions of the random variables; these make the problem in its entirety seem formidable indeed. Fortunately, because of its importance, past work has shed much light on the construction of a reasonable analytical framework and on the estimation of the distributions. Aspects of this study, especially those described in Sections 2.1 and 2.2, continue in the line of analysis used most recently by D. H. Morgen,[1] T. C. Spang, B. E. Davis, and M. G. Mugglin of Bell Laboratories.

The main new development in this paper is the calculation of crosstalk in terms of nongaussian probability distributions, where appropriate for improved accuracy. The data is therefore better represented than if approximating gaussian distributions had been fitted to it, a point especially significant when evaluating the extreme "tails" of distributions, as required in this case. The improvements arising from this approach include:

(*i*) The exact distribution of measured coupling losses can be considered, rather than an estimation based on worst-case coupling or other approximations.

(*ii*) The threshold for intelligibility can be represented as dependent on an exactly calculated "power sum" of noise sources.

(*iii*) Distributions can be truncated when appropriate, as for example at the 30-dBrnC noise limit. This avoids taking advantage of one plant deficiency, excessive noise, to mask another, excessive crosstalk.

The problem is addressed in terms of the general crosstalk probability model summarized in Section II. Section III explains in more

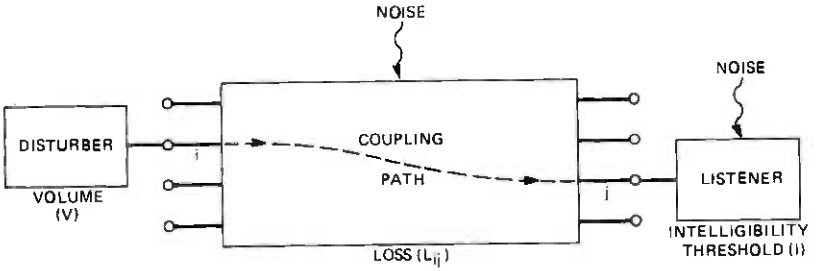

Fig. 1—General crosstalk coupling model.

detail the calculation of the total noise distribution from the distributions of the individual noise sources, after which the intelligibility threshold can be determined. The data for the distributions of random variables is discussed in Section IV, and Section V deals with some of the computational aspects involved. Finally, the results are discussed in Section VI.

II. GENERAL CROSSTALK PROBABILITY MODEL

2.1 The possibility of crosstalk

The essentials of the crosstalk problem can be described very simply and are depicted in Fig. 1. There is a disturber of volume V active on channel i, a disturbed subscriber is listening on channel j, and a coupling path with loss L^{ij} connects them. The listening acuity of the disturbed subscriber is characterized by his intelligibility threshold I.

Usually there are several possible coupling paths. Figure 2 shows the far-end and near-end crosstalk paths involved when voice-frequency gain is used on subscriber loops. However, it is easy to show that the far-end crosstalk probability is small (see Appendix A). The type of crosstalk path considered most likely to be disturbing with voice-

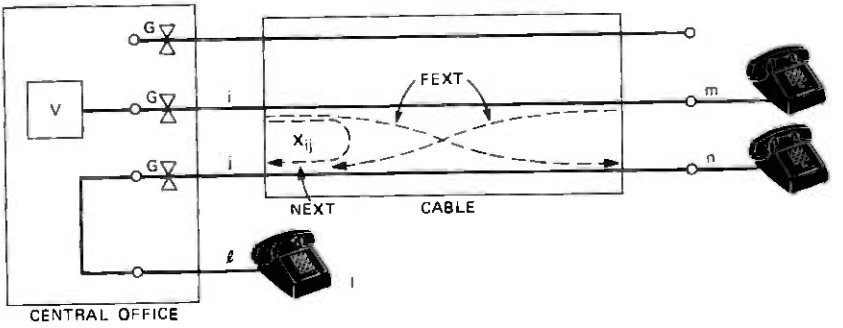

Fig. 2—VFG cable crosstalk coupling path.

frequency gain was near-end crosstalk (NEXT) at the central office (co) because the gain appears twice in the crosstalk path. Thus, L^{ij} in Fig. 2 is seen to include the coupling loss X^{ij} in the cable, reduced by twice the gain. When all quantities are expressed in dB,

$$L^{ij} = X^{ij} - 2G.$$

The disturbed listener is considered to be at zero loss from the co, so that crosstalk is most likely to be heard.

Crosstalk by way of the coupling path L^{ij} from disturbing pair $i \neq j$ to listener l is possible when both are active and subscriber l is using pair j. The probability of coincident activity of two independent channels has been usually given as

$$P_A^u = 1 - \left[\frac{\lambda}{\mu + \lambda}\right]^2, \tag{1}$$

where

μ = mean holding time of call,
λ = mean quiet interval between calls,
A denotes coincident activity.

This was a result of modeling holding times and quiet intervals as exponentially distributed; a derivation under more basic assumptions is presented in Appendix B. From (1), the probability of coincident activity for rural offices has been evaluated, assuming traffic to be somewhat heavier than average but uniformly distributed over all channels,

$$P_A^u = P_A = 0.167.$$

With P^{lj} denoting the probability that the disturbed subscriber l is using channel j, the probability that crosstalk can reach him by way of path L^{ij}, that is, the probability of coincident activity over the path, becomes

$$P_A^{ij} = P_A^u P^{lj}, \qquad i \neq j.$$

In this case, the subscribers on all cable pairs j were considered equally likely to be called by subscriber l, which leads to

$$P^{lj} = \frac{1}{N}$$

$$P_A^{ij} = P_A \cdot \frac{1}{N}. \tag{2}$$

It may be noted that both the talker volume and the noise distributions have been implicitly assumed to be identical and independent for all disturbers and paths, for which reason neither V nor N has

been carrying the superscripts i and j. There seems little reason to assume otherwise, although, if desired, V and N could be treated in a multidisturber context similar to that of L.

2.2 The intelligibility of crosstalk

The condition under which crosstalk over the path L^{ij} becomes intelligible to the disturbed subscriber is, in dB,

$$V - L^{ij} > I. \tag{3}$$

This relation can be elaborated to include the dependence of the intelligibility threshold I on the masking effect of all noise sources:[1]

(*i*) Circuit noise N_C
(*ii*) Room noise N_R
(*iii*) A fit parameter N_{TH} (which can be somewhat loosely interpreted as residual noise in the auditory system, defining the hearing threshold).

The total noise level is the sum of individual noise sources when expressed in units of power, rather than dB:

$$10^{N/10} = 10^{N_1/10} + 10^{N_2/10} + \cdots + 10^{N_K/10} = \sum_k 10^{N_k/10} \tag{4a}$$

or, in short,

$$N = N_1 +_p N_2 +_p \cdots +_p N_k, \tag{4b}$$

where the operator $+_p$ in (4b) is defined by (4a). In general, the noise sources must be specified not deterministically but rather by their probability distributions. The resulting distribution of the total noise level N can be calculated as described in Section III; we may assume for now that N is known. Then the intelligibility threshold I can be modeled as the following linear function of N (see Section 4.3),

$$I = I_0 + N. \tag{5}$$

Thus, the condition for crosstalk to be intelligible, eq. (3), becomes

$$V - L^{ij} > I_0 + N.$$

Now define*

$$R^{ij} \triangleq V - L^{ij} - I_0 - N. \tag{6}$$

Equation (3) is now

$$R^{ij} > 0. \tag{7}$$

* The case of gaussian random variables has been treated previously in detail, as for example in Ref. 1.

2.3 The probability of crosstalk

With that background, the probability of crosstalk over the path L^{ij} can be calculated as the product of the probability of coincident activity over that path times the probability of intelligible crosstalk when active,

$$P_C^{ij} = P_A^{ij} \cdot P_{C|A}^{ij}, \tag{8}$$

where

$$P_{C|A}^{ij} = \Pr\{R^{ij} > 0\}. \tag{9}$$

This can be evaluated by expressing the probability density function of R^{ij}, denoted by f_R^{ij}, in terms of the p.d.f.'s of V, L^{ij}, I_0, and N, denoted by f_V, f_L^{ij}, f_{I_0}, and f_N, respectively. By virtue of eq. (6), f_R^{ij} is the convolution

$$f_R^{ij} = f_V * f_{-L}^{ij} * f_{-I_0} * f_{-N}. \tag{10}$$

Restating eqs. (8) and (9) in terms of f_R^{ij},

$$P_C^{ij} = P_A^{ij} \int_0^\infty f_R^{ij}(R)dR. \tag{11}$$

There are $(N - 1)$ possible disturbers when the listener is on pair j. The probability that disturbers on pairs $i \neq j$ exceed the listener's intelligibility threshold is, therefore,

$$P_C^j = 1 - \prod_{i \neq j} (1 - P_C^{ij}).$$

The rare occurrences of babble due to two or more sufficiently loud disturbers are included. When P_C^{ij} are small, this reduces to

$$P_C^j = \sum_{i \neq j} P_C^{ij}.$$

Considering all N possible pairs used by l, the total probability of intelligible crosstalk to subscriber l is, again for small probabilities,

$$\begin{aligned} P_C &= \sum_{j=1}^{N} \sum_{i \neq j} P_C^{ij} \\ &= \sum_{j=1}^{N} \sum_{i \neq j} P_A^{ij} \int_0^\infty f_R^{ij}(R)dR \\ &= \sum_{j=1}^{N} \sum_{i \neq j} \frac{P_A}{N} \int_0^\infty f_R^{ij}(R)dR. \end{aligned} \tag{12}$$

As a result of the linearity of the convolution and integration operations, this double sum of integrals can be reduced to a very simple form. Returning to (6), we can define an intermediate random

variable

$$S \triangleq V - I_0 - N, \qquad f_S = f_V * f_{-I_0} * f_{-N}.$$

Thus,

$$R^{ij} \triangleq S - L^{ij}, \qquad f_R^{ij} = f_S * f_{-L}^{ij}.$$

Now (12) can be written as

$$P_C = (N-1)P_A \int_0^\infty f_S * \frac{1}{N(N-1)} \sum_{j=1}^{N} \sum_{i \neq j} f_{-L}^{ij}(R)dR.$$

The function

$$\frac{1}{N(N-1)} \sum_{j=1}^{N} \sum_{i \neq j} f_{-L}^{ij}(\cdot)$$

is simply the result of averaging the $N(N-1)$ individual p.d.f.'s f_{-L}^{ij} over all possible channel combinations $i \neq j$. Denote this averaged p.d.f. by f_{-L}:

$$f_L \triangleq \frac{1}{N(N-1)} \sum_{j=1}^{N} \sum_{i \neq j} f_L^{ij}.$$

Then

$$P_C = (N-1)P_A \int_0^\infty f_S * f_{-L}(R)dR.$$

For

$$R \triangleq V - I_0 - N - L, \qquad f_R = f_V * f_{-I_0} * f_{-N} * f_{-L}, \tag{13}$$

$$P_C = (N-1)P_A \int_0^\infty f_R(R)dR = (N-1)P_A[1 - F_R(0)], \tag{14}$$

where F_R is the probability distribution function of R.

The multidisturber case is thus greatly simplified to a result parallel to the case of a single disturbing path, eq. (11), but with f_R appropriately redefined by means of the average of the coupling loss p.d.f.'s. If all f_L^{ij} are identical, then of course,

$$f_L = f_L^{ij}$$

and eq. (14) differs from eq. (11) only by the factor $(N-1)$. For most cables, however, the f_L^{ij} may not be identical for all pair combinations (i, j), because there may be a strong dependence on distance, shielding due to intervening pairs, and twist-length ratios. Noting that it would be a formidable task to specify the individual f_L^{ij}, we proceed to show how $f_L(L)$ and the result (14) are easily available from a single overall cumulative distribution function.

Since no entirely satisfactory analytic derivation of the f_L^{ij} has yet been devised, the most fruitful approach is to use direct measurements

of the coupling losses in cables (more specifically identified as cable units, because within-unit crosstalk predominates). The measurements form a symmetric, off-diagonal matrix for each cable (or cable unit if within-unit coupling is of primary interest), as shown in Fig. 3. By merging these results over all cable units measured, a cumulative distribution function F_L^{ij} in each (i, j) cell can be constructed, from which

$$f_L^{ij}(L) = \frac{d}{dL}\,[F_L^{ij}(L)]$$

and

$$f_L(L) = \frac{d}{dL}\,[F_L(L)],$$

where F_L is the overall cumulative distribution function of all crosstalk measurements,

$$F_L(L) \triangleq \frac{1}{N(N-1)} \sum_{j=1}^{N} \sum_{i \neq j} F_L^{ij}(L).$$

Therefore, even though the distributions differ from cell to cell, it is not necessary to maintain the identities (i, j) of the measurements, a point which is most clearly evident when the distribution functions are expressed in terms of step-functions $u(\cdot)$ at the measured values. For K cable units measured,

$$\begin{aligned} F_L^{ij}(L) &= \frac{1}{K} \sum_{k=1}^{K} u(L - L_k^{ij}) \\ F_L(L) &= \frac{1}{N(N-1)K} \sum_{j=1}^{N} \sum_{i \neq j} \sum_{k=1}^{K} u(L - L_k^{ij}) \\ &= \frac{1}{M} \sum_{m=1}^{M} u(L - L_m), \end{aligned}$$

where $M = N(N-1)K$ and the single summation extends over all measurements of all pair combinations.

Section 4.2 points out that F_L may have arisen from two distinct populations, adjacent within-unit (WU) pairs and nonadjacent WU pairs. In that case, proceeding as above, we can model F_L to show this explicitly:

$$F_L(L) = \frac{A}{M} F_{L,a}(L) + \frac{M - A}{M} F_{L,n}(L), \tag{15}$$

where A is the number of adjacent pair measurements.

To summarize, the result (14) is parallel to the case of a single disturbing path in eq. (11), but with f_R appropriately redefined. Of the four functions constituting f_R, as shown in eq. (13), all but the noise power density f_N can be derived directly from measured data. The

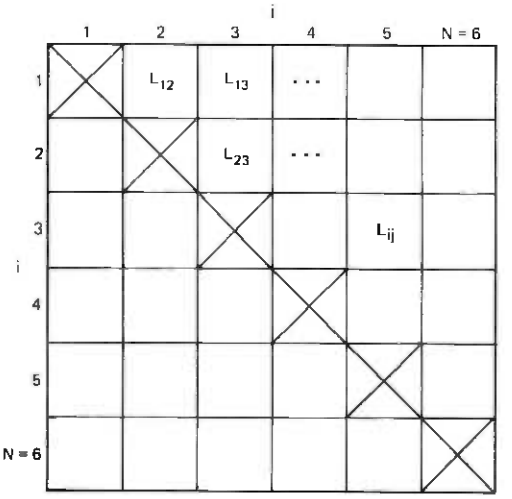

Fig. 3—Symmetric matrix of crosstalk coupling-loss measurements.

calculation of f_N is more complicated and is discussed in the next section.

III. NOISE POWER-SUM CALCULATION

It is necessary to evaluate the probability density of total noise power from stochastically independent noise sources. As summarized in eq. (4), the noise variables N_k, in dB, must be transformed to units of power, e.g., watts,

$$W_k = p(N_k) = 10^{N_k/10} \tag{16a}$$

so that they can be added.

Appendix C describes sums, functions, and general operator sums of independent random variables. To utilize these for the transforming function $p(\cdot)$, we only need to calculate its inverse and derivatives,

$$p^{-1}(W_k) = 10 \log_{10} W_k \tag{16b}$$

$$\frac{d}{dN_k} p(N_k) = \frac{\ln 10}{10} 10^{N_k/10} \tag{16c}$$

$$\frac{d}{dW_k} p^{-1}(W_k) = \frac{10}{\ln 10} \frac{1}{W_k}. \tag{16d}$$

The term N_k and its p.d.f. f_k thus transform as follows:

$$N_k, f_k(N_k) \Leftrightarrow W_k, g_k(W_k) = \frac{10}{\ln 10} \frac{1}{W_k} f_k(10 \log_{10} W_k). \tag{17}$$

Then the total noise power, in units of power, is

$$W = \sum_k W_k$$

and its p.d.f. $g(W)$ is the convolution of the g_k,

$$g = g_1 * \cdots * g_K.$$

To invert W back to dB, we use Appendix C with $u \equiv p^{-1}$ to obtain

$$\begin{aligned} N &= 10 \log_{10} W = 10 \log_{10} \sum_k W_k \\ &= 10 \log_{10} \sum_k 10^{N_k/10} \end{aligned} \tag{18}$$

and

$$\begin{aligned} f_N(N) &= \left\{ \frac{\ln 10}{10} 10^{N/10} \right\} g(10^{N/10}) \\ &= \left\{ \frac{\ln 10}{10} 10^{N/10} \right\} g_1 * \cdots * g_K(10^{N/10}). \end{aligned} \tag{19}$$

This, with the aid of eq. (17), defines the p.d.f. of total noise power.

The power sum convolution process can be summarized by applying it explicitly to noise sources mentioned in Section 2.2. As in Appendix C, the notation can be greatly simplified by introducing the symbol $*_p$ for this "power convolution," analogous to the "power sum" symbol $+_p$ in eq. (4b). Then eqs. (18) and (19) reduce to merely

$$N = N_C +_p N_R +_p N_{TH} \tag{20}$$

$$f_N = f_C *_p f_R *_p f_{TH}. \tag{21}$$

The next step is to describe some data for the random variables discussed: V, L, I_0, N_C, N_R, and N_{TH}.

IV. ESTIMATION OF THE PROBABILITY DISTRIBUTIONS

As mentioned in the preceding sections, the main random variables are talker volume, intelligibility threshold, coupling loss, and noise. Data for them was taken from the best surveys available at this time.

4.1 Talker volume

The 1960 survey of talker volume at central offices as reported by McAdoo[2] was used to model talker volume. Loudness of intraoffice calls varied substantially with the size of the co and local calling area, the means ranging from −19 VU (volume units) in New York City to −29 VU in Enid, Oklahoma. The figure actually used was −26 VU, as measured in Pascagoula, Mississippi, which has a population of 17,000 with 8000 station sets. This volume level was somewhat

below the survey's nationwide average of −24.8 VU, in recognition of the use of VFG (voice-frequency gain) primarily in the smaller communities.

The distribution about the −26 VU mean was modeled as normal with a standard deviation of 7.3 dB, as reported by the survey.

4.2 Coupling loss

Because crosstalk from within-unit (WU) pairs predominates overwhelmingly, the most accurate approach was to consider the distribution of WU coupling loss explicitly, rather than as a small tail of a merged distribution for all pairs in a cable. NEXT coupling loss data at voice frequency was available from Bell Laboratories measurements of an electrically long, 22-gauge, 100-pair, even-count PIC cable, comprising eight units of 12 and 13 pairs. Figure 4 shows the smoothed cumulative distribution function of 468 measurements in WU coupling-loss matrices.

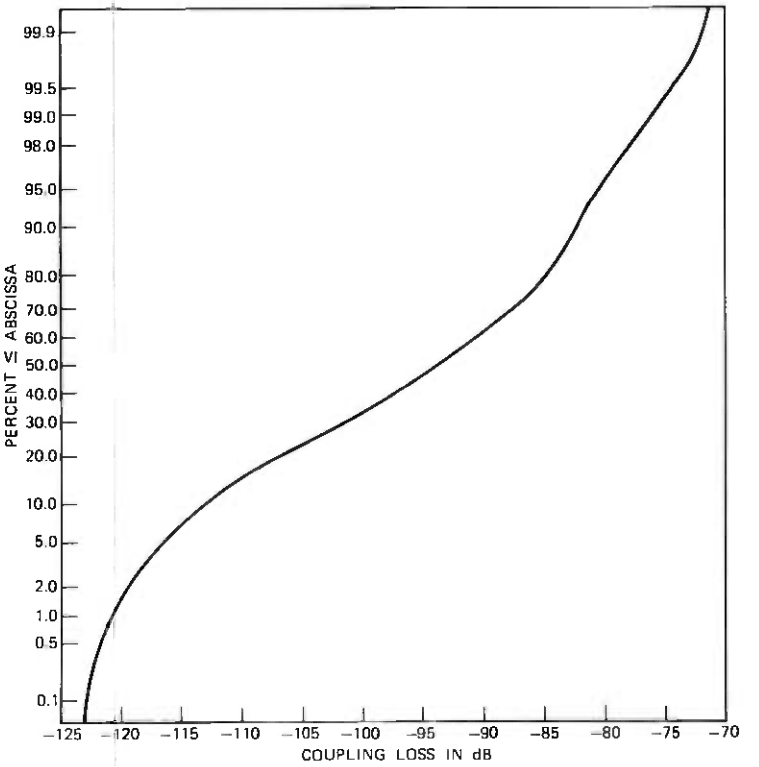

Fig. 4—Distribution of 1000-Hz NEXT coupling loss (dB).

Coupling loss is usually assumed to be log-normally distributed. If this were true of the above data, then it would appear as a straight line in Fig. 4. A possible explanation of why this is realized only approximately is that loss is not distributed uniformly for all pairs, but instead differs for two (or more) distinct populations: adjacent WU pairs and nonadjacent WU pairs. When this hypothesis was tested with some available data of coupling-loss measurements by South Central Bell, a substantial and consistent difference between adjacent-pair and nonadjacent-pair measurements was indeed found.

Therefore, the distribution function of Fig. 4 might be interpreted as a merging of a distribution for adjacent pairs and a distribution for nonadjacent pairs, as in eq. (15). The total distribution function was divided in proportion to the number of adjacent and nonadjacent measurements so that a truncated normal distribution function could be fitted to each part. The approximation gave results that agreed reasonably well with those calculated from the distribution of Fig. 4 exactly (see also Section V); in particular, the truncated normal fit to the low-loss tail, attributed to adjacent pairs, accounted for most of the crosstalk probability.

4.3 Intelligibility threshold

It was mentioned in Section 2.2 that the dependence of intelligibility threshold on total noise level is linear, as developed in Refs. 1 and 3. In this representation, eq. (5), I_0 was modeled as normally distributed in dB with a mean of -95 VU and a standard deviation of 2.5 dB, based on the subjective tests by Sen.[3] These values were determined in experiments in which coupling loss was flat with frequency. The threshold has been found to be slightly lower if coupling loss decreases with frequency; in case of a 6-dB-per-octave slope, sensitivity would be 2 dB greater for a male voice, or 1 dB greater for a female voice. However, in view of other conservative assumptions, this possible effect was neglected.

4.4 Noise sources

Section 3 described the total noise level as a power sum of circuit noise, room noise, and hearing-threshold noise. Their distributions were characterized as described below.

The circuit noise distribution was taken from data of the 1964 Loop Survey described by Gresh.[4] The data for long loops was used because this would be most appropriate to VFG. The distribution is very nearly normal in dB, with a mean of 17.5 dBrnC and a standard deviation of 14.85 dB. However, two adjustments had to be made. First, it is clear from Fig. 2 that the gain would amplify the noise,

so that the distribution had to be shifted by this amount. Second, a considerable fraction of the loops exceeded the immediate remedial action limit of 30 dBrnC. Although the excessive noise would very effectively mask crosstalk, it was deemed better to assume that either this plant deficiency has been already cleaned up (for example, by the introduction of ringer isolators), or else it will be done in the near future. Therefore, the distribution used was normal in dB (hence, log-normal in power, as described in Section III and Appendix D), truncated at 30 dBrnC, with a mean of (17.5 + gain) dBrnC, and a standard deviation of 14.85 dB.

For the noise fit parameter N_{TH}, the value was 12.3 dBrnC;* for room noise, a normal distribution with a mean of 45 dBt (dB relative to 20 μPa) and a standard deviation of 7 dB was used.[1] The conversion from dBt to equivalent dBrnC at the set terminals has been

$$45 \text{ dBt} \Rightarrow 11.5 \text{ dBrnC}.$$

Some tests indicate this to be a conservative estimate for mean room noise. However, it is not known whether its inherently different character may make it less masking than circuit noise, so that the conservatively low value of 11.5 dBrnC may be quite appropriate until further experiments are conducted.

V. COMPUTATIONAL ASPECTS

Conceptually, three main steps are involved. First, the "power convolution" of eq. (21) computes the noise power p.d.f. Second, this result is used in the (ordinary) convolution of eq. (13) to compute the p.d.f. of the intelligibility random variable. Finally, the crosstalk probability is easily obtained as the probability that this variable exceeds zero, eq. (14).

Except for very simple p.d.f.'s, such as the normal distributions of V and I_0, these calculations are very difficult to calculate by hand, yet very easy by computer. Consequently, a computer program implementing the calculations of Appendix C was used. It is thereby possible to calculate the p.d.f. of algebraic expressions of independent random variables and their differentiable, invertible transforms; the "power" transform is seen to be a simple special case in Section III. The convolutions involved were performed very conveniently by using a fast Fourier transform routine,[5] a method which is valid to the extent that the p.d.f.'s are well represented by the calculated discrete Fourier transforms.

* No variance was modeled for this parameter; however, as can be seen from eq. (5), the parameter I_0 does introduce variance due to subjective perceptual differences into the basic equation for the intelligibility threshold.

An advantage of the numerical, rather than analytic, approach is that the p.d.f.'s and transforms could be specified by any method expressible as a function, including the following:

(*i*) Analytic form
(*ii*) Table with analytic interpolation
(*iii*) Distribution of measurement values.

Thus, it is possible to carry out an accurate calculation even when the data is distributed arbitrarily in a way that does not suggest a precise analytic representation. It should be noted also that well-behaved analytic functions can exhibit near-pathological behavior when transformed, as for example in Appendix D, in which case, particular attention to overall numerical accuracy is advisable.

In short, crosstalk probabilities were easily calculated with the data of Section IV used in eqs. (21), (13), and (14), as a special case of Appendix C.

VI. DISCUSSION OF RESULTS

The crosstalk probability calculation involving the three main steps described in Section V was carried out for each value of VFG of interest: 0, 4, 6, and 9 dB. Figures 5 through 8 illustrate the components and results of convolutions in the 4-dB and 9-bB cases. Figures 5 and 6 will serve as an example for the discussion.

The circuit noise p.d.f. with peak at 17.5 dBrnC + 4 dB, the room noise p.d.f. with peak at 11.5 dBrnC, and the convolved total noise p.d.f. including the hearing threshold of 12.3 dBrnC are shown in Fig. 5 for the range 0 to 30 dBrnC. It can be seen that this result is substantially truncated not only near 30 dBrnC, due to truncating the circuit noise there, but also near 12.3 dBrnC, due to the hearing threshold. The latter "truncation," an evident result of the noise power sum, is significant in that it eliminates the possibility of extreme low-noise conditions that would otherwise contribute substantially to the crosstalk probability, or perhaps even dominate it.

Figure 6 shows the convolution of the density of total noise N with the volume above intelligibility $V - I_0$ and with crosstalk coupling loss L. The resulting density is that of the intelligibility random variable R, where $R > 0$ signifies the event that intelligible crosstalk is heard. The probability of this event, as in eq. (14), is shown in Table I for various cases. Results for the three coupling paths identified in Fig. 2 are listed. The NEXT $i \rightarrow l$ case is the one analyzed so far; the probabilities of the FEXT paths are comparatively small, as mentioned in Section 2.1 and analyzed in Appendix A.

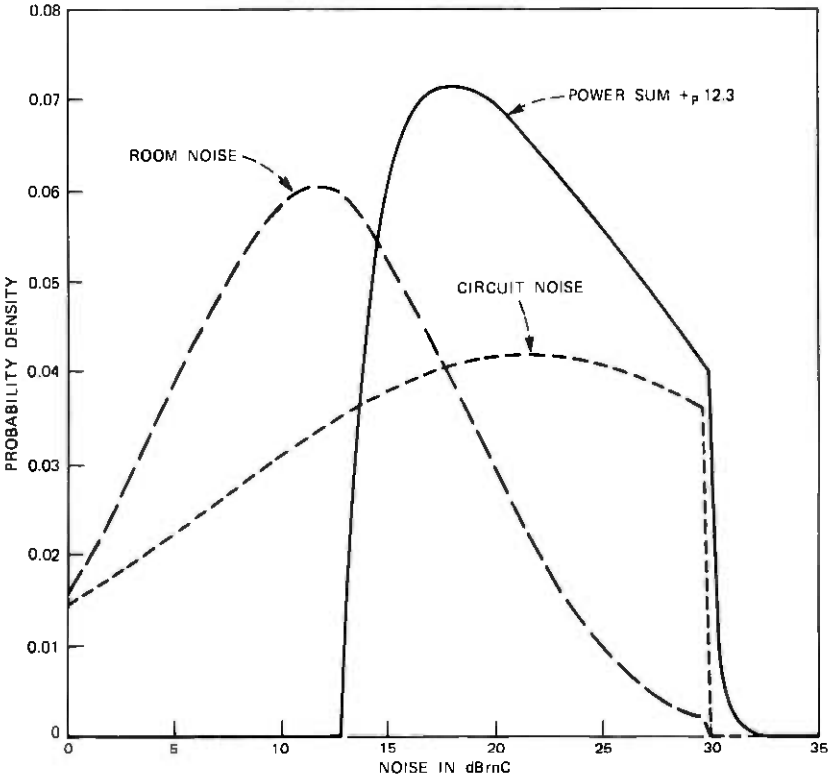

Fig. 5—Power sum of noise sources (gain = 4 dB).

These results show how rapidly the probability rises above the insignificant trace at 0 dB once gain is increased, a feature clearly depicted in Fig. 9. Although a firm objective for crosstalk probability in loop plant has not been established, this should be certainly less than the 1-percent objective for trunk calls because the condition would be dedicated to a particular customer. A probability of 0.1 percent has been used as a criterion.[1] Here we note that this is reached near 4 dB, and is greatly exceeded at 9 dB.

Table I — Probability of intelligible crosstalk

VFG (dB)	NEXT $i \rightarrow l$ (%)	FEXT $m \rightarrow l$ (%)	FEXT $i \rightarrow n$ (%)
0	<0.01	<0.01	<0.01
4	0.14	0.02	0.03
6	0.46	0.04	0.05
9	2.09	0.09	0.18

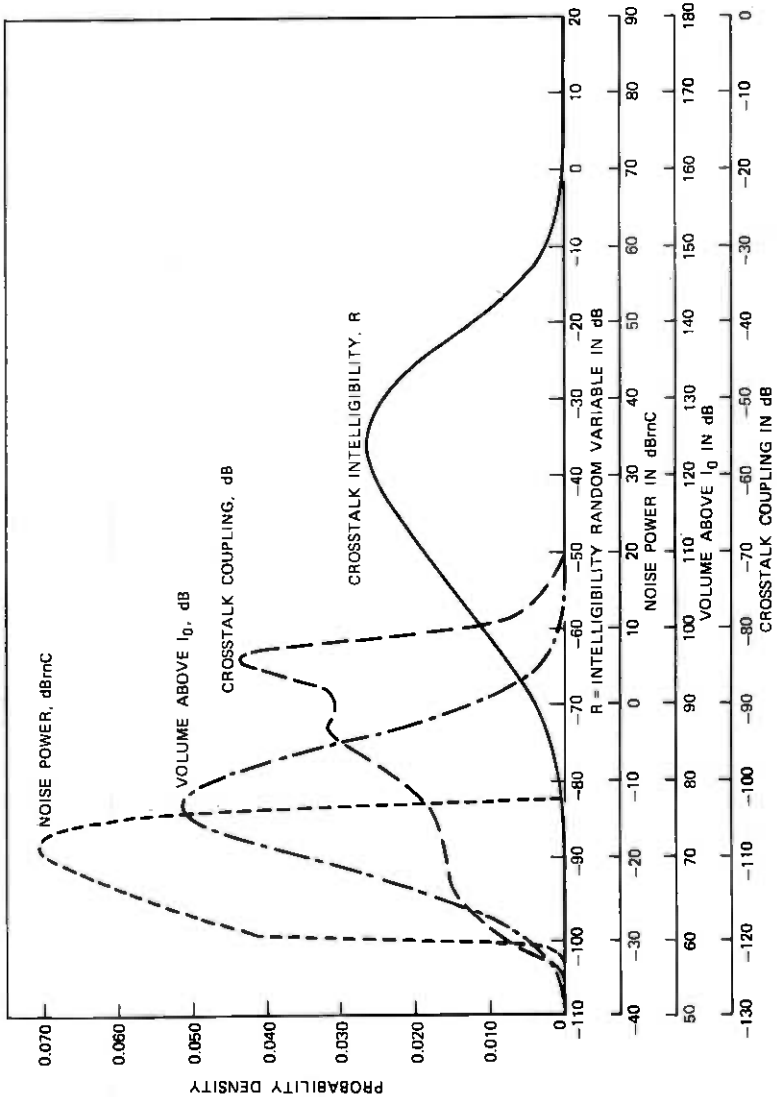

Fig. 6—Crosstalk intelligibility (gain = 4 dB).

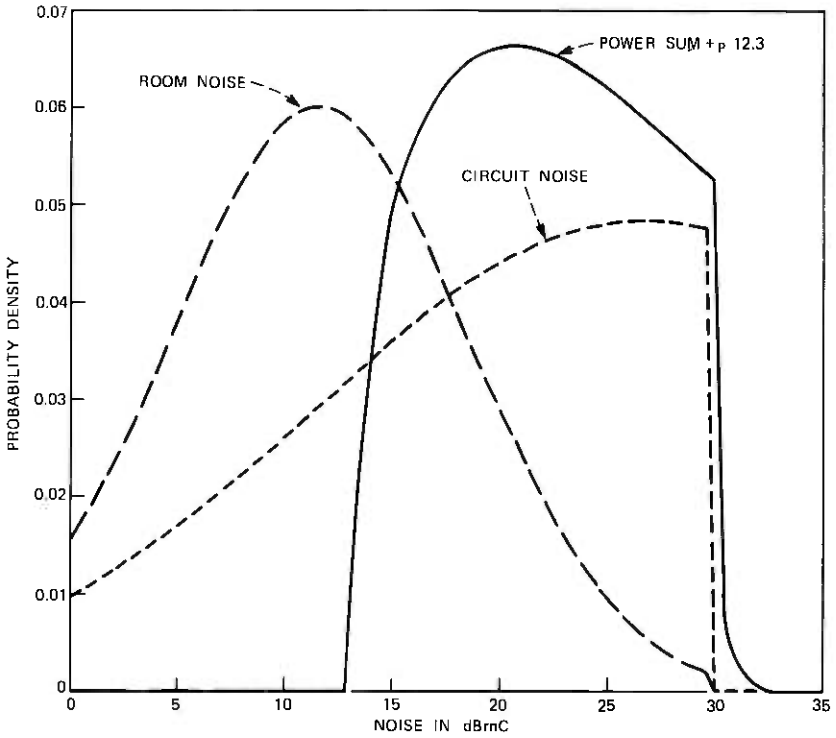

Fig. 7—Power sum of noise sources (gain = 9 dB).

The importance of extreme accuracy in calculation is now apparent. A calculation of the R distribution, which is "only" 99.9-percent accurate, could possibly rate the 4-dB case at *twice* its actual crosstalk probability. Figure 6 shows graphically how small the density is above $R = 0$. In the computer calculation, the precision can be increased as necessary by increasing the order of the fast Fourier transform, so the real limitation is the accuracy of the input data. In that, there is indeed room for further improvement, especially regarding the coupling-loss distribution, which is considered representative according to other measurements but was obtained from a single cable. The true masking effect of room noise should also be investigated further. Fortunately, more complete data are anticipated in the future, and it will be a trivial matter to recalculate the probabilities with this method. However, it is unlikely that the larger probabilities, such as for 9 dB, will turn out sufficiently smaller to be near 0.1 percent.

Four points must be emphasized. First, the crosstalk calculations were made with respect to the connections in Fig. 2—reasonable but

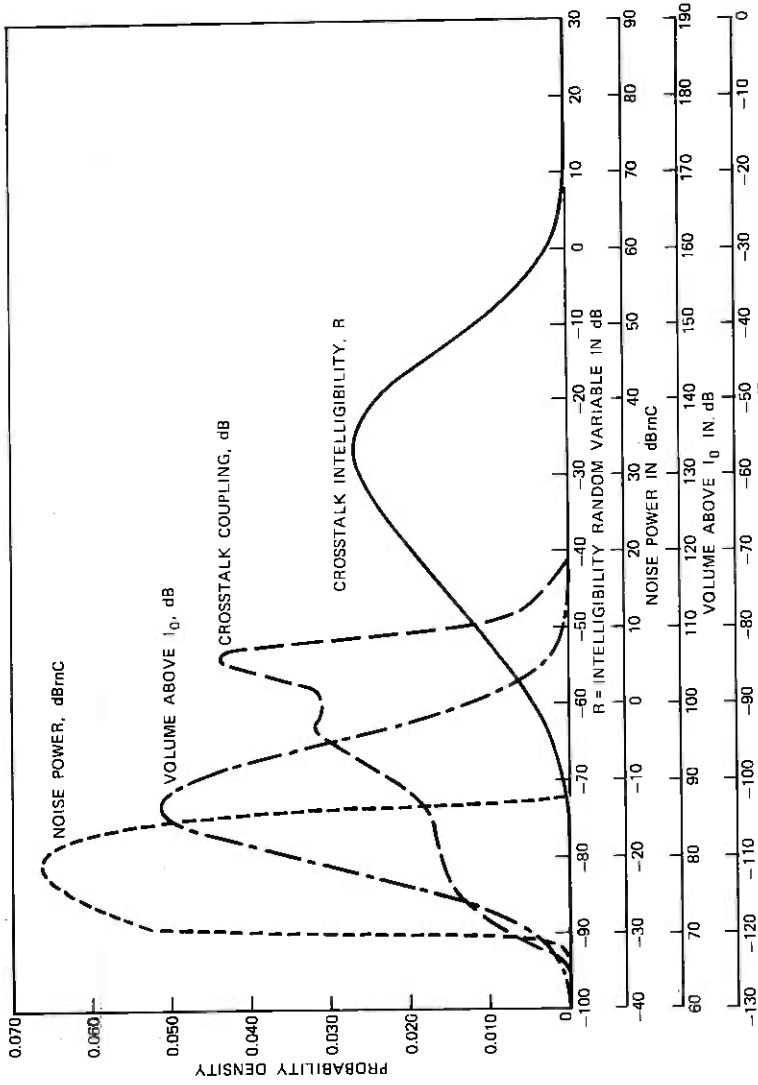

Fig. 8—Crosstalk intelligibility (gain = 9 dB).

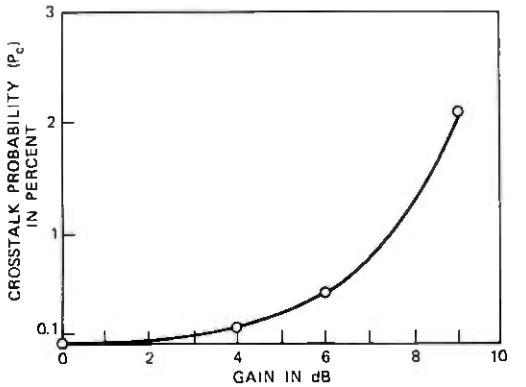

Fig. 9—Total crosstalk probability as a function of gain.

still arbitrary conditions; different conditions would yield different results. Second, the 0.1-percent criterion is intended to be applicable to plant that is fully dedicated to a particular customer. In Fig. 2, not all of customer *l*'s intraoffice calls would be to a community of interest served by VFG. Therefore, provided that the proportion of cables at a CO served by 6-dB gain is less than 20 percent of the cables without gain, the crosstalk probability experienced by the listener will be less than 0.1 percent. Since only 10 percent of the Bell System "long loops" (longer than 30 kft) exceed 60 kft, that degree of saturation is not considered likely; in this case, 6-dB gain is satisfactory. Third, the high noise level of long loops in the 1964 survey (truncated at 30 dBrnC) was used in the calculations. It is likely that extreme noise cases have been and will continue to be mitigated, with the unfortunate side effect of ultimately increasing crosstalk intelligibility. Finally, even under the high circuit-noise level used, the crosstalk probability for 9-dB gain considerably exceeds even the trunk-call objective.

VII. CONCLUSION

The subscriber loop VFG limitation due to probability of crosstalk was evaluated from available data on the random variables involved, including activity coincidence of disturber volume level, coupling-path loss, listener acuity, and various noise sources. Probability distributions which were nongaussian were represented in detail, and the necessary functions, sums, and functions of sums of random variables were calculated accordingly. The results, based on the best data available today, show that gain of 6 dB or less is acceptable and 9 dB is considerably excessive; the desirability of further, more extensive, data is thereby indicated. The method of calculation is independent of specific assumed forms of the distributions of random

variables and, hence, anticipated to be convenient not only for similar crosstalk evaluations requiring high accuracy, but also for other non-gaussian probability problems.

VIII. ACKNOWLEDGMENTS

The aid of J. T. Peoples was invaluable in resolving some vexing aspects of the computation method. The study also benefitted from the enlightening comments of many other colleagues at Bell Laboratories, most substantially D. H. Morgen, K. I. Park, and T. C. Spang. The author is grateful to all.

APPENDIX A

FEXT Calculation

Consider the FEXT coupling path shown in Fig. 2, from disturber i to listener n. The calculation is perhaps somewhat subtler than that for NEXT in the main study, because it is necessary to find the distribution of intelligible crosstalk probabilities that might be assigned to the listener, rather than a single value independent of assignment. For a fixed L^{ij}, eq. (11) may be written in terms of $S = V - I_0 - N$,

$$\begin{aligned} P_C^{in} &= P_A^{in} \int_0^\infty f_S(R + L^{in}) dR \\ &= P_A \int_{L^{in}}^\infty f_S(S) dS \\ &= P_A[1 - F_S(L^{in})]. \end{aligned} \tag{22}$$

When subscriber n is assigned his pair, he is in effect assigned the coupling loss L^{in}, from some distribution F_L^{in}, and a resulting P_C^{in}. Denote by F_C^{in} this distribution of crosstalk probabilities:

$$\begin{aligned} F_C^{in}(C^{in}) &= P\{P_C^{in} \leqq C^{in}\} \\ &= P\left\{L^{in} \geqq F_S^{-1}\left(1 - \frac{C^{in}}{P_A}\right)\right\} \\ &= F_L^{in}\left[-F_S^{-1}\left(1 - \frac{C^{in}}{P_A}\right)\right]. \end{aligned} \tag{23}$$

Moreover, the disturbed subscriber n will be subject to $N - 1$ such coupling paths. If the individual C^{in} are small, then the total crosstalk probability is approximately

$$C^n = \sum_{i \neq n} C^{in} \tag{24a}$$

with density

$$f_C^n = f_C^{1n} * \ldots * f_C^{in} * \ldots * f_C^{Nn}, \; n, \qquad i \neq n \tag{24b}$$

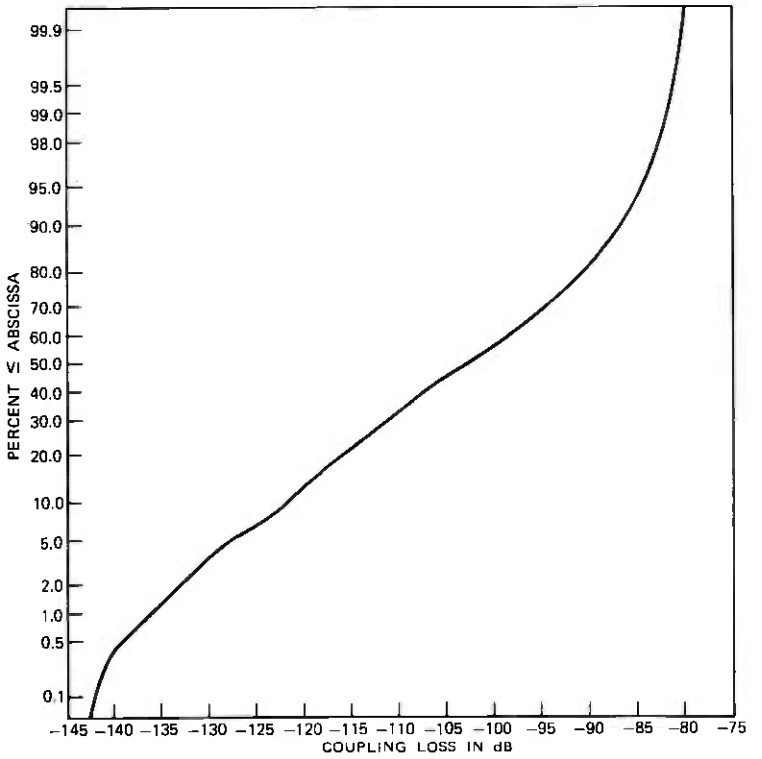

Fig. 10—Distribution of 1000-Hz FEXT coupling loss (dB).

and distribution

$$F_C^n = \int_{-\infty}^{C} f_C^n(C)dC. \tag{24c}$$

Thus, the desired distribution of FEXT probabilities assigned to the subscribers has been determined.

Instead of this calculation, some insight is often gained by evaluating (22) with L^{in} having a fixed value at the worst 1-percent of the coupling-loss distribution. Several sets of past measurements show that the 1-percent worst coupling loss is well estimated to be 84 dB at 6 kft. The loss at other lengths, including gain at the central office, is[6]

$$L^{in}(l) = 84 \text{ dB} - 10 \log_{10}\left(\frac{l}{6 \text{ kft}}\right) + \alpha l - G,$$

where l is the cable length, and α is the attenuation per unit length. The lowest-loss application of 6-dB gain has been for 2000 ohms of

22-gauge cable. This amounts to 11.5 miles, at which length the loss is 9.3 dB.[6] Thus

$$L^{ij}(60.8 \text{ kft}) = 77.24.$$

Using this value, P_c^{in} evaluates as a negligible 0.01 percent. Similar estimates for other gain values are shown below.

We now return to the exact calculation, eqs. (22) through (24). Within-unit FEXT coupling-loss data similar to the NEXT data of Section 4.2 is shown in Fig. 10. However, now the individual distributions F_L^{ij} are required, rather than their merged cumulative distribution as before. Therefore, the calculation is possible only at the price of assuming that the L^{in} are independent and identically distributed according to Fig. 10. The resulting distribution of FEXT probabilities is shown in Fig. 11 for 6-dB gain. It can be seen that the probability of assigning a 0.1 percent or greater FEXT probability to a subscriber is less 0.1 percent.

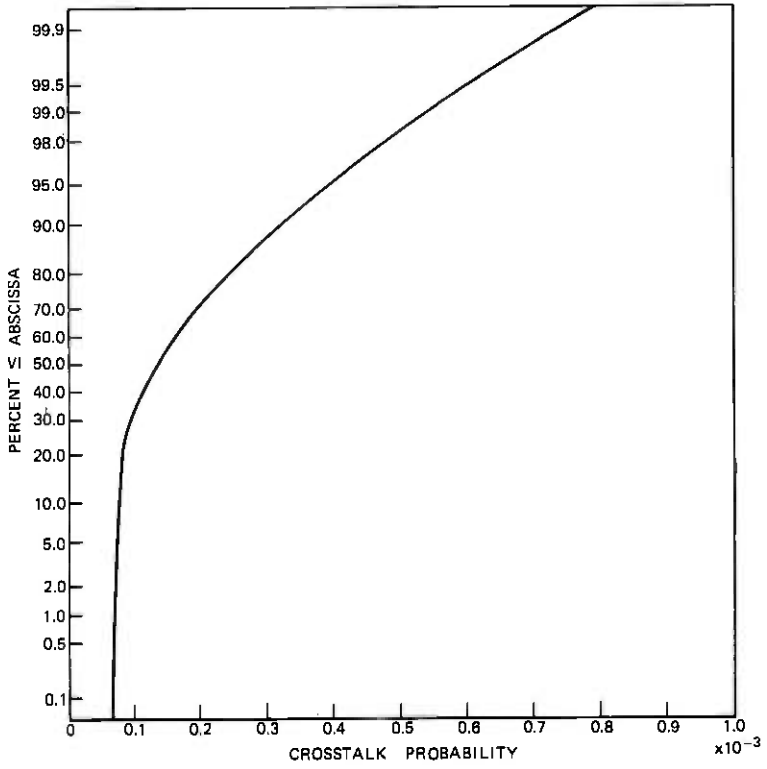

Fig. 11—Distribution of far-end crosstalk probabilities.

Table II — FEXT probability

VFG (dB)	Distributed Loss (%)	1% Worst Loss (%)
0	<0.01	<0.01
4	0.03	<0.01
6	0.05	0.01
9	0.18	0.03

Similar calculations were performed for the other values of gain. Because it is somewhat unwieldy to compare distributions, the 1-percent worst assignment resulting from the distributed coupling loss is specified in Table II. The estimation based on 1-percent worst coupling loss is also shown; both indicate negligible probabilities.

The FEXT coupling path from disturber m to listener l also yielded small crosstalk probabilities. These results are summarized in Section VI.

APPENDIX B

Probability of Coincident Activity of Two Channels

Channels a and b will be assumed to have calls initiated and terminated independently, with the simple assumption that the probabilities of these events during small time increments are proportional to the length of these increments. The quiet intervals and the call holding times will be shown to be exponentially distributed, as in Ref. 7 for a Poisson counting process.

To derive the distribution of quiet intervals, let

$$P_0(x_1, x_2) = \Pr\{\text{No call is initiated in } [x_1, x_2) \mid x_1 \text{ is in a quiet interval}\}.$$

Assume that, as in a Poisson process, the probability of initiation during a time interval Δx is proportional to an initiation-rate parameter $1/\lambda$ except for higher-order terms $0(\Delta x)$,

$$1 - P_0(x, x + \Delta x) = \frac{1}{\lambda}\Delta x + 0(\Delta x) \qquad \forall x \geqq 0, \Delta x \geqq 0.$$

The probability of no initiation in $[0, x + \Delta x)$ is then

$$\begin{aligned} P_0(0, x + \Delta x) &= P_0(0, x)P_0(x, x + \Delta x) \\ &= P_0(0, x)\left[1 - \frac{1}{\lambda}\Delta x - 0(\Delta x)\right] \\ \frac{P_0(0, x + \Delta x) - P_0(0, x)}{\Delta x} &= -\frac{1}{\lambda}P_0(0, x) - P_0(0, x)\frac{0(\Delta x)}{\Delta x}. \end{aligned}$$

In the limit as $\Delta x \to 0$,

$$\frac{dP_0(0, x)}{dx} = -\frac{1}{\lambda} P_0(0, x),$$

which has the solution

$$P_0(0, x) = e^{-x/\lambda} \qquad x \geqq 0.$$

The probability of initiation in $[x, x + \Delta x)$, with no initiation in $[0, x)$, is then

$$\begin{aligned} P_1(x, x + \Delta x) &= P_0(0, x)[1 - P_0(x, x + \Delta)] \\ &= P_0(0, x) \left[\frac{1}{\lambda} \Delta x + 0(\Delta x) \right]. \end{aligned}$$

This is the probability that the quiet interval after time 0 has a length between x and $x + \Delta x$. Denoting the probability distribution function of these quiet interval lengths by F,

$$\frac{\Delta F(x)}{\Delta x} = \frac{P_1(x, x + \Delta x)}{\Delta x} = P_0(0, x) \frac{1}{\lambda} + \frac{0(\Delta x)}{\Delta x} P_0(0, x).$$

The probability density function of these quiet interval lengths is the limit as $\Delta x \to 0$,

$$f_x(x) = \lim_{\Delta x \to 0} \frac{\Delta F(x)}{\Delta x} = \frac{1}{\lambda} P_0(0, x) = \frac{1}{\lambda} e^{-x/\lambda} \qquad x \geqq 0. \tag{25}$$

Similarly, given that a channel is active at time 0, the probability density function of a call termination at time y is determined from the termination-rate parameter $1/\mu$,

$$f_y(y) = \begin{cases} \frac{1}{\mu} e^{-y/\mu}, & y \geqq 0 \\ 0, & y < 0 \end{cases}. \tag{26}$$

The mean quiet interval is

$$\int_{-\infty}^{\infty} x f_x(x) dx = \int_0^{\infty} \frac{x}{\lambda} e^{-x/\lambda} dx = \lambda.$$

Similarly, the mean active interval is μ.

The probability to be derived is that of activity on channel b during some portion of a single call on channel a. This is most easily done by first calculating the probability of avoiding such coincidence.

First, the probability that channel a initiates the call during one of b's quiet intervals is

$$\frac{\lambda}{\mu + \lambda}. \tag{27}$$

Next, let y be the time interval from this initiation to the end of a's call, and x be the time interval from this initiation to the end of b's quiet interval. Then activity coincidence is avoided if

$$x \geqq y. \tag{28}$$

Define

$$z = x - y,$$

so that (28) is the event

$$z \geqq 0. \tag{29}$$

The p.d.f. of z is

$$f_z(z) = f_x * f_{-y}(z) = \int_{-\infty}^{\infty} f_x(x) f_{-y}(z - x)dx.$$

From (25) and (26),

$$\begin{aligned} f_z(z) &= \int_z^{\infty} \frac{1}{\lambda} e^{-x/\lambda} \frac{1}{\mu} e^{(z-x)/\mu} dx, \qquad \text{for} \quad z \geqq 0 \\ &= \frac{1}{\lambda\mu} e^{z/\mu} \int_z^{\infty} e^{-x[(1/\lambda)+(1/\mu)]} dx \\ &= \frac{1}{\lambda + \mu} e^{-z/\lambda}. \end{aligned} \tag{30}$$

From (27) and (29), the probability of avoiding coincident activity is

$$\begin{aligned} 1 - P_A^{ab} &= \left[\frac{\lambda}{\mu + \lambda}\right] \int_0^{\infty} f_z(z) dz \\ 1 - P_A^{ab} &= \left[\frac{\lambda}{\mu + \lambda}\right] \int_0^{\infty} \frac{1}{\lambda + \mu} e^{-z/\lambda} dz \\ &= \left[\frac{\lambda}{\mu + \lambda}\right]^2. \end{aligned}$$

Thus,

$$P_A^{ab} = 1 - \left[\frac{\lambda}{\mu + \lambda}\right]^2.$$

It should be noted that this is a conditional probability describing the event of coincidence given that channel a is active. In other words, this is the probability that b is active during any portion or portions of precisely one call by a. It is necessary to be aware of just how "probability of coincident activity" is defined to avoid ambiguous or misleading results.

APPENDIX C

Functions and Operator Sums of Independent Random Variables

Let X be a random variable with p.d.f. $f(X)$. Let $u(\cdot)$ be an invertible function such that u and its inverse are differentiable. Then

the p.d.f. of

$$Y = u(X)$$

denoted by $g(Y)$ is easily found as follows:

$$\Pr\{y \leqq Y\} = \Pr\{u(x) \leqq Y\} = \Pr\{x \leqq u^{-1}(Y)\}$$

$$= \int_{-\infty}^{u^{-1}(Y)} f(X)dX$$

$$g(Y) = \frac{d}{dY}\int_{-\infty}^{u^{-1}(Y)} f(X)dX = \left[\frac{d}{dY}\,u^{-1}(Y)\right] f[u^{-1}(Y)]. \quad (31)$$

Now consider the problem of finding the p.d.f. of a random variable that is the inverse function of the sum of a function of several random variables,

$$X = u^{-1}[u(X_1) + \cdots + u(X_n)] = u^{-1}[\sum_i u(X_i)], \quad (32)$$

with the p.d.f. of X_i denoted by f_i. The first step is to find the p.d.f. of

$$Y_i = u(X_i), \quad (33)$$

which is

$$g_i(Y_i) = \left[\frac{d}{du}\,u^{-1}(Y_i)\right] f[u^{-1}(Y_i)]. \quad (34)$$

Then the p.d.f. of

$$Y = \sum_i Y_i \quad (35)$$

is the convolution

$$g(Y) = g_1 * \cdots * g_n(Y), \quad (36)$$

and the p.d.f. of $X = u^{-1}(Y)$ is, by applying eq. (31) with $u(\cdot)$ replaced by $u^{-1}(\cdot)$,

$$f(X) = \left[\frac{d}{dX}\,u(X)\right] g[u(X)]. \quad (37)$$

The calculations (32) through (37) are much more conveniently expressed by defining an operator $+_u$ analogous to $+$, to deal with the function $u(\cdot)$:

$$(X_a) +_u (X_b) \triangleq u^{-1}[u(X_a) + u(X_b)].$$

Similarly, the extended convolution $*_u$ is defined by eqs. (34), (36), and (37). Then all of (32) through (37) can be expressed as

$$X = X_1 +_u \cdots +_u X_n$$

$$f(X) = f_1 *_u \cdots *_u f_n.$$

Section III illustrates the convenience of this notation in the case of power sums. Another important application is the multiplication of random variables,

$$X = X_a \cdot X_b = e^{\log X_a + \log X_b} = X_a +_m X_b,$$

where the function $m(\cdot)$ is defined as

$$m(X) = \log X,$$

which is invertible and differentiable as required. Thus,

$$f(X) = f_a *_m f_b.$$

Since both addition and multiplication are covered, it is possible to calculate in this manner the p.d.f. of algebraic expressions of independent random variables and their differentiable, invertible transforms.

APPENDIX D

Some Pathological Aspects of Power-Summing Random Variables with Large Variances

When the variances of gaussian random variables in a power sum are *small* compared to the means, it is easy to see that the power function will not substantially distort their distributions. With $p(\cdot)$ defined as in Section III,

$$Y = p(X) = 10^{X/10}, \qquad X = q(Y) = p^{-1}(Y) = 10 \log_{10} Y.$$

The term Y can be normalized with respect to its mean μ and standard deviation σ if the variance is finite:

$$\mathbf{Y} \triangleq \frac{Y - \mu}{\sigma}$$

$$X = q(Y) = 10 \log_{10} (\mu + \sigma \mathbf{Y}) = \mathbf{q}(\mathbf{Y}).$$

If $N(X)$ is the normal c.d.f. of X, and $G(\mathbf{Y})$ the c.d.f. of $\mathbf{Y}$, by Appendix C they are related as follows,

$$G(\mathbf{Y}) = N[\mathbf{q}(\mathbf{Y})].$$

Expanding around $\mathbf{Y} = 0$,

$$\mathbf{q}(\mathbf{Y}) = \mathbf{q}(0) + \frac{d\mathbf{q}}{d\mathbf{Y}}(0)\mathbf{Y} \quad \text{with error} < \left|\frac{d^2\mathbf{q}}{d\mathbf{Y}^2}(0)\mathbf{Y}^2\right|$$

$$\mathbf{q}(\mathbf{Y}) = 10 \log_{10} \mu + \frac{10\sigma}{\ln 10 \mu}\mathbf{Y} \quad \text{with error} < \frac{10}{\ln 10}\left(\frac{\sigma}{\mu}\right)^2 \mathbf{Y}^2.$$

Thus, for $|\sigma/\mu|$ small $\mathbf{q}$ is approximately linear, and the c.d.f. of $\mathbf{Y}$

may be expected to approach

$$G(Y) = N\left(10\log_{10}\mu + \frac{10\sigma}{\ln 10\mu}\,Y\right),$$

which is normal also.

An entirely different situation exists when the variances are *large* compared to the means. As an example, consider the distribution of circuit noise N_C from Section IV, which is normal in dB with p.d.f.

$$F_C(N_C) = \frac{1}{\sqrt{2\pi}\sigma}\exp[-(N_C-\mu)^2/2\sigma^2], \qquad \mu = 17.5, \quad \sigma = 14.85.$$

Applying $p(\cdot)$ to find the density in units of power,

$$\begin{aligned} g_C(W_C) &= \frac{10}{\ln 10}\frac{1}{W_C}f_C(10\log_{10}W_C) \\ &= \frac{10}{\ln 10}\frac{1}{\sqrt{2\pi}\sigma}\frac{1}{W_C}\exp[-\{(10\log_{10}W_C-\mu)^2/2\sigma^2\}]. \end{aligned}$$

To show that this density is extremely skewed, we find its maximum by differentiating,

$$\begin{aligned} \frac{dg_C(W_C)}{dW_C} = \frac{10}{\ln 10}\frac{1}{\sqrt{2\pi}\sigma}\Bigg[&\frac{1}{W_C}\left(-\frac{1}{\sigma^2}\right)(10\log_{10}W_C-\mu) \\ &\cdot\left(\frac{10}{\ln 10}\frac{1}{W_C}\right)-\frac{1}{W_C^2}\Bigg]\exp[-\{(10\log_{10}W_C-\mu)^2/2\sigma^2\}]. \end{aligned}$$

This is zero at

$$W_{C\,\mathrm{Max}} = 10^{[\mu-\sigma^2(\ln 10/10)]/10} = 10^{[17.5-14.85^2(\ln 10/10)]/10} = 0.0005.$$

Now the *median* value of g_C is at

$$W_{C\,\mathrm{Med}} = p(\mu) = 10^{\mu/10} = 10^{17.5/10} = 87.5.$$

The large difference between the mode and the median indicates the function's skewness.

A graph of g_C up to the truncation point 30 dBrnC would show very little, but the salient features are depicted in Fig. 12, which has the scale broken and expanded at $W_C = 10$ and 0.003 so that some detail is visible. It can be seen that g_C is less than 10 percent of the maximum over almost all of the range 0 to 1000.0, but rises sharply for values near zero.

Because of the difference between the mode and the median of g_C, it can be concluded that neither a normal density at the median nor an impulse at the maximum would be a very good approximation.

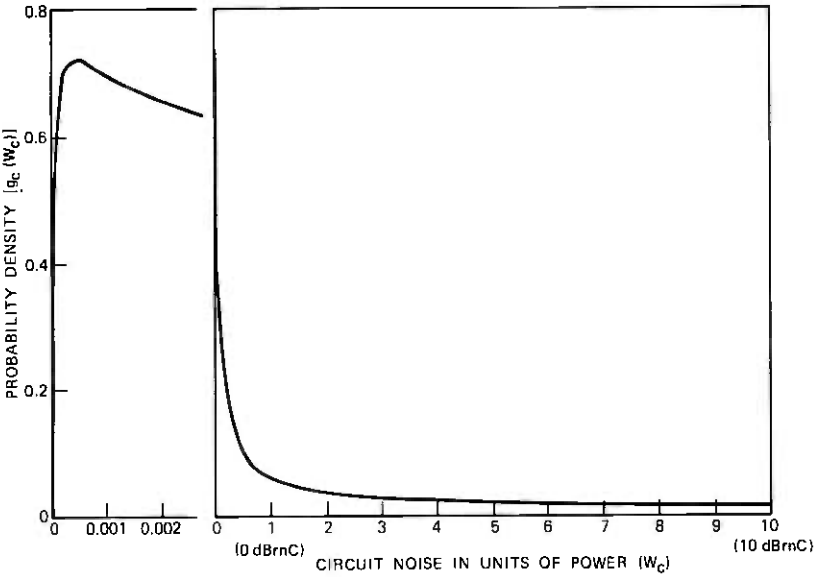

Fig. 12—Circuit noise density on expanded scales.

The former would underestimate the density at the low-noise tail, whereas the latter would overestimate it.

REFERENCES

1. D. H. Morgen, "Expected Crosstalk Performance of Analog Multichannel Subscriber Carrier Systems," IEEE Trans. Commun., *COM-23*, No. 2 (February 1975), pp. 240–245.
2. K. L. McAdoo, "Speech Volumes on Bell System Message Circuits—1960 Survey," B.S.T.J., *42*, No. 5 (September 1963), pp. 1999–2012.
3. T. L. Sen, "Masking of Crosstalk by Speech and Noise," B.S.T.J., *49*, No. 4 (April 1970), pp. 561–584.
4. P. A. Gresh, "Physical and Transmission Characteristics of Customer Loop Plant," B.S.T.J., *48*, No. 10 (December 1969), pp. 3337–3385.
5. J. T. Peoples, personal communication, 1975.
6. Members of the Technical Staff, Bell Laboratories, *Transmission Systems for Communications*, Revised Fourth Edition, February 1970.
7. W. B. Davenport, Jr., *Probability and Random Processes*, New York: McGraw-Hill, 1970.

THE BELL SYSTEM TECHNICAL JOURNAL
Vol. 55, No. 7, September 1976
Printed in U.S.A.

Offset and Tilt Loss in Optical Fiber Splices

By D. GLOGE

(Manuscript received March 8, 1976)

Transverse offset and angular misalignment (tilt) are serious causes of loss in multimode fiber splices. Our computation of these losses in multimode graded-index fibers reveals that the loss depends strongly on the power distribution in the fiber. We find that offsets of 0.1 of the core radius (or tilts of 0.1 of the fiber numerical aperture) cause a loss of 0.1 dB in the case of steady-state conditions, and between 0.34 and 0.38 dB if the power distribution is assumed as uniform. We compare these results with measured offset loss values and conclude that the steady-state distribution better reflects transmission line conditions than the uniform distribution.

I. INTRODUCTION

Fiber transmission lines will frequently have more than 10 splices between terminal points; to estimate the overall line loss, we need a reliable figure for the splice loss to be expected under varying line conditions. The loss in multimode fiber splices depends on the power distribution among the modes in the fiber. The difficulty of correctly simulating line conditions in laboratory measurements or computations has so far prevented the establishment of a reliable splice-loss estimate. Calculations have predicted as much as 0.4 dB for a 10-percent relative offset (offset divided by the core radius). These calculations assumed an equal or uniform power distribution in all modes.[1] Techniques used to measure the offset loss have attempted to simulate the equal-power condition by illuminating the full numerical aperture of the input fiber by a coherent source,[1,2] but the resulting loss values were between 0.1 and 0.2 dB for a 10-percent offset. The question has been raised whether some of the discrepancies are attributable to leaky rays.

The following study considers lateral offset and angular misalignment (tilt) of splices made from perfectly similar fibers by joining them without air gap. As an introduction to the subject, we derive simplified offset-loss formulae for power-law profiles, considering both the absence and presence of leaky rays. We find that leaky rays are

most likely not the cause of the discrepancies. The main part of this study concerns the misalignment loss in square-law fibers when the mode-power distribution is nonuniform as a result of mode-conversion effects. Special attention is given to the steady-state power distribution.[3] We find that the discrepancies mentioned earlier can be explained in terms of differences in the relevant mode-power distributions.

II. UNIFORM DISTRIBUTION

To compute the offset loss, Miller[1] compares the number of rays that exit and enter at coinciding points of the two fiber end faces of an offset fiber joint (see Fig. 1a). The percentage of rays not accepted on entrance is the offset loss. As a first case, we assume all rays to be uniformly excited. Both fibers have the same dimensions and are of the same kind. In the case of step-index fibers, all rays traversing the overlapping core areas continue to propagate and the only loss occurs outside these areas. Offset graded-index fibers show a loss also in the overlapping areas where the local numerical aperture (LNA) of the outgoing fiber is smaller than the corresponding LNA of the incoming

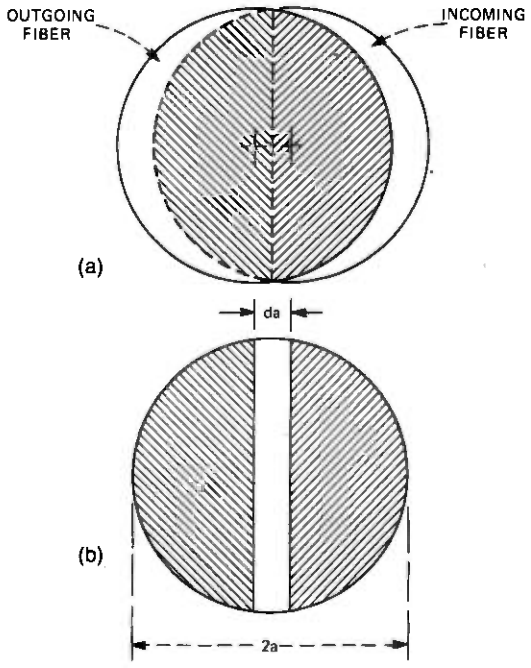

Fig. 1—Areas of transmission in a fiber splice. (a) End-on view of the splice. (b) Area of overlap rearranged for computation of offset loss.

fiber.* This condition exists for example in the right-hand half of the area of overlap in Fig. 1a. In this area, the outgoing fiber accepts only those rays that fall within its LNA; all others are lost. On the other hand—and this is important for our derivation—*all* rays in the outgoing fiber are uniformly excited in this area since we have assumed that all rays of the incoming fiber were excited.

In the left-hand half of the area of overlap, the incoming LNA is smaller than the outgoing LNA. Thus, all incoming rays are accepted there. On the other hand, the outgoing fiber is *not* fully excited. Since we assume that both fibers have the same characteristics, the number of incoming rays in the left half equals that of the accepted rays in the right half. If we arrange the two halves as in Fig. 1b, we find that the number of rays lost equals the number of those rays that traverse the blank area of Fig. 1b in a uniformly excited fiber. The width of this area is equal to the offset.

Assume a fiber core of diameter $2a$ and define a radial coordinate r that is so normalized that $r = 1$ at the core periphery. Let $n(r)$ be the core index and assume a constant index $n(1)$ in the cladding. In the case of full and uniform excitation of all trapped modes, the rays traversing a point in the core are uniformly distributed over all angular directions within a cone that has the LNA as its apex. The number of these rays is proportional to $(\text{LNA})^2 = n^2(r) - n^2(1)$. The integration of this quantity over the blank area of Fig. 1b, properly normalized, yields the offset loss. The integration can be performed analytically for step-index and parabolic profiles and leads to the results of Ref. 1.

If the offset is a small fraction d of the fiber radius, we can approximate the blank area by a rectangle of length $2a$ and width da. In addition, we can ignore the variation of the LNA across the width of that area. These assumptions simplify the integration so that the offset loss becomes simply

$$L_t = \frac{d}{\pi} \frac{\int_0^1 [n^2(r) - n^2(1)]dr}{\int_0^1 [n^2(r) - n^2(1)]rdr}. \tag{1}$$

If the index follows a power law

$$n^2(r) = n_0^2(1 - 2\Delta r^\alpha) \tag{2}$$

in the core, the evaluation yields

$$L_t = \frac{2d}{\pi} \frac{\alpha + 2}{\alpha + 1}. \tag{3}$$

* The LNA is proportional to the square root of the index difference at that point.

A comparison with the exact expressions for $\alpha = 1$, 2, and ∞ shows that (3) represents the first term of an expansion of L_t in powers of d. Remember that the result applies in the case of full and uniform excitation of all trapped rays, that is, those rays that are totally reflected inside the core.

Leaky rays possess an evanescent cladding field in a region extending from the core periphery to a circle of radius A in the cladding.[4] The smaller A, the larger the radiative (leakage) loss $l(A)$. Stewart[4] has found that the solid angle, which includes all rays having a loss smaller than $l(A)$, equals the solid angle comprising the trapped rays divided by $(A^2 - r^2)^{\frac{1}{2}}$. To obtain an upper bound to the influence of the leaky rays on the offset loss, we assume $A = a$ in the following although, by doing so, we include leaky rays that have a significant leakage loss.

Arguments analogous to the previous derivation lead to an offset loss

$$L_f = \frac{d}{\pi} \frac{\int_0^1 \frac{1 - r^\alpha}{(1 - r^2)^{\frac{1}{2}}} dr}{\int_0^1 \frac{1 - r^\alpha}{(1 - r^2)^{\frac{1}{2}}} r dr} \tag{4}$$

for a uniform power distribution in both trapped and leaky modes. We obtain

$$L_f = \frac{d}{2} \frac{1 - 1/K}{1 - K/(\alpha + 1)} \tag{5}$$

with

$$K = 2^{\alpha-2} \alpha \Gamma^2 \left(\frac{\alpha}{2}\right) \Big/ \Gamma(\alpha). \tag{6}$$

Table I lists loss values for some exponents α. Figure 2 shows loss versus offset for $\alpha = 2$. In that case, an offset of one tenth of the core radius causes a loss of 8.5 percent or 0.38 dB if only the trapped modes are considered and 7.5 percent or 0.34 dB if all leaky modes are taken into account as well. The discrepancy is small.

Equations (1) and (4) are based on the assumption that at least one of the fibers of the joint is fully excited at any given point in the splice cross section. This assumption requires some scrutiny in the

Table I — Offset loss coefficients

α	1	2	4	∞
L_t/d	0.95	0.85	0.76	0.64
L_l/d	0.85	0.75	0.67	0.5

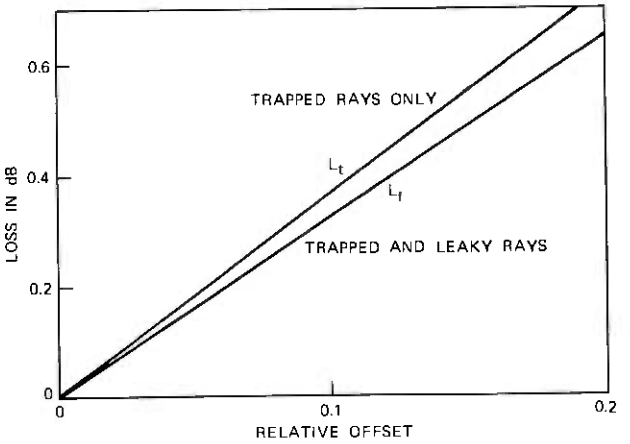

Fig. 2—Offset loss vs relative offset for uniform power distribution according to eqs. (3) and (5).

case of the leaky modes. In this case, the cone of rays traversing a given point in the core becomes elliptical, with the major axes oriented in radial and tangential direction. The offset juxtaposes cones with slightly different orientation. For (4) to hold, the larger of the cones must completely overlap the smaller cone. Without presenting details, we merely mention here that this condition is not satisfied, but that the resulting error is within the linear approximation in d.

III. NONUNIFORM DISTRIBUTIONS

Consider a ray that propagates in a fiber that has an index profile of the form (2). Assume that the ray forms an angle θ with the fiber axis at a distance ra from the axis. The principal ray optics variables r and θ have no physical meaning in the wave optics picture; the combination

$$R = \left(r^\alpha + \frac{\sin^2 \theta}{2\Delta} \right)^{\frac{1}{2}}, \tag{7}$$

however, is directly related to the propagation constant of a fiber mode.* Given the power in each fiber mode, we can plot the power distribution $p(R)$. Although the following computations can be performed for general power-law profiles, we restrict the derivation to the square-law profile in the interest of simplicity. The results for near square-law profiles are very similar. We introduce a normalized

* $R^2 = (1 - \beta^2/k^2 n_0^2)/2\Delta$, where β is the propagation constant and k the vacuum wave number. R is the magnitude of a vector coordinate in phase space pointing to the locus of the mode. We call R, therefore, the mode coordinate.

angular coordinate

$$\rho = \sin \theta/(2\Delta)^{\frac{1}{2}}, \tag{8}$$

so that, for square-law profiles,

$$R^2 = r^2 + \rho^2. \tag{9}$$

The fact that r and ρ are interchangeable in this relationship implies that offsets and tilts can be treated in the same way.* More specifically, in case of a tilt angle δ and a lateral offset d, we can introduce a single offset variable D so that

$$D^2 = d^2 + \sin^2 \delta/2\Delta. \tag{10}$$

Before we calculate the offset loss, let us compute the total transmitted power P for a given power distribution $p(R)$. We note from (9) that $\rho d\rho = RdR$ and that $p(R) = 0$ for $r > R$. Hence,

$$P = \int_0^1 p(R)2\pi RdR \int_0^R 2\pi\, rdr \tag{11}$$

or

$$P = 2\pi^2 \int_0^1 p(R)R^3dR. \tag{12}$$

If the power distribution depends on the angle ϕ, as indicated in Fig. 3, we obtain

$$P = 4\pi \int_0^1 R^3dR \int_0^\pi q(R, \phi) \sin^2 \phi d\phi \tag{13}$$

by introducing $rdr = ydx$ with $x = r \cos \phi$ and $y = r \sin \phi$ in (11).

Now consider a lateral offset d. Assume the power distribution in the incoming fiber to be $q(R_i)$ for $R_i < 1$ and zero everywhere else. If we retain only linear terms of d as before, $R_i = R - d \cos \phi$, where R is the mode coordinate of the outgoing fiber. The power distribution in terms of this coordinate becomes

$$p(R) = \frac{2}{\pi} \int_0^{\arccos[(R-1)/d]} q(R - d \cos \phi) \sin^2 \phi d\phi. \tag{14}$$

This expression is a modification of the second integral in (13), which takes into account that $q = 0$ for $\phi > \arccos [(R - 1)/d]$. A similar derivation holds for a tilt angle δ or a combination of offset and tilt. The result has the form (14) with d replaced by D of (10). It is convenient to normalize $q(R)$ for unit total power P; this is done in the following analyses.

---

*The modes of square-law fibers occupy a phase-space volume of rotational symmetry.

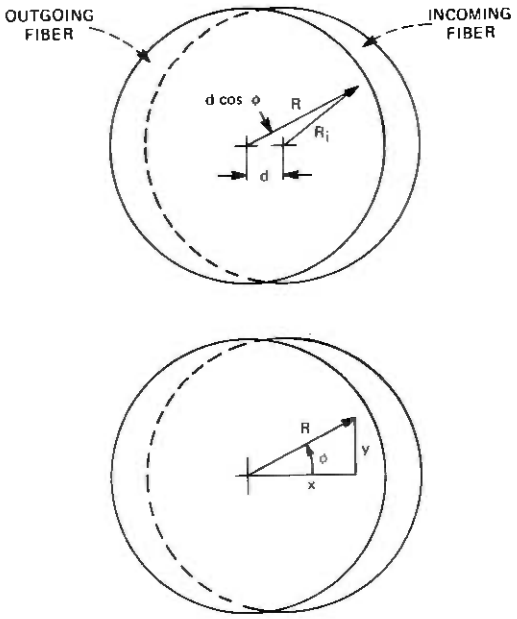

Fig. 3—Coordinate system used to compute offset loss.

As a first example, assume a uniform input distribution

$$q_1(R_i) = \begin{cases} 2/\pi^2 & \text{for} \quad R_i < 1 \\ 0 & \text{for} \quad R_i > 1. \end{cases} \tag{15}$$

Because of (14), the distribution in the splice becomes

$$p_1(R) = \frac{2}{\pi^3} \arccos \frac{R-1}{D} - \frac{2}{\pi^3} \frac{R-1}{D} \left[1 - \frac{(R-1)^2}{D^2}\right]^{\frac{1}{2}}. \tag{16}$$

Figure 4a shows q_1 and p_1 in the vicinity of $R = 1$ for $D = 0.1$. The offset loss is indicated by the cross-hatched area in Fig. 4a. It is

$$L_1 = 2\pi^2 \int_1^{1+D} p_1(R) R^3 dR = \frac{8D}{3\pi} \tag{17}$$

in accordance with (3), which yields $L_t = 8d/3\pi$ for $\alpha = 2$.

Power transfer among the modes as a result of guide imperfections modifies the step distribution (15). If we assume uniform excitation at the input and model the power exchange by a diffusion process, we find that the step function (15) assumes the form

$$1 - \exp[(R_i - 1)/0.17(z/z_c)^{\frac{1}{2}}] \tag{18}$$

a short distance z from the input. In this expression, z_c is the coupling

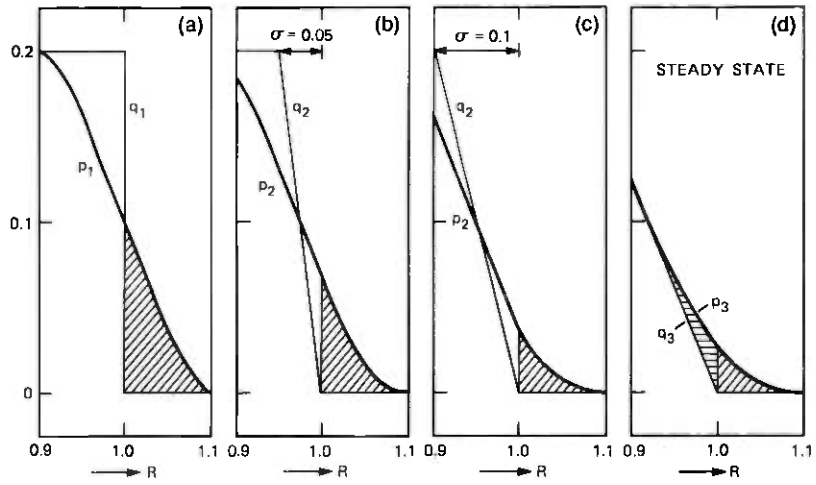

Fig. 4—Power distribution immediately ahead of the splice (q) and immediately behind the splice (p) for various power distributions plotted vs the mode coordinate R. The cross-hatched areas indicate splice loss; $D = 0.1$.

length.[3*] For our purposes, the approximation

$$q_2 = \frac{2(1+2\sigma)}{\pi^2}\begin{cases} 1 & \text{for} \quad R_i < 1-\sigma \\ (1-R_i)/\sigma & \text{for} \quad 1-\sigma < R_i < 1 \\ 0 & \text{for} \quad R_i > 1 \end{cases} \tag{19}$$

is satisfactory and valid as long as

$$\sigma = 0.17(z/z_a)^{\frac{1}{2}} \tag{20}$$

is small compared to unity. Figures 4b and c show plots of q_2 for $\sigma = 0.05$ and $\sigma = 0.1$ as well as the distribution $p_2(R)$ calculated from (14). An integration of the cross-hatched areas similar to (17) yields the loss L_2. Although an analytical solution exists, we list here only the simpler approximate form

$$L_2 = \frac{2D}{\pi}(1+2\sigma)\left(\frac{3}{4-1.3\sigma/D} + \frac{8}{\pi}\frac{\sigma}{D}\right)^{-1}, \tag{21}$$

which is more useful for design consideration. Figure 5 shows L_1 and L_2 for $\sigma = 0.05$ and $\sigma = 0.1$ plotted vs the offset D. If, for example, $z_a = 200$ m, a power distribution resembling that of Fig. 4b ($\sigma = 0.05$)

* The coupling length can be obtained by measuring the impulse response at a fiber length where the steady state has been reached. The coupling length is then equal to that length, multiplied by the square of the rms pulse width measured, and divided by the square of the rms width expected without mode conversion.

would exist 17.3 m from the input; similarly, a distribution resembling that of Fig. 4c would exist 34.6 m from the input (provided the input excitation is uniform). A 10-percent offset (or tilt) at these points would cause a loss of 0.14 dB or 0.09 dB respectively compared to 0.38 dB if the distribution were uniform at the splice. The reason for the drastic decrease in offset loss can be found in the fact that the modes close to cutoff suffer the main part of the offset loss, but cease to carry a significant portion of the total power a short distance away from the (uniformly excited) input.

For $\sigma > D$, the last term in (21) dominates. The loss can then be written in the form

$$L = \frac{\pi^2}{8} q'(1) D^2, \tag{22}$$

where $q'(1)$ is the derivative of q with respect to R at $R = 1$. In this case, the loss depends on the square of the offset and $L(D)$ has zero slope at $D \to 0$.

As z approaches z_s, the power distribution in the fiber resembles more and more the steady-state distribution.[3] Properly normalized, this distribution assumes the form

$$q_s = \frac{u^3}{2\pi^2(u^2 - 4)} \begin{cases} J_0(uR)/J_1(u) & \text{for} \quad R < 1, \\ 0 & \text{for} \quad R > 1, \end{cases} \tag{23}$$

where J_0 and J_1 are Bessel functions and $u = 2.405$ is the first root of

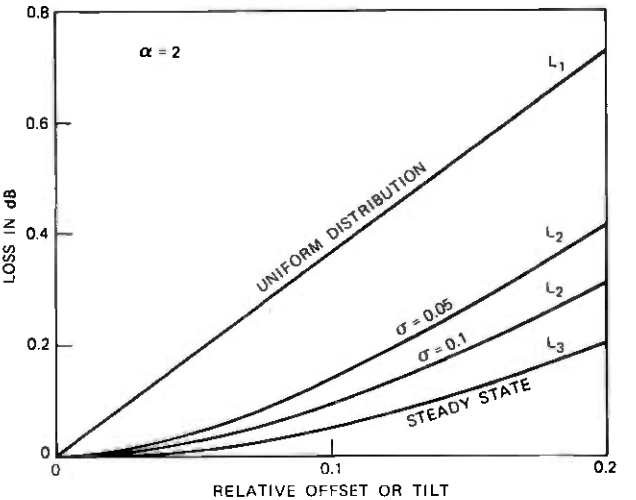

Fig. 5—Offset loss in dB vs relative offset or tilt for the four mode-power distributions sketched in Fig. 4.

J_0. Figure 4d shows q_3 as well as the distribution p_3 in the vicinity of $R = 1$. The fraction of p_3 that extends beyond $R = 1$ indicates the loss in the splice; it can be obtained from (22) by computing $q_3'(1)$ with the help of (23). The resulting loss L_3 is also plotted in Fig. 5. The part of the power distribution p_3 that deviates from the steady-state q_3 in the region $R < 1$ is accepted by the outgoing fiber, but is dissipated later as a result of mode conversion until the steady state is reestablished. An integration of $p_3 - q_3$ analogous to (17) but extending from $R = 1 - D$ to $R = 1$ reveals that this loss contribution is equal to the loss suffered in the splice. Thus, the total loss can be obtained by inserting $q_3'(1)$ into (22), as mentioned earlier, and by doubling the result of this integration; the total loss caused by an offset under steady-state conditions is, therefore,

$$L_s = \frac{u^4 D^2}{8(u^2 - 4)}. \tag{24}$$

This loss is plotted in Fig. 6. A 10-percent offset or a tilt angle equal to one tenth of the fiber NA causes 0.1 dB loss compared to 0.38 dB if the power is uniformly distributed in all trapped modes or 0.34 dB if leaky modes are present as well (Fig. 2).

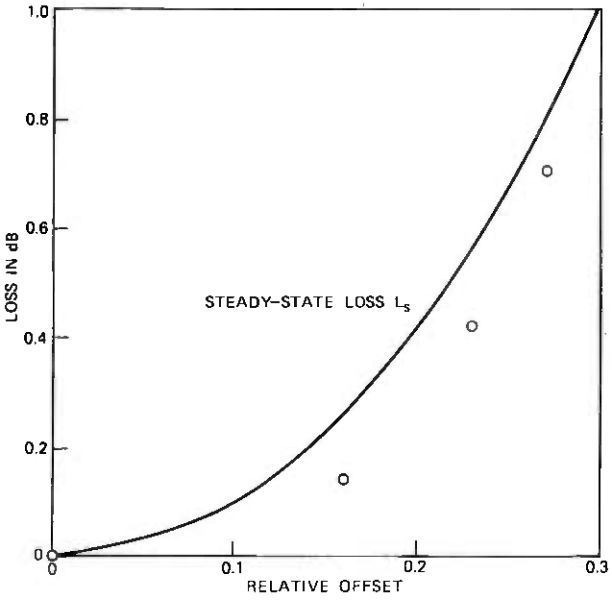

Fig. 6—Steady-state loss vs relative offset. Points show loss measured for offset between two ½-km fibers.

IV. COMPARISON WITH MEASUREMENTS

Figure 6 also shows loss values measured in a splice connecting two ½-km fibers. Details concerning the measurement are presented in Ref. 1. The coupling length characterizing these fibers was not measured, but was probably of the order of the fiber length. The fact that the loss values are consistently lower than the predicted steady-state loss may indicate that the ½-km length was not quite sufficient for the steady-state power distribution to establish itself before and after the splice.

Figure 7 shows loss values measured in a splice connecting two 3-m fiber pieces.[2] The fibers had an outside diameter of 125 μm, a core diameter of 75 μm, and an NA of 0.155. They were part of a cable structure that may have introduced some mode conversion. The fiber input was excited by a HeNe laser. Focused on the core, the gaussian laser beam filled a numerical aperture of 0.25 (at $1/e^2$ intensity). The solid line in Fig. 7 is a repetition of L_2 for $\sigma = 0.05$ plotted in Fig. 5. According to (20), this curve corresponds to the distribution present at a distance of 8.6 percent of the coupling length from the (uniformly excited) input.

It is beyond the purpose of this paper to determine under what circumstances a coherent source produces a uniform power distribution at the fiber input. The results depicted in Fig. 7 suggest that the use of a laser beam for splice loss measurements is acceptable as long as the

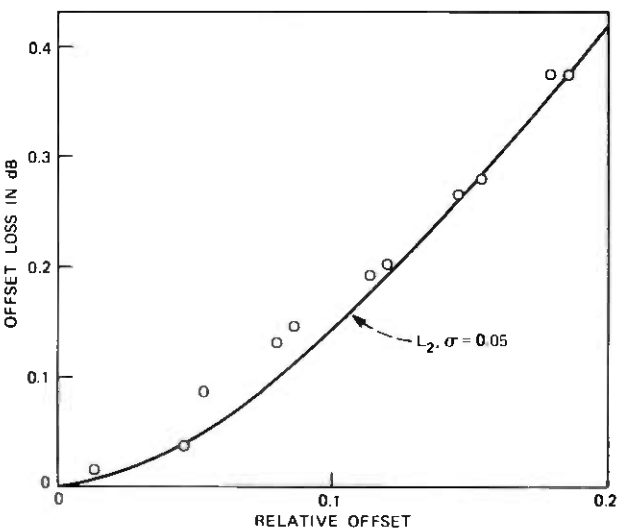

Fig. 7—Loss measured for offset between two 3-m fibers; solid line applies to conditions of Fig. 4b.

fiber NA is adequately filled by the beam and a modest amount of mode conversion is present (or applied) between input and splice. Measurements under the conditions described yield loss values that are about 50 percent too high at 10-percent offset and about equal to the steady state at 20-percent offset (or tilt).

V. CONCLUSIONS

We have attempted to show that the assumption of a uniform power distribution among all modes (or rays) is an idealization rarely obtained in fibers. The power distribution and particularly its behavior at the critical angle strongly affect the offset loss. If the offset loss calculation is based on the steady-state distribution, the loss at 10-percent relative offset (or tilt) is 3.8 times smaller than that predicted for a uniform distribution. Although the steady-state distribution does not necessarily exist at all splice points, we believe that it reflects transmission line conditions much better than a uniform distribution. We have compared these results with measurements by Miller[1] and Chinnock[2] and found that coherent excitation can provide offset loss values representative of line conditions if care is taken that the source fills the NA of the fiber and a modest amount of mode conversion is effective ahead of the splice point.

REFERENCES

1. C. M. Miller, "Transmission vs. Transverse Offset for Parabolic-Profile Fiber Splices With Unequal Core Diameters," B.S.T.J., this issue.
2. E. L. Chinnock and D. Gloge, "Simple Field Splicing Technique for Fiber Cable," unpublished work.
3. D. Marcuse, "Losses and Impulse Response of a Parabolic Index Fiber with Random Bends," B.S.T.J., *52*, No. 8 (October 1973), pp. 1423–1437.
4. W. J. Stewart, "Leaky Modes in Graded Fibers," Electron. Lett., *11*, No. 15 (July 24, 1975), pp. 321–322.

THE BELL SYSTEM TECHNICAL JOURNAL
Vol. 55, No. 7, September 1976
Printed in U.S.A.

Transmission vs Transverse Offset for Parabolic-Profile Fiber Splices With Unequal Core Diameters

By C. M. MILLER

(Manuscript received March 16, 1976)

A geometrical optics model is presented that is based on defining a local numerical aperture as a function of fiber radius with a uniform power distribution. Transmission vs transverse offset characteristics for parabolic-profile fiber splices are calculated for unequal fiber-core diameters. We show that the often-used assumptions of equal-mode excitation, equal-mode attenuation, and no-mode coupling are not adequate to calculate realistic transmission vs offset characteristics. Splice-loss measurements with long fiber lengths on each side of the splice show less than the calculated sensitivity to small offsets and greater than the calculated sensitivity to large offsets.

I. INTRODUCTION

Accurate transverse alignment is difficult to obtain in fiber optic splices primarily due to the small size of optical fibers. Many splicing techniques[1,2,3] use grooves or channels and are dependent on fiber outer diameter (OD) for transverse alignment. Experience thus far indicates that OD variations as small as ± 1 percent can be achieved on a single long fiber; however, fiber-to-fiber variations for fibers drawn at different times may be considerably greater. Small fluctuations in core-diameter-to-OD ratios are also expected. When the receiving fiber core is smaller than the transmitting fiber core, a loss occurs even with perfect transverse axial alignment.

Thiel[4] and Henderson[5] have reported transmission vs offset for equal-core-diameter, step-profile fiber splices and Pugh[6] has considered core-diameter ratios less than one (receiving fiber smaller than transmitting fiber) for step-profile fiber splices. Calculated values for transmission vs offset for equal-core-diameter, parabolic-profile fiber splices have been obtained earlier by the author.[7]

Transmission vs offset for parabolic-profile fiber splices with unequal core diameters is calculated in this paper. In addition, transmission vs offset-measurement data for equal-core-diameter, parabolic-profile fiber splices are presented. We found that the theoretical model gives pessimistic results for the equal-diameter case for the region of primary interest (offsets less than 0.8 core radius). Measured transmission is less than the model for offsets greater than 0.8 core radius.

II. ASSUMPTIONS

The solid angle defined by the local numerical aperture (NA) of the fiber at every point on the core is assumed to contain a uniform power distribution. This assumption is consistent with equal-mode excitation, equal-mode attenuation, and no-mode coupling.[8] Consider the profile

$$\eta(r) = \eta_0 \left[1 - 2\Delta \left(\frac{r}{R}\right)^\alpha\right]^{\frac{1}{2}} \quad \text{for} \quad r < R, \tag{1}$$

where

$\Delta = (\eta_0 - \eta_c)/\eta_0$ is small.
η_0 = refractive index at center of core.
η_c = refractive index of cladding.
α = a parameter between 1 and ∞.
R = fiber core radius.

The NA as a function of radius is then

$$\text{NA}(r) = [\eta(r)^2 - \eta_c^2]^{\frac{1}{2}}, \tag{2}$$

or

$$\text{NA}(r) \cong \eta_0\sqrt{2\Delta}\left[1 - \left(\frac{r}{R}\right)^\alpha\right]^{\frac{1}{2}}. \tag{3}$$

Since uniform power per unit solid angle is assumed transmitted for each incremental area of the core within the angle

$$\phi(r) = \sin^{-1}[\text{NA}(r)/\eta(r)], \tag{4}$$

the total power, P_T, equals

$$P_T \cong P(0)\int_0^{2\pi}\int_0^R \left[1 - \left(\frac{r}{R}\right)^\alpha\right] r dr d\theta, \tag{5}$$

or

$$P_T = \pi R^2 \alpha P(0)/(\alpha + 2), \tag{6}$$

where $P(0)$ is a constant dependent on the input power Δ and η_0.

When the fiber cores are offset, the total power received at a given point is assumed to be limited by the transmitting or receiving NA, whichever is the minimum at that point.

III. GENERAL APPROACH FOR THE PARABOLIC PROFILE ($\alpha = 2$)

For the case of equal fiber-core diameters, the locus of equal NA is a straight line, as shown in Fig. 1. The NA function is integrated over the area of overlap bounded by a circle and a straight line. The resulting integral for received power in region I, where the transmitting fiber has the minimum NA, is

$$P_R = 2P(0) \int_0^{\cos^{-1}(d/2R_T)} \int_{d/2\cos\theta}^{R_T} \left[1 - \left(\frac{r}{R_T}\right)^2\right] r dr d\theta. \qquad (7)$$

For region II, where the receiving fiber NA function has the minimum NA, a positive translation of the NA function must be made. The receiving NA function, translated an amount d and referenced to the center of the transmitting fiber, equals

$$\text{NA}(r) \cong n_0 \sqrt{2\Delta} \left[1 - \left(\frac{r^2 - 2dr\cos\theta + d^2}{R_R^2}\right)\right]. \qquad (8)$$

Four separate cases are considered to calculate transmission vs offset for unequal core diameters. If K is the ratio of the radius of the receiving fiber to the radius of the transmitting fiber, $K = R_R/R_T$, and d = offset, then the four cases are as follows:

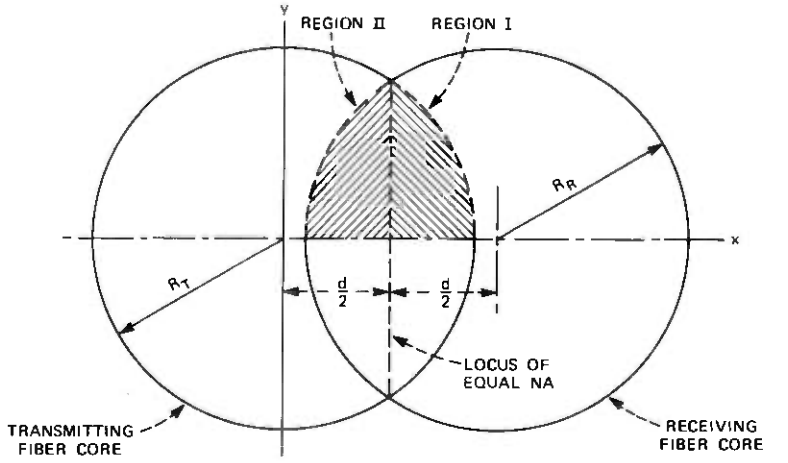

Fig. 1—Regions of overlap for offset fiber cores ($R_T = R_R$).

Case I

See Fig. 2. $d/R_T < K - 1$ for $K > 1$. Core boundaries do not intersect and $R_R > R_T$.

Case II

See Fig. 3. $d/R_T > K - 1$ for $K > 1$. Core boundaries intersect and $R_R > R_T$.

Case III

See Fig. 4. $d/R_T < 1 - K$ for $K < 1$. Core boundaries do not intersect and $R_T > R_R$.

Case IV

See Fig. 5. $d/R_T > 1 - K$ for $K < 1$. Core boundaries intersect and $R_T > R_R$.

For Cases I and III, areas of overlap are circles and the integrals are easily written and solved for the transmission. The resulting equations are shown on Figs. 2 and 4. For Cases II and IV, some areas of overlap are bounded by arcs of circles, and integrals for these areas are tedious to solve. The approach used for these cases is to divide

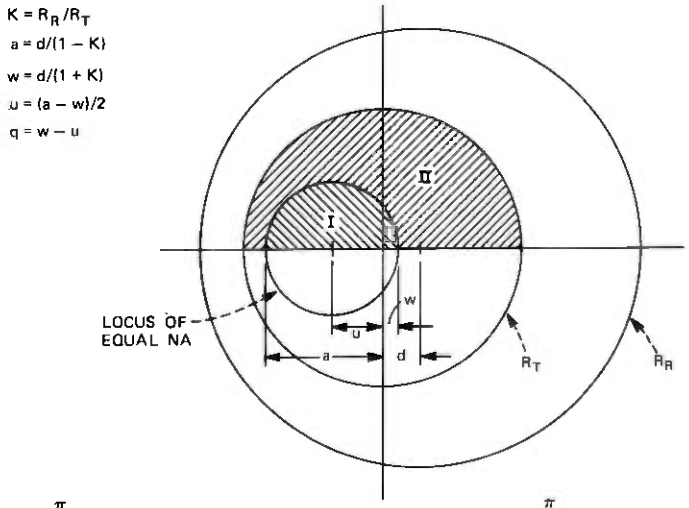

$$P_I = 2\int_0^{\frac{\pi}{2}}\int_0^{q}\left[1-\left(\frac{r}{R_R}\right)^2+\frac{2(d-u)r\cos\theta}{R_R^2}-\frac{(d-u)^2}{R_R^2}\right]r\,dr\,d\theta\,;\quad P_{II} = \frac{P_{TOT}}{2} - \int_0^{\frac{\pi}{2}}\int_0^{q} 2\left[1-\left(\frac{r}{R_T}\right)^2-\frac{2ur\cos\theta}{R_T^2}-\frac{u^2}{R_T^2}\right]r\,dr\,d\theta$$

$$T = \frac{2(P_I + P_{II})}{P_{TOT}} = 1 + \frac{4q^2}{R_T^2}\left[\left(1-\frac{1}{K^2}\right)\left(\frac{q^2}{2}+\frac{4qu}{3\pi}+\frac{u^2}{2}\right)+\frac{d}{K^2}\left(\frac{4q}{3\pi}+u-\frac{d}{2}\right)\right]$$

Fig. 2—$d < R_R - R_T$.

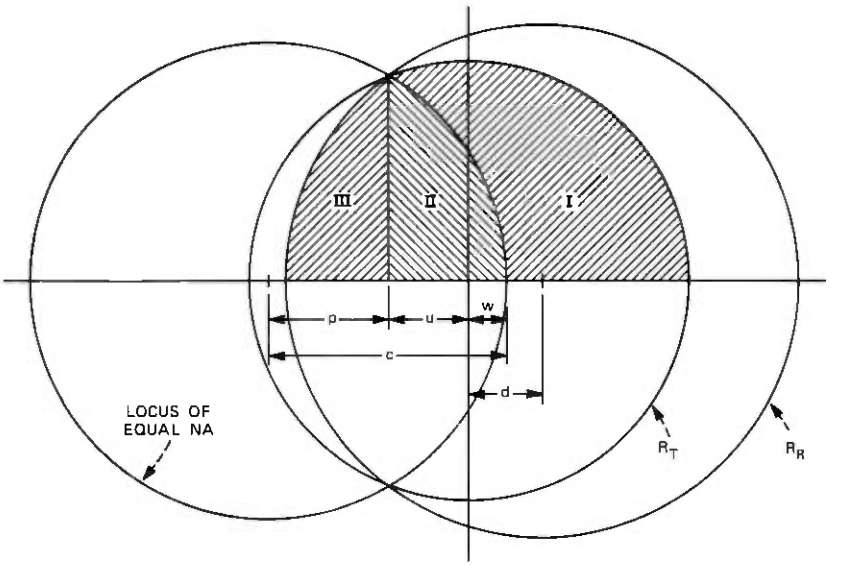

Fig. 3—$d > R_R - R_T$.

the areas of overlap into sections which are bounded by a circle and a straight line and to combine these sections to obtain the required geometry. All integrals then have the form suggested by eqs. (7) and (8) and can be segmented into the following three integral forms.

$$\int_0^{\cos^{-1}(a/b)} \int_{a/\cos\theta}^{b} r dr d\theta = \frac{b^2}{2}\cos^{-1}\frac{a}{b} - \frac{a}{2}\sqrt{b^2 - a^2}. \tag{9}$$

$$\int_0^{\cos^{-1}(a/b)} \int_{a/\cos\theta}^{b} r^2 \cos\theta\, dr d\theta = \tfrac{1}{3}\sqrt{(b^2 - a^2)^3}. \tag{10}$$

$$\int_0^{\cos^{-1}(a/b)} \int_{a/\cos\theta}^{b} r^3\, dr d\theta = \frac{b^4}{b}\cos^{-1}\frac{a}{b} - \frac{a}{12}\sqrt{(b^2 - a^2)^3} - \frac{a^3}{4}\sqrt{b^2 - a^2}. \tag{11}$$

These integrals were computer-programmed and summed to calculate transmission vs offset. Closed form expressions were not obtained due to the large number of terms involved. The combination of integrals for cases II and IV is given in the Appendix.

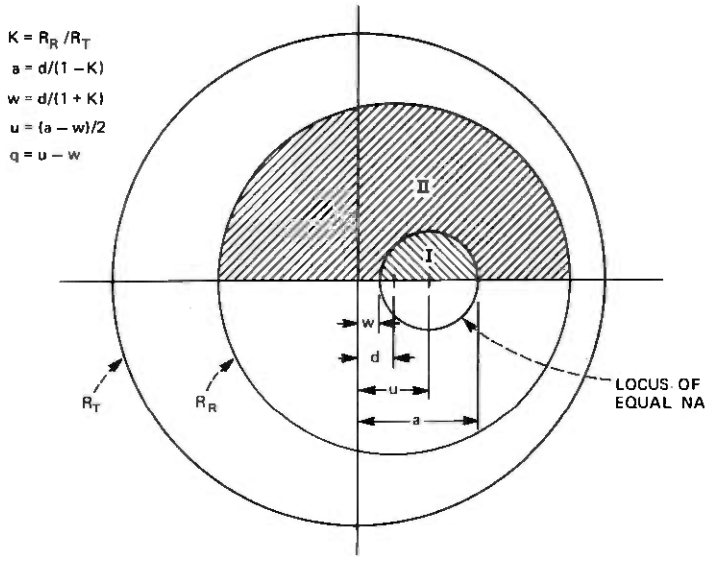

$$P_I = 2\int_0^{\frac{\pi}{2}}\int_0^{q}\left[1-\left(\frac{r}{R_T}\right)^2+\frac{2ur\cos\theta}{R_T^2}-\frac{u^2}{R_T^2}\right]r\,dr\,d\theta \;;\; P_{II} = 2\int_0^{\frac{\pi}{2}}\int_0^{q}\left[1-\left(\frac{r}{R_R}\right)^2\right]r\,dr\,d\theta - 2\int_0^{\frac{\pi}{2}}\int_0^{q}\left[1-\left(\frac{r}{R_R}\right)^2+\frac{2(u-d)r\cos\theta}{R_R^2}-\frac{(u-d)^2}{R_R^2}\right]r\,dr\,d\theta$$

$$T = K^2 + \frac{4q^2}{R_T^2}\left[\left(\frac{1}{K^2}-1\right)\left(\frac{q^2}{2}-\frac{4qu}{3\pi}+\frac{u^2}{2}\right)+\frac{d}{K^2}\left(\frac{4q}{3\pi}-u+\frac{d}{2}\right)\right]$$

Fig. 4—$d < R_T - R_R$.

IV. RESULTS OF CALCULATIONS

Figure 6 is the resulting plot of transmission (percent) vs offset (transmitting fiber-core radius) for $K = 1.05$, 1.00, and 0.95. Also shown are results calculated for the step profile for $K = 1.00$ and 0.95. These calculations show a 33-percent greater sensitivity to offset for the parabolic profile and approximately the same sensitivity to K as the step profile. Figure 7 is a family of curves for small offsets. For zero offset, the transmission equals 1 for $K > 1$ and equals K^2 for $K < 1$, as in the step profile. For offsets less than $R_T - R_R$ for $K < 1$, the parabolic profile exhibits a dependence on offset, whereas the step profile is constant. The reduction in transmission due to this effect is only 0.7 percent at 0.05 core-radius offset for $K = 0.95$. The slope discontinuities in the parabolic case in Fig. 7 result from the 0.01 core-radius offset increment selected. Curves for transmission vs offset are smooth except at the point $d = R_T - R_R$, where a discontinuity in the slope may exist.

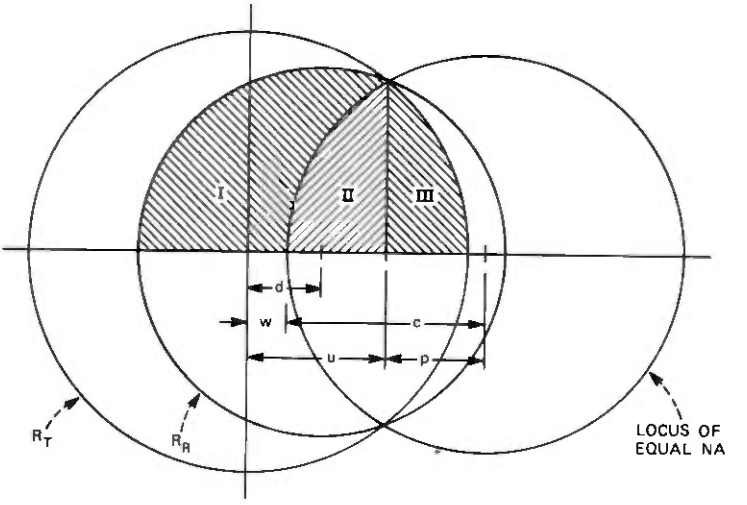

$k = R_R / R_T$

$u = (1/2d)\,(R_T^2 - R_R^2 + d^2)$

$w = d/(1 + K)$

$$c = \frac{-2uw + w^2 + R_T^2}{2(u - w)}$$

$p = c + w - u$

Fig. 5—$d > R_T - R_R$.

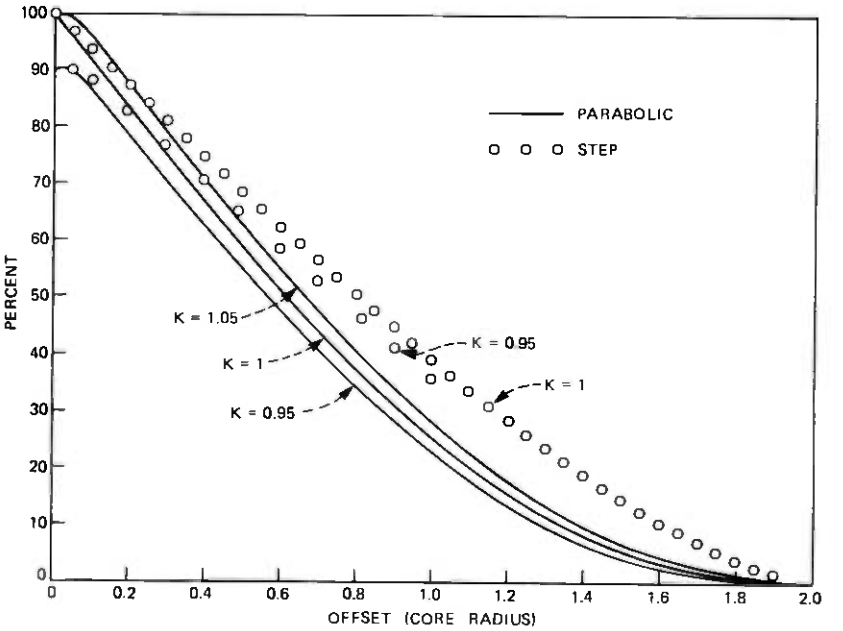

Fig. 6—Calculated transmission vs transverse offset.

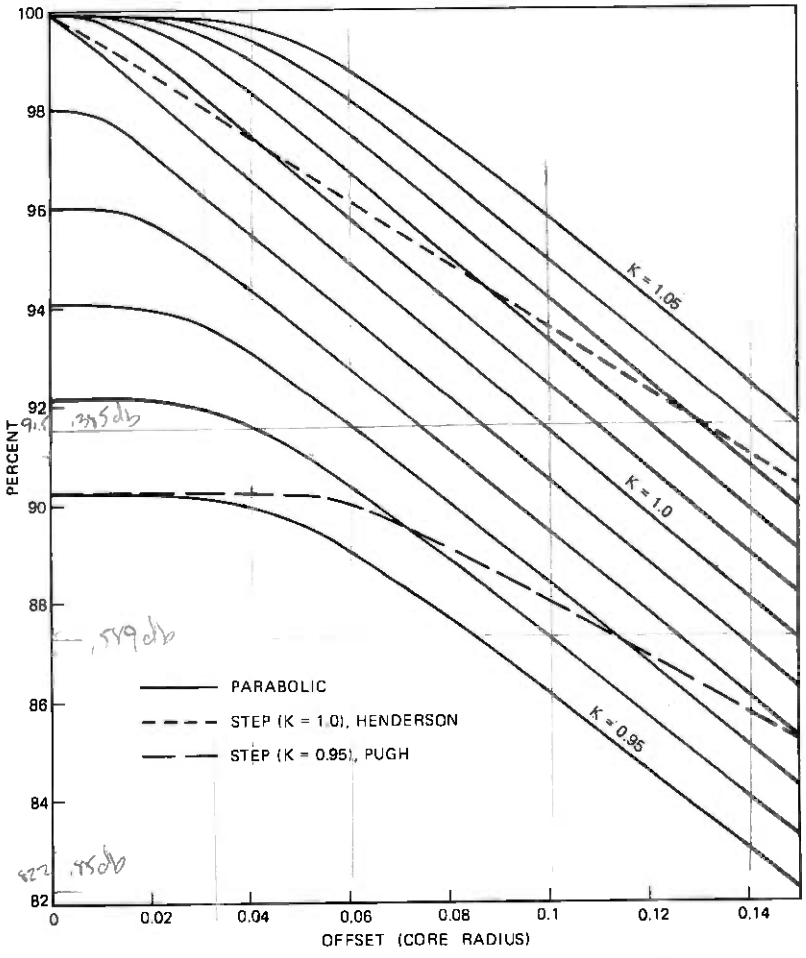

Fig. 7—Calculated transmission vs transverse offset for small offsets.

V. COMPARISON OF CALCULATIONS AND MEASUREMENTS

Several investigators have seen indications[9,10] that the sensitivity to small offsets is significantly less than the calculated values for parabolic fiber splices. These measurements[9,10] were made with short fibers on each side of the splice and the launched mode distribution probably differed greatly from the uniform power distribution assumed here.

A measurement of transmission vs offset was made with 500 meters of Corning fiber on each side of the splice subsequent to measuring the 100-percent transmission level. A helium-neon laser with an expanded beam and a 20X objective lens were used to completely fill the fiber NA. Two tabs were placed near the center of the 1-km parabolic CGW

fiber, about 4 inches apart, and the fiber was scored and broken between these tabs. A single break was made and the same ends were realigned on a microscope slide against a thin straightedge with the tabs used to obtain rotational alignment. Glycerin was used as the index-matching material and a cover slip held the ends in position under a microscope. The 100-percent level was again obtained and transverse offset was introduced in the splice and photographed.

Figure 8 shows the result of the transmission vs offset measurement. The sensitivity to offset for small offsets was less than predicted by theory, and greater than predicted for large offsets. The crossover point is approximately 0.8 core radius. For small offsets the reduction in sensitivity to offset is approximately the same as one would expect for a 10-percent oversized receiving fiber ($K = 1.1$).

The use of the geometrical optics approximation has been corroborated by comparison with the wave analysis of Marcuse.[12] The conclusion is that the assumption of equal-mode excitation, equal-mode attenuation, and no-mode coupling is not adequate to calculate splice transmission sensitivity to offset. The calculated transmission with core-diameter mismatch shows trends that can be used to obtain relative effects only. The long fiber length measurements of transmission vs offset can be used as design data for setting required alignment tolerances.

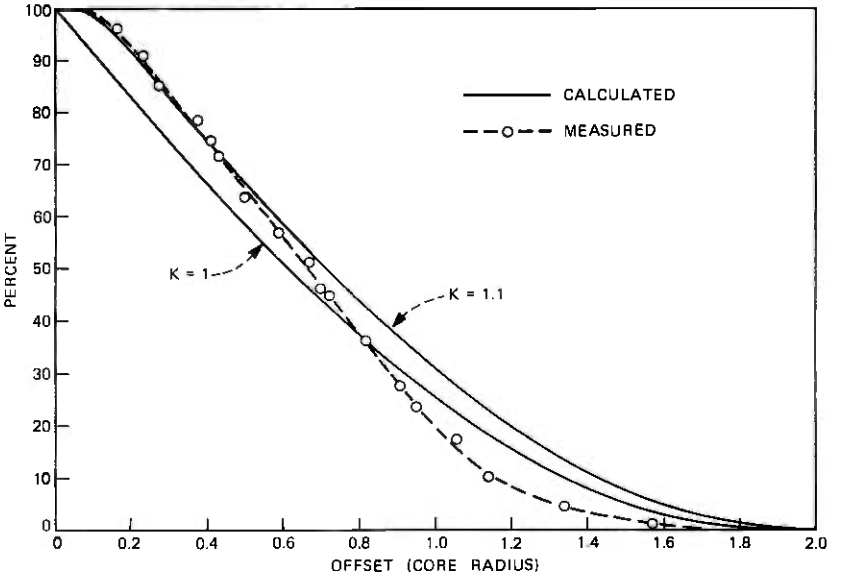

Fig. 8—Comparison of calculated and measured transmission vs transverse offset.

Current work by Gloge[13] indicates that the assumption of a sharp cutoff of power at the boundary of the solid angle defined by local NA could cause the discrepancies noted here. The model used in this paper is extended by Gloge to include a nonuniform power distribution across the solid angle defined by the local NA.

VI. ACKNOWLEDGMENT

The author is grateful to A. W. Miller for his help with the computer programs and plots.

APPENDIX

Integrals for Cases II and IV

A.1 Case II (Fig. 3) $d/R_T > 1 - K$ for $K > 1$.

$$P_{\mathrm{I}} = P_{\mathrm{tot}} - 2\int_0^{\cos^{-1}(-u/R_T)} \int_{-u/\cos\theta}^{R_T} \left[1 - \left(\frac{r}{R_T}\right)^2\right] r\,dr\,d\theta$$
$$- 2\int_0^{\cos^{-1}(p/c)} \int_{p/\cos\theta}^{c} \left[1 - \frac{r^2}{R_T^2} - \frac{2r(c-w)\cos\theta}{R_T^2} - \frac{(c-w)^2}{R_T^2}\right] r\,dr\,d\theta$$

$$P_{\mathrm{II}} = 2\int_0^{\cos^{-1}(p/c)} \int_{p/\cos\theta}^{c} \left[1 - \frac{r^2}{R_R^2} - \frac{2r(c+d-w)\cos\theta}{R_R^2} - \frac{(c+d-w)^2}{R_R^2}\right] r\,dr\,d\theta$$

$$P_{\mathrm{III}} = 2\int_0^{\cos^{-1}[(d-u)/R_R]} \int_{(d-u)/\cos\theta}^{R_R} \left[1 - \left(\frac{r}{R_R}\right)^2\right] r\,dr\,d\theta$$

$$T = \frac{P_{\mathrm{I}} + P_{\mathrm{II}} + P_{\mathrm{III}}}{P_T}.$$

A.2 Case IV (Fig. 5) $d/R_T > 1 - K$ for $K < 1$.

$$P_{\mathrm{I}} = 4\int_0^{\pi/2} \int_0^{R_R} \left[1 - \left(\frac{r}{R_R}\right)^2\right] r\,dr\,d\theta$$
$$-2\int_0^{\cos^{-1}[(u-d)/R_R]} \int_0^{R_R} \left[1 - \left(\frac{r}{R_R}\right)^2\right] r\,dr\,d\theta$$
$$-2\int_0^{\cos^{-1}(p/c)} \int_{p/\cos\theta}^{c} \left[1 - \left(\frac{r}{R_R}\right)^2 - \frac{2r(c+w-d)\cos\theta}{R_R^2} - \frac{(c+w-d)^2}{R_R^2}\right] r\,dr\,d\theta$$

$$P_{II} = 2\int_0^{\cos^{-1}(p/c)} \int_{p/\cos\theta}^{c} \left[1 - \left(\frac{r}{R_T}\right)^2 - \frac{2r(c+w)\cos\theta}{R_T^2} - \frac{(c+w)^2}{R_T^2}\right] r dr d\theta$$

$$P_{III} = 2\int_0^{\cos^{-1}(u/R_T)} \int_{u/\cos\theta}^{R_T} \left[1 - \left(\frac{r}{R_T}\right)^2\right] r dr d\theta$$

$$T = \frac{P_I + P_{II} + P_{III}}{P_T}.$$

REFERENCES

1. A. H. Cherin and P. J. Rich, "A Multi-Groove Embossed Plastic Splice Connector for Joining Groups of Optical Fibers," Applied Optics, *14* (December 1975), pp. 3026–3030.
2. C. M. Miller, "Loose Tube Splices for Optical Fibers," B.S.T.J., *54* (September 1975), pp. 1215–1226.
3. C. M. Miller, "A Fiber Optic Cable Connector," B.S.T.J., *54* (November 1975), pp. 1547–1556.
4. F. L. Thiel, "Utilizing Optical Fibers in Communications Systems," International Conference on Communications, Conference Record, Vol. II, Session 32, June 16–18, 1975.
5. D. M. Henderson, "A Fiber Quick-Connect Coupler," unpublished work.
6. W. E. Pugh, "Geometric Considerations for Array Splices in Fiber Optic Cables," unpublished work.
7. C. M. Miller, "Loss vs Tranverse Offset for Parabolic Fiber Splices," unpublished work.
8. D. Gloge and E. A. J. Marcatili, "Multimode Theory of Graded-Core Fibers," B.S.T.J., *52* (November 1973), pp. 1563–1578.
9. T. C. Chu, unpublished data on transmission vs offset for parabolic fibers, June 23, 1975.
10. C. M. Miller, unpublished data on transmission vs offset for an array splice using parabolic fibers, October 1, 1974.
11. J. S. Cook, P. Balaban, and T. C. Chu, "Axial Displacement Loss in Fiberguide Connectors," unpublished work.
12. D. Marcuse, "Excitation of Parabolic-Index Fibers with Incoherent Sources," B.S.T.J., *54* (November 1975), pp. 1507–1530.
13. D. Gloge, "Offset and Tilt Loss in Optical Fiber Joints," B.S.T.J., this issue.

THE BELL SYSTEM TECHNICAL JOURNAL
Vol. 55, No. 7, September 1976
Printed in U.S.A.

Laminated Fiber Ribbon for Optical Communication Cables

By C. M. MILLER

(Manuscript received February 26, 1976)

Laminated fiber ribbon (LAMFIR) exhibits mechanical properties of a composite structure and is strong enough to withstand the stresses of cable fabrication. Laminating parameters have been adjusted to make the LAMFIR relatively easy to separate for accessing the fibers. Optical properties of LAMFIR have been characterized, so that trade-offs between numerical apertures (NA), cladding thickness/core diameter (t/d), and additional loss are given for uncoated, step-profile fibers and one set of laminating conditions. Larger values of t/d than originally expected are desirable due to the bends in the fiber axes.

I. INTRODUCTION

The minimum loss obtainable in high-quality optical fibers has been steadily decreasing over the years with losses of less than 2 dB/km at 1.06 μm now being reported.[1] These advances along with those in the area of sources and detectors indicate that the basic components needed to build digital fiber links capable of operation in the tens or perhaps even hundreds of Mb/s range are becoming available. Combining a plurality of fragile optical fibers with adequate packaging to form a rugged communications cable is needed before fiber systems become practical.

The ribbon structure (linear array) for packaging optical fibers was suggested by Standley[2] and others of Bell Laboratories. This linear array structure is attractive from the splicing standpoint since groups of fibers can be handled at once. The "essentially two-dimensional" nature of fiber ribbons relaxes the alignment requirements needed to accomplish mass field splicing of optical cables. This is advantageous for multifiber splicing. In addition, the ribbon provides mechanical support and increased bulk, thereby greatly improving the "handling qualities" of individual fibers.

Other fundamental requirements of any ribbon structure are as follows:

(*i*) The ribbon structure must protect the fibers against breakage due to handling and must have an adequate service life. The mechanical strength and abrasion resistance must be sufficient to withstand forces generated in the cabling operation as well as the cable handling required to emplace these cables.

(*ii*) The optical properties of the fibers must not be significantly degraded by the ribbon structure or the subsequent cabling operation.

(*iii*) The ribbon structure must be strippable in order to expose the fibers for splicing or terminating to sources or detectors. Alignment accuracy of fibers within the ribbon and relative to the edge of the ribbon will probably be dictated by splicing requirements.

(*iv*) The ribbon structure must be economically manufacturable.

This paper reports on a laminated fiber ribbon (LAMFIR) which has strong bonding between the fibers and the ribbon structure. As shown in Fig. 1, a composite polyester-polyethylene tape forms each side of the structure with the fibers between them. At the polyester-polyethylene interface, the ribbon must be peelable in order to gain access to the fibers.

II. FABRICATION OF LAMFIR

A commercially available roll laminator, designed to plastic-encapsulate identification cards, was modified to fabricate LAMFIR. The additions to the original machine include (*i*) a fiber guide to provide uniform fiber separation, (*ii*) a cutter to trim away excess tape material, (*iii*) a more accurate temperature controller, and (*iv*) modified gearing to increase the laminating speed. As shown in Fig. 2, two supply reels feed the composite polyester-polyethylene material over heated rollers which soften the polyethylene. The two heated tapes are brought into contact under pressure and the fibers are sandwiched in polyethylene which serves as the adhesive. Forced-air cooling is applied after the pressure rollers. Power rollers pull the laminated

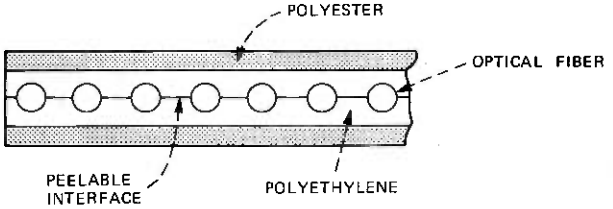

Fig. 1—Cross section of a laminated fiber ribbon.

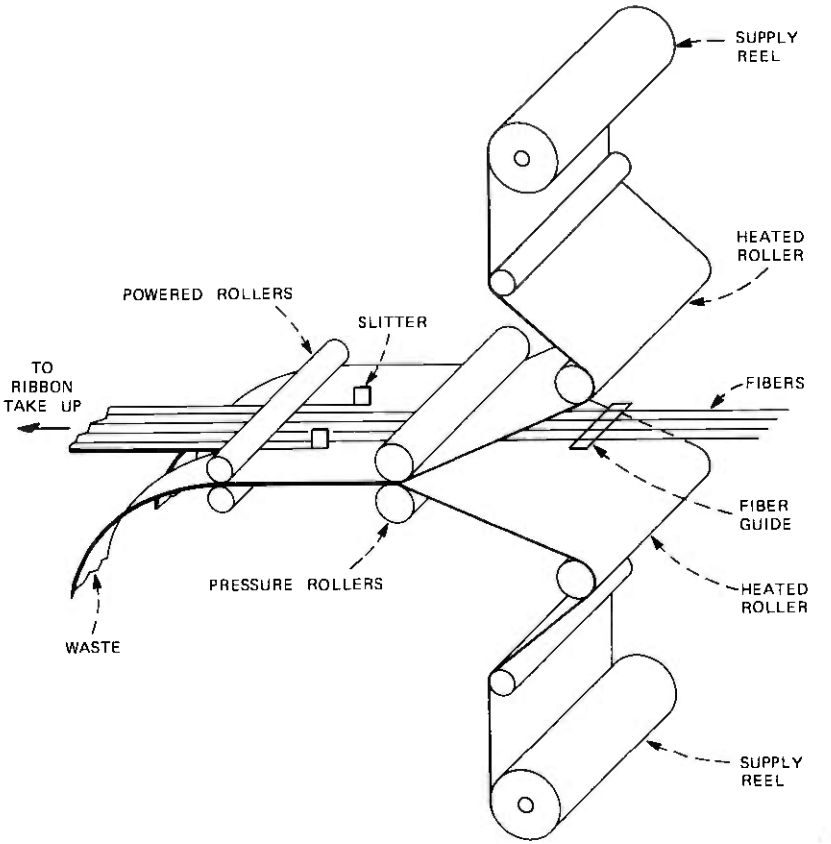

Fig. 2—Laminated fiber ribbon fabrication.

material through the slitting station, with tension provided by the supply reels.

The polyester maintains dimensional stability (higher melting temperature than polyethylene), while the polyethylene is softened by application of heat. At the proper temperature and pressure the polyethylene flows sufficiently around each fiber to form the cross section shown in Fig. 1.

III. MECHANICAL PROPERTIES

Mechanical strength tests have been performed on the LAMFIR structure.[3] The purpose of these tests was to determine how the structure modifies the mechanical properties of individual fibers. Tensile tests were made on two-foot samples with individual fiber breaks being detected *in situ* by an optical technique. The results

of these tests[3] on the LAMFIRs containing different numbers of fibers are shown in Fig. 3. The output of an optical sensor indicates that the first break in the straight portion of the curve corresponds to the load at which all the fibers have broken. It is seen that the load-bearing capacity of the fibers, as well as the slope, increases with the number of fibers. A comparison of the curves for the LAMFIR

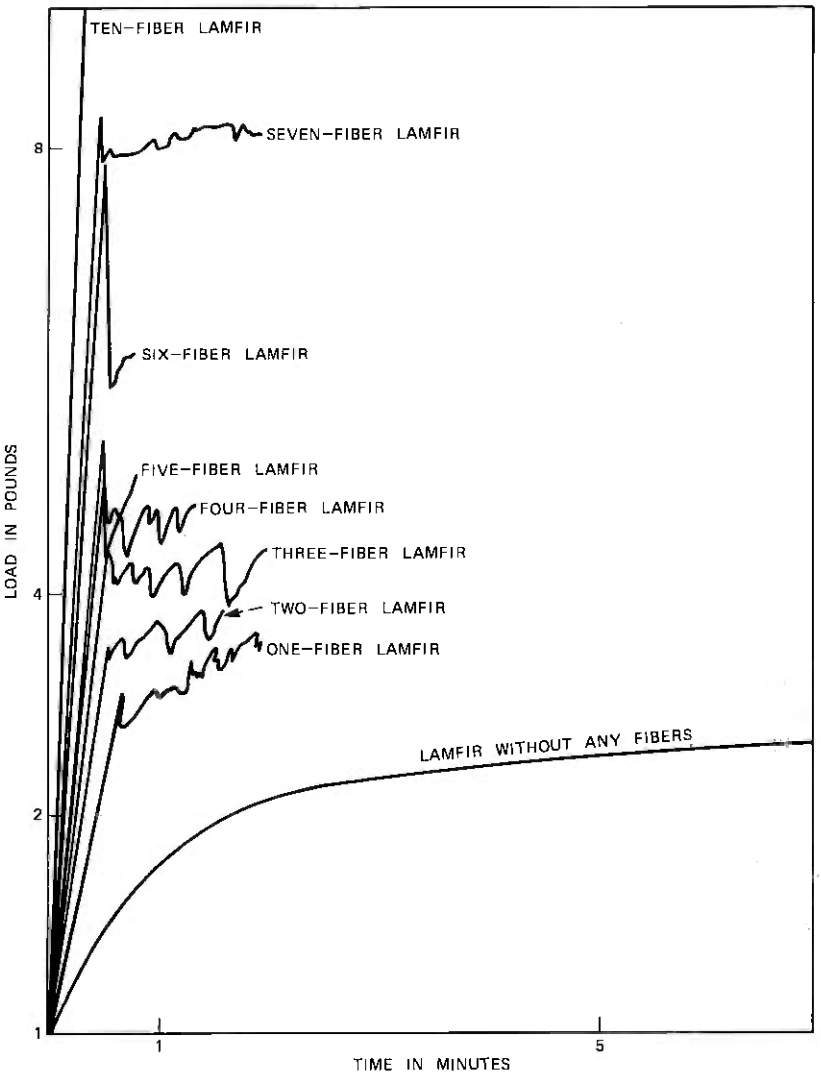

Fig. 3—Strength of a LAMFIR.

composites with the curve for LAMFIR containing no fibers shows that the fibers indeed carry the major portion of the load. After all of the fibers had fractured, the load did not decrease to the load-bearing capacity of the plastic alone. The fibers broke at different locations with respect to the tape, and the ribbon now behaves like a mechanical composite containing discontinuous fibers. Well-bonded discontinuous fiber composites react to applied loads by locally transferring stress through the matrix across the fiber discontinuities.[3]

From a mechanical standpoint the LAMFIR structure performs well. Rudimentary cables fabricated with LAMFIRs preserve the composite character of the ribbons. Tensile loads comparable to those anticipated in pulling long cables into ducts can be withstood without fiber breakage. Should additional strength be required, load-bearing fibers of graphite, Kevlar 49,* or glass could perhaps be guided into place during lamination to increase the strength of the ribbons. Load-bearing elements might also be embedded in the cable sheath[4] or elsewhere if additional strength is needed for pulling cables into rough or tight (high coefficient of friction) ducts.

IV. OPTICAL PROPERTIES

Initial LAMFIRs exhibited exceedingly high losses (hundreds of dB/km). It was found that random bending of the fiber axis caused this increased loss. The random bending was caused by shrinkage in the polyester component of the composite film after lamination during cooling of the polyethylene. A thicker polyester component which was oriented longitudinally to reduce shrinkage greatly reduced the additional loss.

The fiber cladding thickness is another factor that greatly affects the loss due to bending in the presence of a lossy jacket. The cladding optically isolates the fiber core by providing a low-loss medium for the exponentially decaying evanescent field. If the cladding is too thin, this evanescent field has appreciable intensity at the boundary between the cladding and, in the case of LAMFIR, the polyethylene which is lossy at optical frequencies. When bending of an optical fiber occurs, the transverse field extends even further into the cladding on the outside of the bend.[5]

Increased mode coupling due to random bending may also be contributing to the added loss.[6] This mechanism may result in a continuous transfer of energy to the lossier high-order propagating modes and to radiating modes. Either effect, inadequate cladding thickness or increased mode coupling, can significantly increase the loss of fibers.

---

* Trademark of E. I. duPont de Nemours and Company, Inc.

A set of 12 ribbons was fabricated with the emphasis on uniformity of ribbon geometry and repeatability of laminating conditions. All conditions during ribbon fabrication were held as constant as possible at a set laminating temperature and a constant laminating pressure supplied by pressure rollers. Additional loss vs cladding thickness/core diameter (t/d) for various fiber numerical apertures (NA) are shown in Fig. 4. All data points follow the dashed curves which indicate the trends in the data. Conclusions based on these particular laminating conditions (not necessarily optimum) are as follows:

(*i*) Additional loss decreases with increasing t/d and increasing NA as expected.

(*ii*) Three-mil OD fibers consistently exhibit higher additional losses than 5-mil OD fibers with the same t/d and NA. The amplitude and spatial frequency spectrum of the bends depend

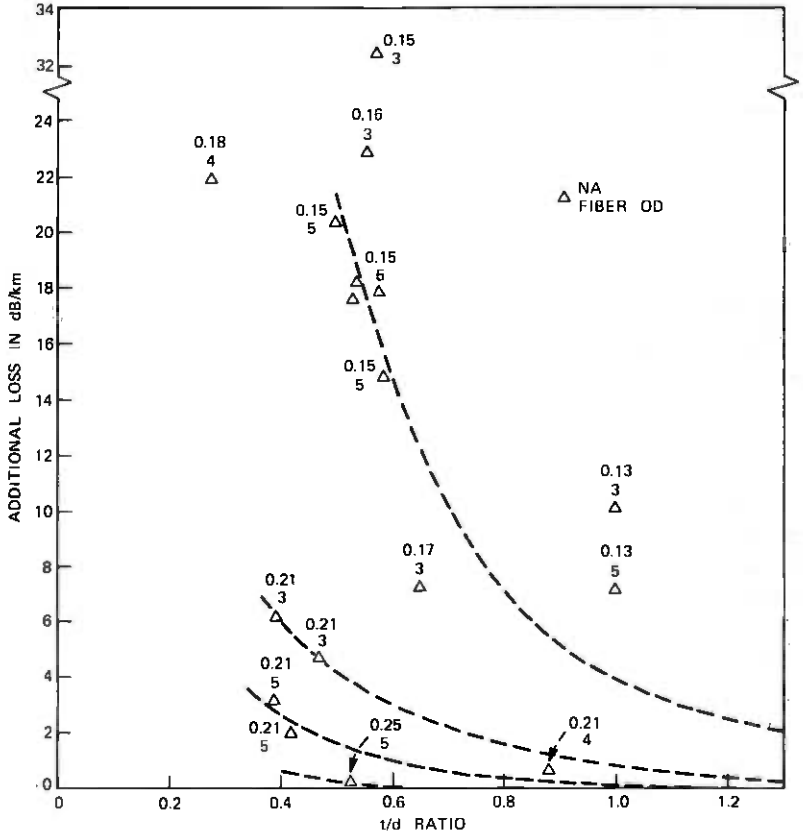

Fig. 4—Additional loss in a LAMFIR structure.

on the fiber stiffness. Five-mil fibers are much stiffer and probably assume bends with smaller amplitudes or longer periods (or both) as compared with 3-mil fibers.

(*iii*) A relatively high t/d value is needed for the LAMFIR structure. A t/d ratio approximately equal to 0.5 is required for 5-mil fibers at NA = 0.21 and probably t/d $\approx$ 1.3 for 5-mil fibers with NA = 0.15 for less than 2 dB/km added loss. The t/d parameter was selected because added loss increases with d and decreases with t. Since the powers of these two dependences may differ, loss may not be a single-valued function of t/d for a wide range of t and d. It is unclear which loss mechanism is responsible for the added loss, and indeed, inadequate cladding thickness may be important at small values of t/d while mode-coupling effects should dominate at large values of t/d.

(*iv*) Excellent repeatability of the data is indicated by the cluster of points with NA = 0.15 in the interval $0.5 < t/d < 0.6$. These fibers were all in different ribbons.

V. ACKNOWLEDGMENTS

The author appreciates the assistance of A. W. Miller in ribbon fabrication, the fruitful technical discussions with M. I. Schwartz, and the mechanical testing performed by B. K. Tariyal.

REFERENCES

1. W. G. French, J. B. MacChesney, P. B. O'Connor, and G. W. Tasker, "Optical Waveguides with Very Low Losses," B.S.T.J. Brief, *53*, No. 5 (May–June 1974), pp. 951–954.
2. R. D. Standley, "Fiber Ribbon Optical Transmission Lines," B.S.T.J. Brief, *53*, No. 6 (July–Aug. 1974), pp. 1183–1185.
3. B. K. Tariyal, private communication.
4. R. A. Kempf, private communication.
5. D. Marcuse, "Bent Optical Waveguide with Lossy Jacket," B.S.T.J., *53*, No. 6 (July–August 1974), pp. 1079–1101.
6. W. B. Gardner, "Microbending Loss in Optical Fibers," B.S.T.J., *54*, No. 2 (February 1975), pp. 457–465.

THE BELL SYSTEM TECHNICAL JOURNAL
Vol. 55, No. 7, September 1976
Printed in U.S.A.

Microbending Losses of Single-Mode, Step-Index and Multimode, Parabolic-Index Fibers

By D. MARCUSE

(Manuscript received January 16, 1976)

We present formulas for the microbending losses of fibers that are caused by random deflections of the fiber axis. We consider single-mode (or almost single-mode), step-index fibers and multimode, parabolic-index fibers and compare their losses. Loss formulas for the single-mode fiber are derived from coupled-mode theory using radiation modes. Simple empirical approximations of the general formulas are also presented. The losses of the parabolic-index, multimode fiber have been derived earlier. The losses of both fiber types are compared by assuming either that each fiber samples the spatial Fourier spectrum of the distortion function at the same spatial frequency, or by comparing typical fibers of each type with each other regardless of any similarity between them. It is found that the multimode, parabolic-index fiber has lower losses if it supports a sufficient number of guided modes.

I. INTRODUCTION

Two types of optical fibers appear to be promising for wideband communications, the monomode step-index fiber and a multimode fiber with parabolic (or nearly parabolic) refractive index distribution.[1] A third fiber type, the W-fiber,[2] is so similar to the step-index fiber that its properties are easily included in the discussion of single-mode fibers. However, single and multimode fibers suffer radiation losses caused by unintentional random bends of the fiber axis.[3,4] Thus, it is of interest to compare the two types of fibers and investigate which of them is better from the point of view of microbending losses. This loss comparison is the objective of this paper.

Radiation losses of optical fibers are caused by coupling between the guided modes and radiation modes.[5] Two modes with propagation constants β_1 and β_2 are coupled via a spatial frequency θ of the coupling function when[4]

$$|\beta_1 - \beta_2| = \theta. \tag{1}$$

A guided mode with propagation constant β_g couples directly to the radiation modes using the entire spatial frequency spectrum in the range

$$\beta_g - n_2k < \theta < \beta_g + n_2k \tag{2}$$

(n_2k is the plane-wave propagation constant of the cladding). However, most practical, randomly bent fibers have spatial Fourier spectra that drop off very rapidly with increasing spatial frequency so that only a narrow region of the spatial frequency spectrum near

$$\theta = \beta_g - n_2k = \Omega \tag{3}$$

is actually responsible for radiation losses in single-mode fibers.

In parabolic-index, multimode fibers, the random curvature of the fiber axis causes coupling among the guided modes. Adjacent guided modes in parabolic-index fibers have almost equal spacings in β space, so that only a very narrow band of spatial frequencies is instrumental in coupling the guided modes among each other.[6] Since most practical Fourier spectra drop off rapidly with increasing spatial frequency, we may assume that only the guided modes immediately adjacent (in β space) to radiation modes couple directly to radiation. Radiation losses in multimode fibers are thus less direct than in monomode fibers. The energy is exchanged among guided modes and is lost only when it reaches the guided modes of highest order. We treat this problem mathematically by assuming that the highest-order modes always carry zero power, because they lose their power directly to radiation.[6] In addition, we assume throughout this discussion that the modes are coupled so tightly that the steady-state power distribution has been established.[5] This assumption allows us to use a definite radiation loss of the multimode fiber. If steady state is not reached, the fiber loss cannot be characterized by a single number independently of the input conditions.

Our discussion has made it clear that essentially one single spatial frequency is responsible for radiation losses in fibers. In multimode, parabolic-index fibers, it is the spatial frequency that couples the guided modes among each other; in single-mode fibers, it is the spatial frequency Ω of (3). However, even though we can specify a definite spatial frequency for the single- as well as the multimode fiber, we still face the possibility that these frequencies may be different in either case. This raises the problem: what criteria are to be used by which a single-mode and a multimode fiber may be compared? In this paper, we shall use two different criteria. First, we asume that the spatial frequencies of interest are identical for both types of fibers. This requires us to assume that the core radius as well as the maximum

refractive index difference between core center and cladding is different for each fiber type. When compared on this basis, the parabolic-index, multimode fiber is superior in its loss performance to the single-mode fiber, provided that a sufficiently large number of guided modes can exist. This result is intuitively apparent, since we have seen that the power has to "dribble" down through all the guided modes before it reaches the region of radiation modes and becomes lost.

A second way of comparing single-mode and multimode fibers consists in considering configurations that are typical for each type of fiber regardless of the spatial coupling frequencies and determining quantitatively what their radiation losses are. It is clear that we must assume that the form of the spatial frequency spectrum is identical for each fiber type, otherwise no comparison would be possible. Compared on this basis the typical multimode, parabolic-index fiber has lower loss than the typical single-mode fiber.

A step-index fiber operates in a single guided mode if its characteristic V-number has values $V < 2.405$. However, some fibers are made with a relatively thin inner cladding that is surrounded by an outer cladding whose refractive index is similar to that of the fiber core. An example of such a structure is the W-fiber.[2] Such fibers do not support guided modes in the strict mathematical sense; each mode loses power by leakage through the thin inner cladding and may be regarded as a leaky mode. The loss of the lowest-order leaky mode may be kept so small that it is negligible for practical purposes. The loss of the mode of next higher order may be considerably larger, causing its power to be lost in a relatively short distance. Such a fiber behaves as a single-mode fiber for V values exceeding $V = 2.405$. The radiation losses caused by random bends can be calculated by computing the power-coupling coefficient of the lowest-order mode to the next higher mode and by assuming that the higher-order mode is so lossy that it does not carry any power. We include such quasi-single-mode fibers in our discussion. Since it is impossible to anticipate the actual shape of the power spectra of the coupling function, we use simple power laws as models. Because only limited spatial frequency ranges need to be compared in any case, it should always be possible to approximate an actual power spectrum by a suitable power law.

II. LOSS FORMULA FOR THE SINGLE-MODE FIBER

Random bends of an optical fiber can be described by assuming that the core-cladding boundary is changing as a function of the length coordinate z. Thus, we describe the core boundary of a fiber with random bends by the equation[5]

$$r(\phi, z) = a + f(z) \cos \phi. \tag{4}$$

In this equation, a is the core radius and $f(z)$ describes the shape of the randomly deformed fiber axis; ϕ is the angular coordinate of a cylindrical coordinate system.

Using the standard coupled-mode formalism,[5] we derive the following formula for the radiation loss coefficient of any LP mode (for definition of LP, see Ref. 7) of the step-index fiber with randomly deformed axis,

$$2\alpha_\nu = \frac{(n_1^2 - n_2^2)\gamma^2 J_\nu^2(\kappa a)}{2(n_2 \pi a)^2 |J_{\nu-1}(\kappa a) J_{\nu+1}(\kappa a)|} \cdot \int_{-n_2 k}^{n_2 k} |\beta| (F^2(\beta_\nu - \beta)) \left\{ \frac{J_{\nu-1}^2(\sigma a)}{|\sigma J_\nu(\sigma a) H_{\nu-1}^{(1)}(\rho a) - \rho J_{\nu-1}(\sigma a) H_\nu^{(1)}(\rho a)|^2} + \frac{J_{\nu+1}^2(\sigma a)}{|\sigma J_\nu(\sigma a) H_{\nu+1}^{(1)}(\rho a) - \rho J_{\nu+1}(\sigma a) H_\nu^{(1)}(\rho a)|^2} \right\} d\beta. \quad (5)$$

The Fourier spectrum of the distortion function $f(z)$ appearing in (4) is defined as

$$F(\theta) = \lim_{L \to \infty} \frac{1}{\sqrt{L}} \int_0^L f(z) e^{-i\theta z} dz. \quad (6)$$

The ensemble average of the square of $F(\theta)$ can be expressed as the Fourier transform of the correlation function $R(u)$ of $f(z)$,[8]

$$\langle F^2(\theta) \rangle = \int_{-\infty}^{\infty} R(u) e^{-i\theta u} du. \quad (7)$$

The other symbols appearing in (5) are defined as follows:

2α = power attenuation coefficient
a = core radius
n_1 = refractive index of fiber core
n_2 = refractive index of cladding
ν = azimuthal mode number of LP mode ($\nu = 0$ for HE_{11} mode)
β_ν = propagation constant of guided LP mode
$k = \omega(\epsilon_0 \mu_0)^{\frac{1}{2}} = 2\pi/\lambda$ free-space propagation constant
$V = (n_1^2 - n_2^2)^{\frac{1}{2}} ka$
$\kappa = (n_1^2 k^2 - \beta_\nu^2)^{\frac{1}{2}}$
$\gamma a = [V^2 - (\kappa a)^2]^{\frac{1}{2}}$
$\sigma = (n_1^2 k^2 - \beta^2)^{\frac{1}{2}}$
$\rho = (n_2^2 k^2 - \beta^2)^{\frac{1}{2}}$
$J_\nu(x)$ = Bessel function
$H_\nu^{(1)}(x)$ = Hankel function of the first kind.

Equation (5) was derived by using the approximate radiation modes of the fiber. This formula is, thus, accurate only if the radiation escapes at small angles relative to the fiber axis.[5] This condition is satisfied for power spectra that drop off rapidly with increasing spatial frequency, an assumption that is made throughout this paper.

It was mentioned in the introduction that certain step-index fibers have claddings that are sufficiently narrow to provide high-leakage losses to all but the lowest-order mode. We obtain the microbending radiation loss for such fibers by assuming that two modes can exist in the fiber, but that only the lowest-order mode carries power. This mode is coupled to the next-higher-order leaky mode as well as to the radiation modes. However, since we assume that the amplitude of the spatial power spectrum of the coupling function decreases rapidly with increasing spatial frequencies, it is sufficient to consider only coupling to the leaky guided mode and ignore the radiation mode spectrum. The power-coupling coefficient between guided modes 0 and 1 is designated as h_{01}. The power loss coefficient for the HE_{11}-mode in the presence of a second but leaky mode may thus be expressed as*

$$2\alpha = h_{01} = \frac{\gamma_0^2\gamma_1^2 J_0^2(\kappa_0 a) J_1^2(\kappa_1 a)\left[k^3\langle F^2(\bar{\Omega})\rangle\right]}{2a^2 n_2^2 k^5 J_1^2(\kappa_0 a)\,|J_0(\kappa_1 a) J_2(\kappa_1 a)|}. \tag{8}$$

The subscript 0 refers to the HE_{11} mode while the subscript 1 indicates the next higher LP mode.[7] The spatial frequency $\bar{\Omega}$ is defined as

$$\bar{\Omega} = \beta_0 - \beta_1 \approx \frac{\kappa_1^2 - \kappa_0^2}{2n_2 k}. \tag{9}$$

Equation (8) is applicable in the range

$$2.405 < V < 3.832. \tag{10}$$

A discussion of the validity of using radiation modes to calculate the microbending losses is given in the Appendix.

III. APPROXIMATE LOSS FORMULAS

It is possible to approximate formulas (5) and (8) by expressions that show the relative influence of the fiber parameters and are simple enough to allow evaluation by pocket calculators.

In the remainder of this paper, we restrict ourselves to power spectra of the form

$$\langle F^2(\theta)\rangle = \frac{m\bar{\sigma}^2 \sin\frac{\pi}{m}}{\Delta\theta\left[1 + \left(\frac{\theta}{\Delta\theta}\right)^m\right]}. \tag{11}$$

* See eqs. (3.6–10) and (5.2–20) in Ref. 5.

This simple power law may serve as a model for every practical power spectrum, because we are usually interested only in a narrow spatial frequency region of the spectrum, which can always be approximated by a function of the form (11). The variance $\bar{\sigma}^2$ is defined by (28); m is the exponent of the power law, and $\Delta\theta$ is the width parameter of the distribution (11).

For large values of the spatial frequency, we can express (11) in the simpler form,

$$\langle F^2(\theta)\rangle = \frac{A_m}{\theta^m}, \tag{12}$$

with

$$A_m = m(\Delta\theta)^{m-1}\bar{\sigma}^2 \sin\frac{\pi}{m}. \tag{13}$$

If we use (12) and the transformation

$$\theta = \Omega x, \tag{14}$$

we can express (5) for $\nu = 0$ (HE_{11}-mode) in the form

$$2\alpha_0 = \frac{(n_1^2 - n_2^2)k\gamma^2\Omega J_0^2(\kappa a)}{\pi^2 n_2 a^2 J_1^2(\kappa a)}\langle F^2(\Omega)\rangle \cdot \int_1^\infty \frac{1}{x^m}\frac{J_1^2(\sigma a)}{|\sigma J_0(\sigma a)H_1^{(1)}(\rho a) - \rho J_1(\sigma a)H_0^{(1)}(\rho a)|^2}dx. \tag{15}$$

This expression is not much simpler than (5), but it shows clearly that the radiation loss depends indeed only on the spatial frequency $\theta = \Omega$ defined by (3). The upper limit ∞ on the integral in (15) is an approximation that is valid for sufficiently large values of m. Equation (15) is useful only in the narrow interval

$$1 < V < 2.405. \tag{16}$$

For smaller V values, the HE_{11} mode is so loosely guided that its field reaches very far into the cladding and suffers excessive bending losses. For $3.832 > V > 2.405$, the step-index fiber is no longer supporting only one mode and (8) must be used. We have plotted (15) for a number of m values in the range (16) and used this plot to obtain the following empirical approximation of (15):

$$2\alpha_0 = \frac{n_2 k^4\langle F^2(\Omega)\rangle}{(m-1)(m-2)}\left(\frac{\Omega}{k}\right)^3\left(V + 7.58\times 10^{-5}\frac{m^9 V^m}{e^{1.7m}}\right). \tag{17}$$

This formula holds only for $m \geqq 4$. The accuracy of (17) will be discussed in connection with a discussion of Fig. 3.

A good approximation [less than 0.5 percent error in the range (16)] of the solution of the eigenvalue equation of the HE_{11} mode can be

expressed empirically as follows:

$$\kappa_0 a = 2.405 \exp\left(-\frac{0.8985}{V}\right), \tag{18}$$

and (3) can be approximated by

$$\frac{\Omega}{k} = (n_1 - n_2)\left[1 - \left(\frac{\kappa a}{V}\right)^2\right]. \tag{19}$$

Equations (18) and (19) enable us to calculate loss values from (17) without having to solve the eigenvalue equation for the HE_{11} mode.

A similar empirical procedure allows us to approximate (8) as follows:

$$2\alpha_0 = \frac{\langle F^2(\bar{\Omega})\rangle}{2n_2^2 a^6 k^2}\left[9(V - 1.87) - \frac{0.616}{(V - 2.405)^{\frac{1}{2}}}\right]. \tag{20}$$

The spatial frequency $\bar{\Omega}$ is defined by (9) with $\kappa_1 a$ approximated by

$$\kappa_1 a = 3.832 \exp\left(-\frac{0.8492}{V - 0.55}\right). \tag{21}$$

In the range (10), this formula deviates from the exact solution of the eigenvalue equation by less than 0.5 percent (only very close to the endpoint at $V = 2.41$ is the error 0.8 percent).

IV. MULTIMODE LOSSES

The radiation loss formula for multimode parabolic-index fibers, whose mode distribution has reached steady state, has been derived earlier,[6]

$$2\alpha_p = 5.8\,\frac{\langle F^2(\theta_p)\rangle}{a^4}\,\Delta. \tag{22}$$

The refractive-index distribution inside the fiber core is given by the expression

$$n(r) = n_1\left[1 - \left(\frac{r}{a}\right)^2\Delta\right]. \tag{23}$$

The spatial frequency instrumental for mode coupling is[6]

$$\theta_p = \frac{(2\Delta)^{\frac{1}{2}}}{a}. \tag{24}$$

The total number of guided modes of both polarizations and orientations supported by the fiber is[9]

$$N = (n_1 ka)^2\,\frac{\Delta}{2}. \tag{25}$$

Since the core radius a appearing in (22) is different for single-mode,

step-index fibers and multimode, parabolic-index fibers, we must express it in terms of some other quantity. We have mentioned in the introduction that the spatial frequency Ω of eq. (3) characterizes coupling of the step-index fiber mode to radiation. One way of comparing single- and multimode fibers is to insist that the critical coupling (spatial) frequency is the same for both fiber types. By eliminating a and Δ, we obtain from (22), (24), and (25),

$$2\alpha_p = 1.45 \frac{n_1}{\sqrt{N}} \left(\frac{\theta_p}{k}\right)^8 k^4 \langle F^2(\theta_p)\rangle. \tag{26}$$

The number of modes carried by the fiber can be varied by varying the core radius a, the relative refractive index Δ, or the free-space propagation constant k. Keeping θ_p and k constant requires us to vary a and Δ as N is varied.

V. COMPARISON OF SINGLE-MODE AND MULTIMODE FIBER LOSSES

We represent the radiation loss coefficients in normalized form by dividing 2α by the product $k^4\langle F^2\rangle$. According to its definition (6) or (7), the power spectrum has the dimension cm^3. Since k has the same dimension as 2α, the ratio is dimensionless. The spatial frequency θ and the shape of $\langle F^2(\theta)\rangle$ are always chosen to be the same for the single-mode or multimode fibers that are to be compared. In Figs. 1 and 2, we have plotted the normalized loss coefficient of the single-mode

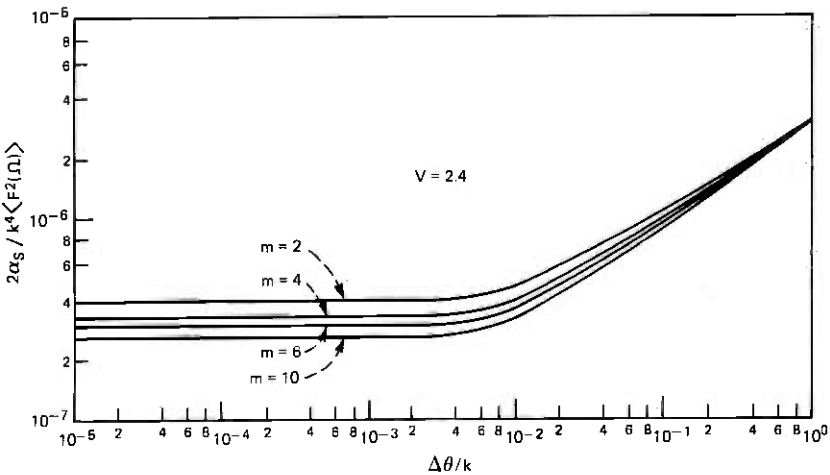

Fig. 1—Normalized loss coefficient of the single-mode, step-index fiber with power spectrum defined by (11) as a function of the width parameter $\Delta\theta/k$ of the power spectrum. The curve parameter m indicates the exponent of the power law. $n_1 = 1.515$, $n_2 = 1.5$, $V = 2.4$.

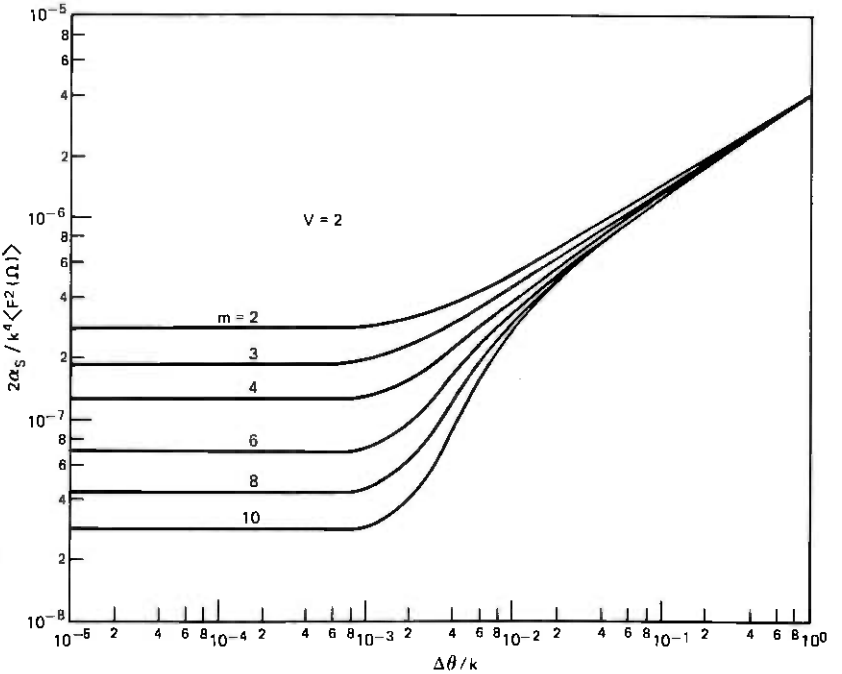

Fig. 2—Similar to Fig. 1 with $V = 2$.

fiber as a function of the normalized width parameter $\Delta\theta/k$ of the power spectrum (11) for $n_2 = 1.5$ and $n_1 = 1.01\ n_2$. The loss curves were computed from (5) and the frequency Ω appearing in the argument of the power spectrum is defined by (3). Figures 1 and 2 show that the loss coefficient is independent of the width parameter for small values of $\Delta\theta/k$. The dependence of the normalized loss on the normalized frequency V is illustrated in Fig. 3 for the case that the power spectrum (11) can be approximated in the form (12). The solid curves are computed from (5) while the dotted curves are calculated from the approximate formulas (17) through (19). It is apparent that the approximation is quite good, particularly for large values of the exponent m. The dash-dotted curves in Fig. 3 illustrate how the approximation deteriorates if the term in (17) containing V^m is omitted. It is apparent that this term provides an important correction for large values of V. The range of V values on the abscissa of Fig. 3 coincides with the single-mode range of (16). Formulas (5) or (17) do not hold for larger V values. For $2.405 < V < 3.83$, eq. (8) or its approximation (20) apply. The agreement of the approximation (20) with (8) is at least as good as that of the solid and dotted curves with $m = 10$ in Fig. 3; therefore, only a

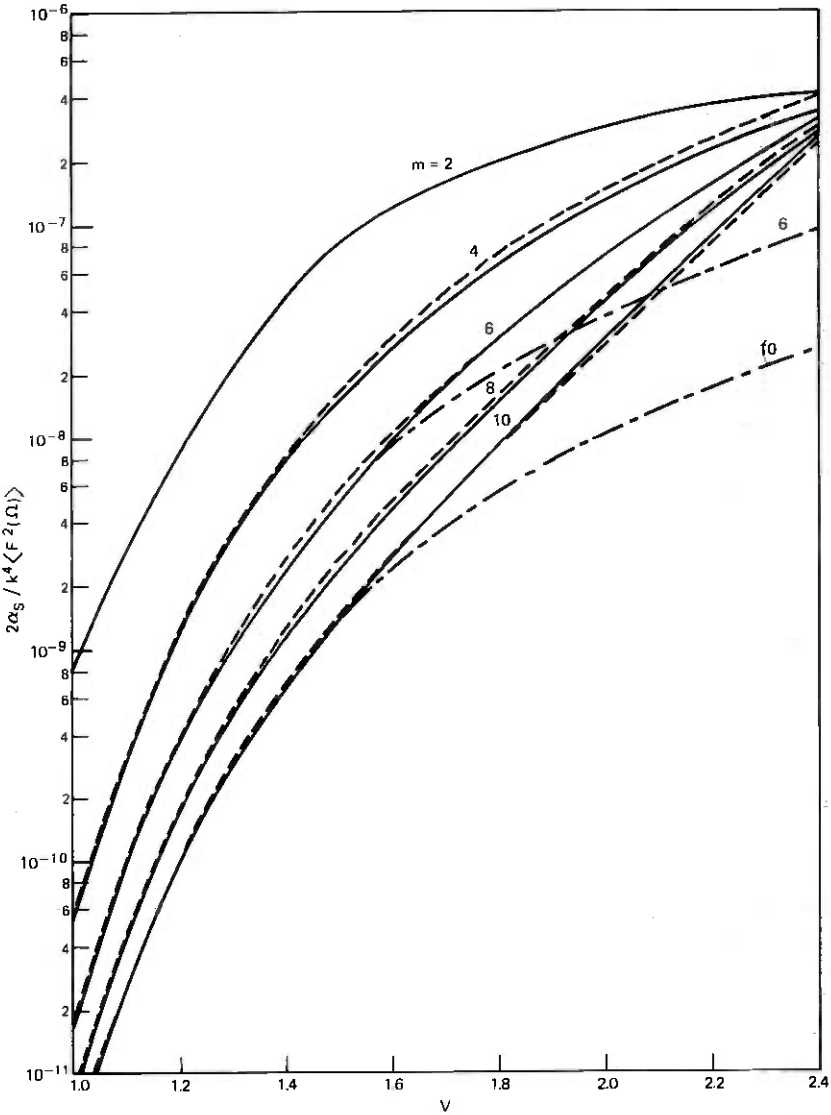

Fig. 3—Normalized loss coefficient of the single-mode, step-index fiber as a function of the normalized frequency parameter V for several values of the power law exponent m. The loss values in this curve correspond to the flat portions on the left-hand side of Figs. 1 and 2. The solid curves correspond to eq. (5) while the dotted curves were computed from the approximate equation (17). The dash-dotted curves represent (17) without the term V^m. $n_1 = 1.515$, $n_2 = 1.5$.

single solid curve was drawn in Fig. 4 to represent these formulas. In the vicinity of $V = 2.4$, the simple equation (8) and consequently its approximation (20) are not exact. As long as the value of the propa-

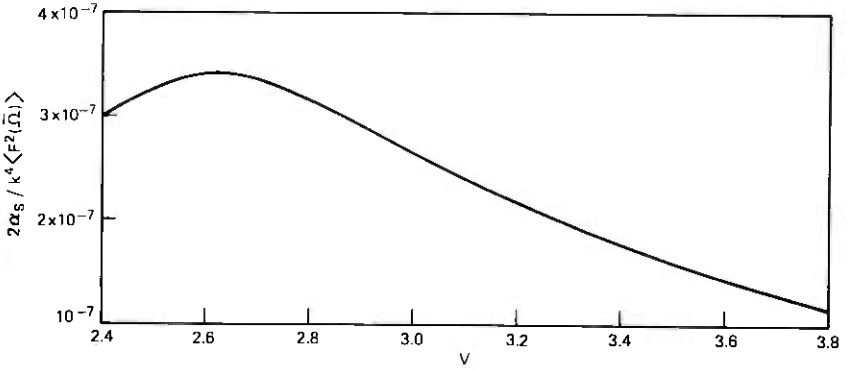

Fig. 4—Plot of eq. (20). This curve represents the normalized radiation loss of a quasi-single, HE_{11} mode in the presence of a leaky (next-higher-order) mode. The curve in this figure continues the curves in Fig. 3 to higher values of V, $n_1 = 1.515$, $n_2 = 1.5$.

gation constant β_1 is very close to n_2k, coupling to the radiation modes is not entirely negligible. It is apparent from Fig. 3 that the loss curves for different values of m have a tendency to converge to one curve. In Fig. 4 this convergence has taken place, but the transition from the many curves to one single curve is lost.

A comparison between the loss coefficients of the single-mode, step-index fiber and the multimode, parabolic-index fiber is possible only if certain assumptions are made. Figure 5 presents plots obtained from the loss formula (26) of the multimode fiber. We have drawn these curves by requiring $\theta_p = \Omega$ with Ω given by (3) and θ_p defined by (24). Multimode and single-mode fibers now sample the power spectrum at the same spatial frequency. The independent variable N in Fig. 5 represents the total number of modes that can propagate in the multimode fiber. As the number of modes changes, the fiber dimensions must change accordingly, keeping the value of θ_p constant.

The curves in Fig. 5 are labeled by the values of the normalized spatial frequency Ω/k; the corresponding values of the V number of the single-mode fiber are written in parenthesis. These V values are needed for a comparison of the loss values in Figs. 3 and 5. The normalized loss values are directly comparable since the same power spectrum at the same spatial frequency has been used in both cases. However, each curve of Fig. 5 must be compared with the curves in Fig. 3 at the proper V value. It is apparent that the loss of the multimode fiber can always be reduced below the loss of the single-mode fiber if the number of modes, N, is made large enough. For example, a single-mode fiber will normally be operated near $V = 2.4$. The corresponding curve (with $V = 2.4$) in Fig. 5 lies below the single-mode loss value

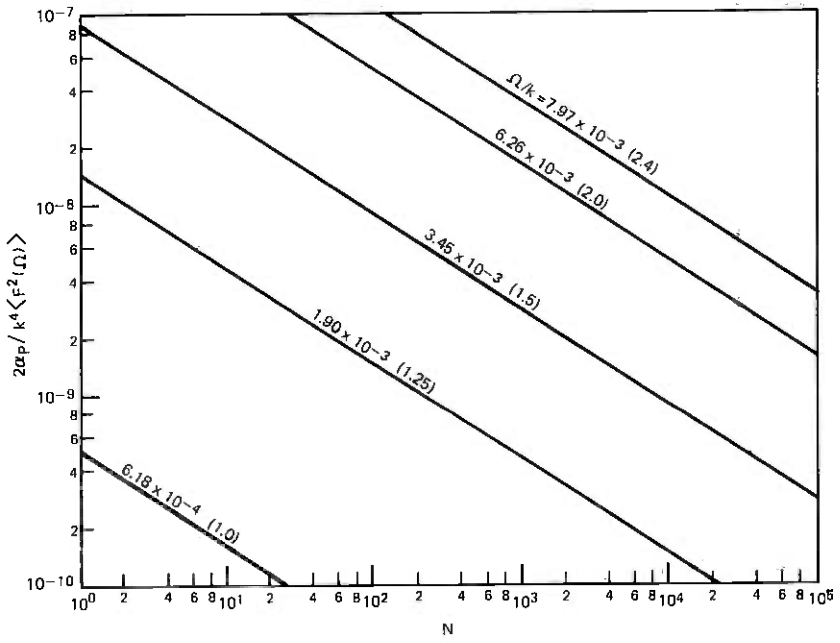

Fig. 5—Normalized loss coefficients of the multimode, parabolic-index fiber which is designed so that its spatial frequency θ_p [eq. (24)] coincides with the spatial frequency Ω [eq. (3)] of the single-mode fiber. The values of Ω/k label the curves; the values shown in parenthesis are the corresponding V values of the single-mode fiber.

for $N > 30$. For a fiber with $n_2 = 1.5$ and $\Delta = 0.01$, $N = 30$ corresponds to $ka = 52$, for $\lambda = 1$ μm we have a core radius of $a = 8$ μm.

Next we compare the microbending losses of single- and multimode fibers by assuming typical fiber parameters. Single-mode fibers must be designed to have a V value near $V = 2.4$. If the fiber has a narrow inner cladding surrounded by an outer cladding, whose refractive index is similar to that of the core, the leaky mode losses of modes of order higher than HE_{11} may be so large that the fiber behaves effectively as though it supported only one guided mode and its V value may be chosen to be above $V = 2.405$. After the V value has been chosen, it is desirable to make the core radius a as large as possible to ease the splicing problem. We assume that fiber core radius values in the range $a = 5$ μm to 10 μm are of interest. Thus, with $\lambda = 1$ μm, we are interested in ka values in the range $40 < ka < 60$. With $V = 2.4$, the corresponding index difference would be in the range $0.0005 < n_1 - n_2 < 0.002$; for $V = 3.5$, we have instead $0.001 < n_1 - n_2 < 0.0045$.

For a typical multimode, parabolic-index fiber, we use $\Delta = 0.01$ and let the core radius fall in the range $16 < a < 35$ μm so that with

$\lambda = 1\ \mu$m, we have $100 < ka < 220$. The cladding index is assumed to be that of fused silica, $n_2 = 1.457$, for both types of fibers. Since there is now no fixed spatial frequency that we may use for normalization purposes, we use the power spectrum at the spatial frequency $\theta = n_2 k\Delta$ to normalize the loss coefficient. This normalization uses the Δ value of the multimode fiber ($\Delta = 0.01$) and is certainly quite arbitrary, particularly for the single-mode fiber. However, a common normalization for both fiber types is necessary if we want to compare the loss values.

Figures 6 through 9 present normalized loss values for the single- and multimode fibers for $m = 4$, 6, 8, and 10. The single-mode losses are plotted as solid lines for different values of V; the dotted lines indicate the multimode loss values. The upper scale in the abscissa ranging from $ka = 30$ to $ka = 60$ applies to the single-mode curves, while the lower abscissa from $ka = 100$ to $ka = 220$ applies to the multimode curves. We have included two curves with $V = 3.1$ and

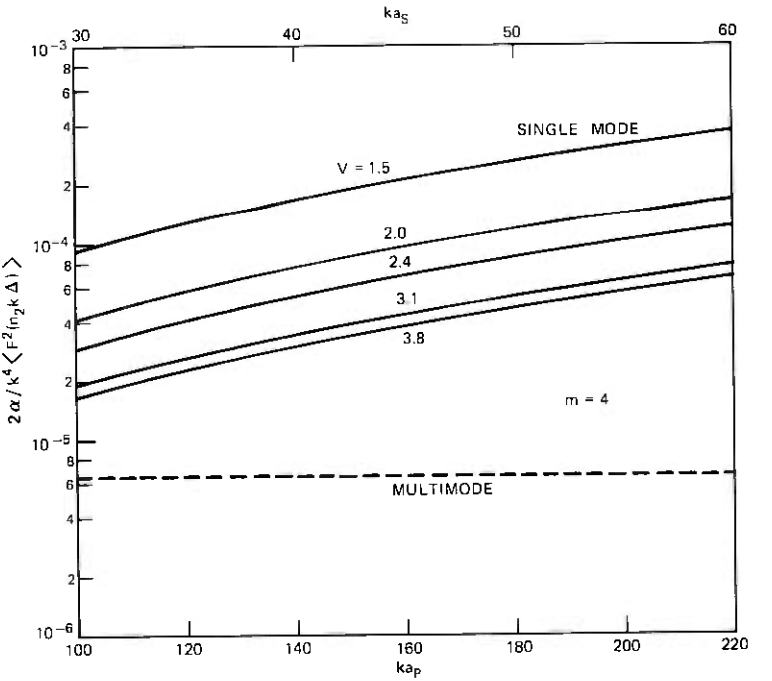

Fig. 6—Normalized radiation losses of single-mode (solid curves) and multimode (dotted curve) fibers. The upper scale on the abscissa applies to the single-mode case while the lower scale belongs to the multimode fiber. The power spectrum used for normalization of the loss factor is taken at the spatial frequency $\theta = n_2 k\Delta$ with $\Delta = 0.01$, $n_2 = 1.457$. This figure uses the exponent $m = 4$ of the power spectrum (12).

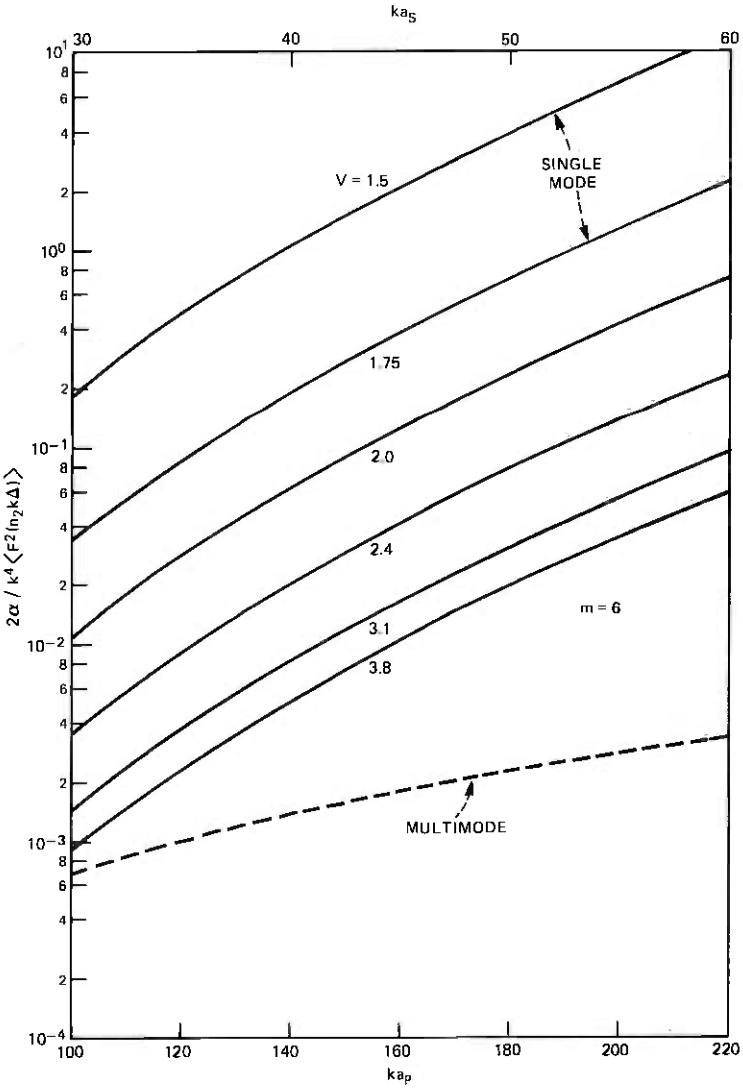

Fig. 7—Same as Fig. 6 with $m = 6$.

$V = 3.8$ in Figs. 6 through 9 to illustrate the case of a fiber that is not strictly speaking "single mode," but supports an additional leaky mode. The curves for V in the range $1.5 < V < 2.4$ were computed from (17) through (19) while the curves with $V = 3.1$ and $V = 3.8$ were computed from (20). The dotted curve for the parabolic-index fiber was obtained from (22).

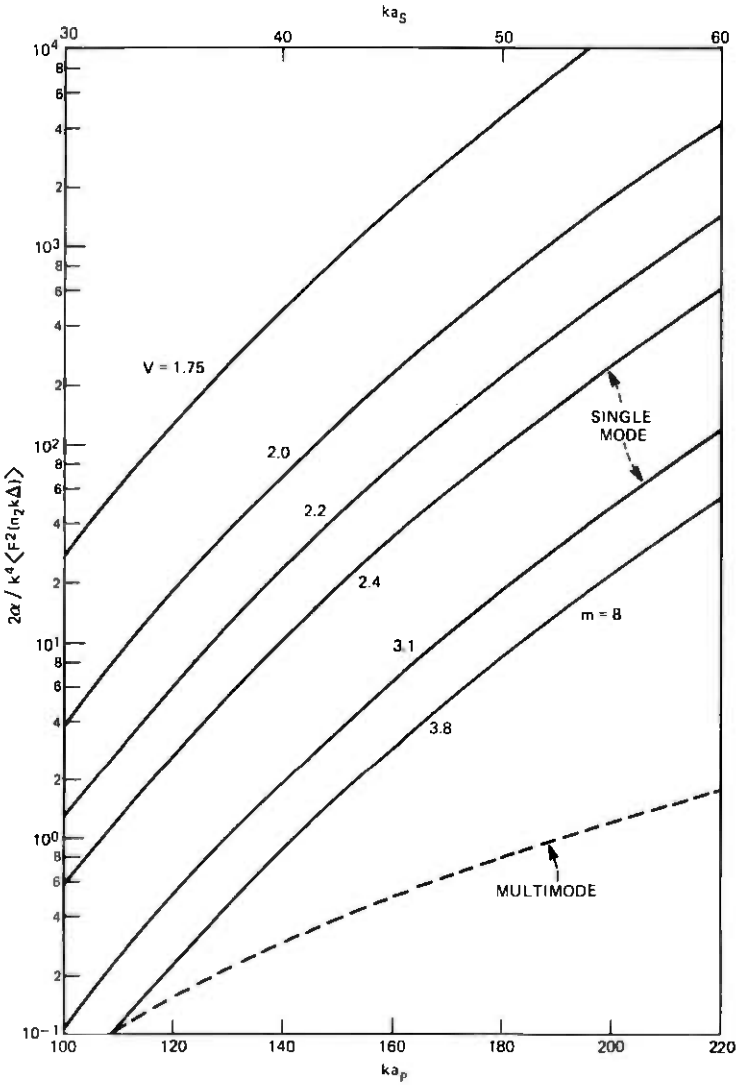

Fig. 8—Same as Fig. 6 with $m = 8$.

It is apparent that typical multimode fibers have lower losses than typical single-mode fibers.

VI. CONCLUSIONS

We have presented loss formulas for the single-mode, step-index fiber and for the multimode, parabolic-index fiber. The step-index fiber

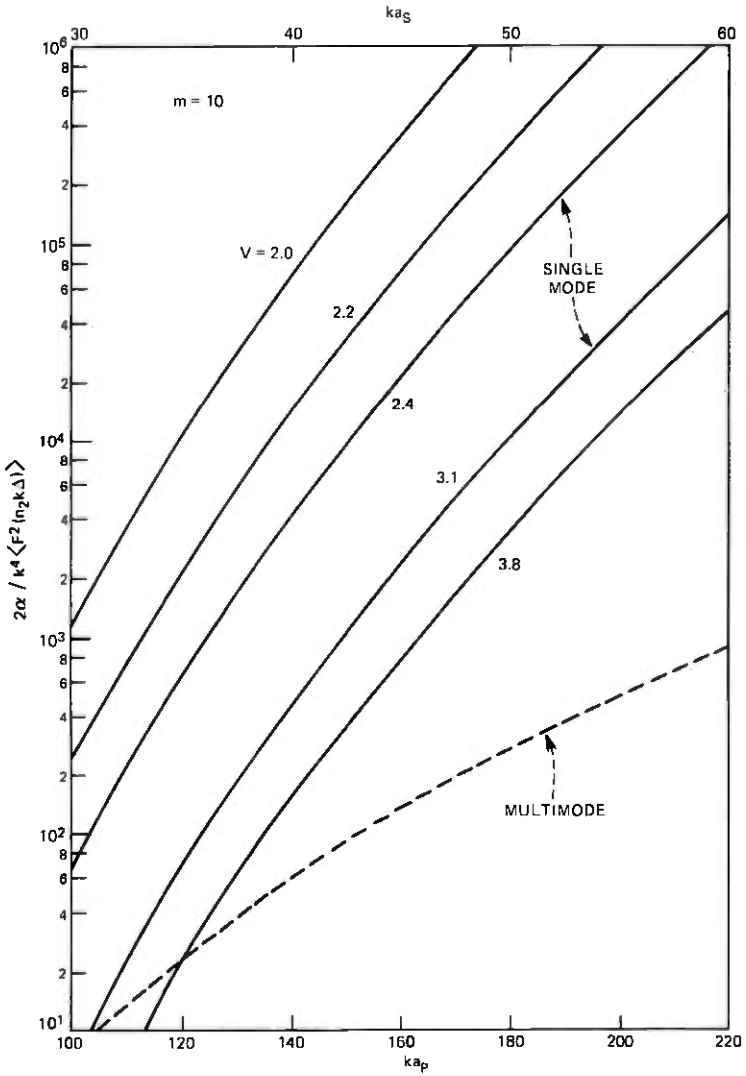

Fig. 9—Same as Fig. 6 with $m = 10$.

formulas were approximated by simple empirical approximations to obtain analytical expressions that can be easily evaluated with the help of a pocket calculator.

We compared the radiation losses of both fiber types that are caused by random deflections of the fiber axis. It was our objective to determine which fiber type is more sensitive to these microbending losses.

Our conclusion is that the single-mode fiber is more susceptible to microbending losses than the parabolic-index, multimode fiber. Since both fiber types are useful for wideband communications purposes using GaAs injection lasers or LEDs (in the case of the multimode fiber only), a knowledge of their respective microbending losses is important for system considerations.

VII. ACKNOWLEDGMENT

I am grateful to D. Gloge who suggested this study and contributed to it through several illuminating discussions. My thanks are also due to E. A. J. Marcatili who made many helpful suggestions.

APPENDIX

Validity of the Loss Formula in Equation (5)

Equation (5) was derived under the assumption that the fiber core is surrounded by an infinite cladding. Actually, cladding modes play the role of our radiation modes and the question arises: how accurate is a description of mode losses in terms of radiation modes? To answer this question, we compare the results of numerical evaluations of (5) with a theory published by Kuhn,[4] who uses cladding modes in a fiber with lossy jacket to calculate mode losses caused by random bends. Kuhn assumes that the curvature of the fiber can be described by either an exponential or gaussian correlation function. Since our formulation uses the function $f(z)$ to describe the fiber axis, we must first transform our equations into a form that allows us to compare it to a description in terms of fiber curvature. If we denote the power spectrum of the curvature function by $\langle C^2(\theta)\rangle$, the following relation holds:

$$\langle F^2(\theta)\rangle = \frac{\langle C^2(\theta)\rangle}{\theta^4}. \tag{27}$$

The variance of $f(z)$ is defined as

$$\bar{\sigma}^2 = \frac{1}{\pi}\int_0^\infty \langle F^2(\theta)\rangle d\theta. \tag{28}$$

The variance of the curvature spectrum is similarly defined as

$$\left\langle \left(\frac{1}{R}\right)^2 \right\rangle = \frac{1}{\pi}\int_0^\infty \langle C^2(\theta)\rangle d\theta. \tag{29}$$

If we define the power spectrum $\langle F^2\rangle$ with variance $\bar{\sigma}^2$, we can compute the corresponding variance for the curvature spectrum only if the integral (29) exists. For an exponential correlation function of the curvature, the power spectrum $\langle C^2\rangle$ has a Lorentzian shape[3] that re-

mains finite at $\theta = 0$ so that the integral in (28) does not exist. Correspondingly, (29) does not exist for a Lorentzian shaped $\langle F^2 \rangle$. Thus, a comparison between Kuhn's theory and ours is possible only for the gaussian correlation function.

Kuhn uses the following autocorrelation function for the fiber curvature:[4]

$$R_c(u) = \left\langle \left(\frac{1}{R} \right)^2 \right\rangle \exp(-u^2/D^2). \tag{30}$$

D is the correlation length. The power spectrum of the distortion function $f(z)$ is, thus,

$$\langle F^2(\theta) \rangle = \sqrt{\pi} \left\langle \left(\frac{1}{R} \right)^2 \right\rangle \frac{D}{\theta^4} \exp[-(\theta D/2)^2]. \tag{31}$$

Numerical integration of (5) yields the solid curve for the normalized radiation power loss shown in Fig. 10. This curve was computed for

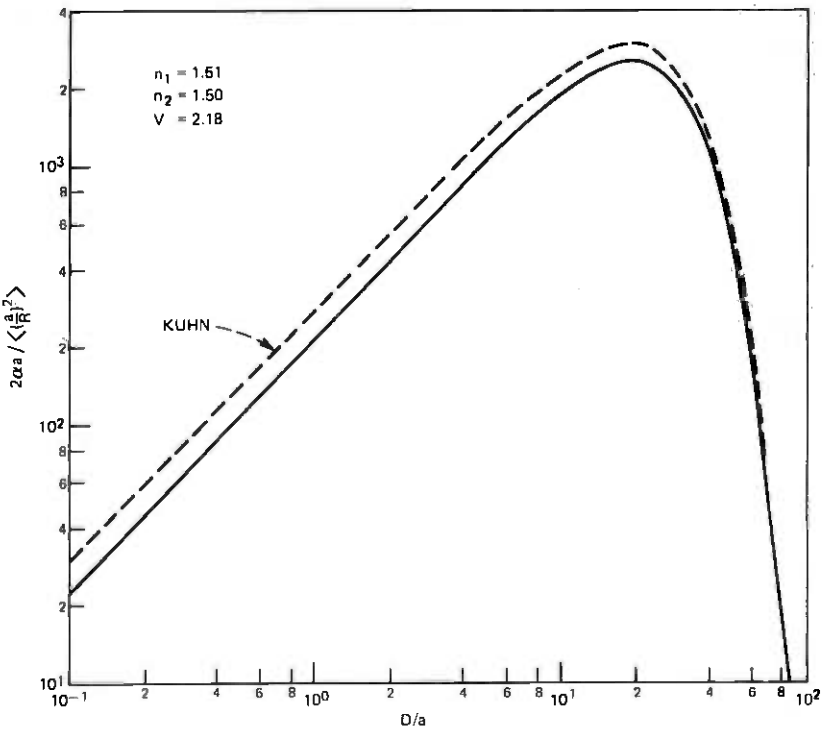

Fig. 10—Comparison between Kuhn's theory and our theory for $n_1 = 1.51$, $n_2 = 1.5$, and $V = 2.18$. The autocorrelation function of the fiber curvature is gaussian.

the following conditions:

$$n_1 = 1.51$$
$$n_2 = 1.5$$
$$ka = 12.56531.$$

These values lead to $V = 2.18$. The eigenvalue equation for LP modes[7] allows us to calculate $ka = 1.5851486$.

The dashed curve in Fig. 10 was obtained from Kuhn's publication.[4] It is apparent that the two theories agree very well for large correlation length corresponding to small spatial frequencies. The agreement is not quite as good for short correlation length or high spatial frequencies. Coupling spectra with large spatial frequencies lead to radiation escaping from the fiber core at large angles. Our eq. (5) is limited to small angle radiation. The solid curve in Fig. 10 was computed by using (5) for large correlation length, but using a corresponding formula derived with the help of free-space radiation modes for small correlation length. However, the longitudinal components of the guided and radiation modes were ignored, which led to an underestimation of the loss for radiation escaping at large angles. In the main part of this paper, we are interested only in coupling functions whose Fourier spectra drop off rapidly with increasing spatial frequency, so that only small spatial frequencies are important; eq. (5) is thus applicable. The comparison of our theory with Kuhn's shows that no large error results from using radiation modes instead of cladding modes to compute microbending losses.

REFERENCES

1. S. E. Miller, E. A. J. Marcatili, and T. Li, "Research Toward Optical Fiber Transmission Systems," Proc. IEEE, *61*, No. 12 (December 1973), pp. 1703–1751.
2. S. Kawakami and S. Nishida, "Characteristics of a Doubly Clad Optical Fiber with a Low-Index Inner Cladding," IEEE J. Quantum Electron., *QE-10*, No. 12 (December 1974), pp. 879–887.
3. D. Gloge, "Bending Losses in Multimode Fibers with Graded and Ungraded Core Index," Appl. Opt., *11*, No. 11 (November 1972), pp. 2506–2513.
4. M. H. Kuhn, "Curvature Loss in Single Mode Fibers with Lossy Jacket," AEÜ, *29*, No. 9 (September 1975), pp. 400–402.
5. D. Marcuse, "Theory of Dielectric Optical Waveguides," New York: Academic Press, 1974.
6. D. Marcuse, "Losses and Impulse Response of a Parabolic Index Fiber with Random Bends," B.S.T.J., *52*, No. 8 (October 1973), pp. 1423–1437.
7. D. Gloge, "Weakly Guiding Fibers," Appl. Opt., *10*, No. 10 (October 1971), pp. 2252–2258.
8. D. Marcuse, "Light Transmission Optics," New York: Van Nostrand Reinhold, 1972.
9. D. Marcuse, Excitation of Parabolic Index Fibers with Incoherent Sources, B.S.T.J., *54*, No. 9 (November 1975), pp. 1507–1530.

THE BELL SYSTEM TECHNICAL JOURNAL
Vol. 55, No. 7, September 1976
Printed in U.S.A.

Comparison of Equalizing and Nonequalizing Repeaters for Optical Fiber Systems

By S. D. PERSONICK

(Manuscript received October 15, 1975)

This paper compares the performances of equalizing and nonequalizing repeaters in optical fiber systems in the presence of delay distortion leading to intersymbol interference on the received optical pulse stream. Curves of receiver sensitivity loss vs delay distortion are computed for nonequalizing repeaters for various received optical pulse shapes. These results are then compared to previously published results for equalizing receivers. The results indicate that for modest delay distortion (less than 5 dB of receiver sensitivity loss) there are no significant advantages of the equalizing receiver over the nonequalizing type.

I. INTRODUCTION

This paper is concerned with the effects of intersymbol interference on the performance of equalizing and nonequalizing optical fiber system repeaters. Recent advances in the fabrication of graded-index optical fibers and improvements in laser lifetime should result in the ability to design fiber systems that are essentially loss-limited for data rates below 100 Mb/s. Nevertheless, it is interesting to study the effects of small amounts of intersymbol interference due to fiber delay distortion on the performance of optical fiber system repeaters.* Repeaters which can accommodate small amounts of intersymbol interference increase the yield of usable fibers in real cables where the index gradings are not ideal.

In a previous paper,[1] the effects of intersymbol interference on equalizing repeaters were studied. Such repeaters compensate for the fiber delay distortion (pulse spreading) by incorporating a high-frequency rollup filter in their linear channels. This rollup results in an enhancement of the receiver noise. Using the results of that paper, curves can be plotted of receiver sensitivity loss vs the spreading of the received optical pulses.

* Throughout this paper we shall assume that optical power pulses that overlap at the receiver add linearly, as justified in Ref. 3.

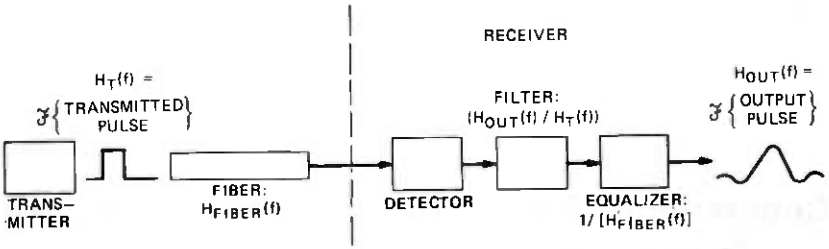

Fig. 1—Equalizing receiver.

In this paper, we shall present similar curves for nonequalizing repeaters. In such repeaters, pulse spreading results in an uncompensated closing of the receiver output "eye", leading to a sensitivity loss. Nonequalizing receivers do not require a knowledge of the

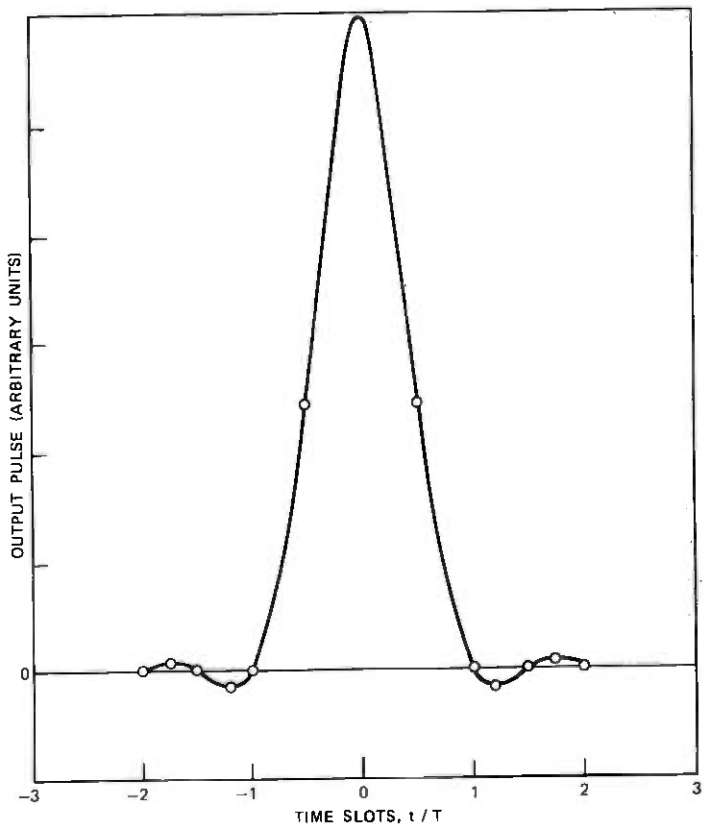

Fig. 2(a)—Ideal output pulse; $V_{out}(t)$, $T = 1.28$.

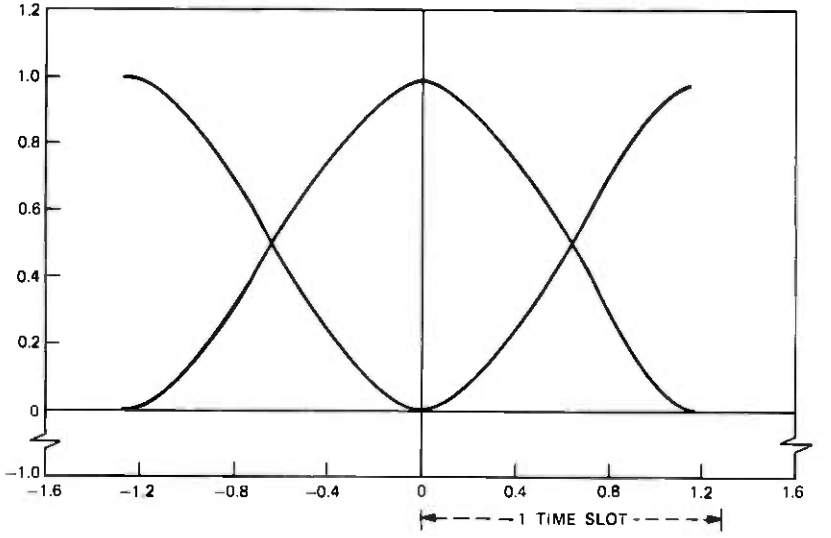

Fig. 2(b)—Ideal eye diagram; $V_{out}(t)$, $T = 1.28$.

received pulse shape. This is particularly important in systems using graded-index fibers, where residual pulse spreading, due to grading errors, can lead to unpredictable received pulse shapes.

Numerical results indicate that there is no significant advantage in equalizing over nonequalizing repeaters for sensitivity losses below 5 dB. There is no drastic deterioration in performance of the nonequalizing repeater compared to the equalizing type. As a consequence, the importance of hypothetical receivers that estimate the received pulse shape in order to adjust adaptive equalizers is considerably diminished.

II. THERMAL-NOISE-LIMITED SYSTEMS

This paper is concerned primarily with thermal-noise-limited systems. This restriction drastically simplifies the analysis compared to systems limited by randomly multiplied signal-dependent shot noise. We shall briefly discuss shot-noise-limited systems in Section III.

2.1 Equalizing receivers

An equalizing receiver is shown in Fig. 1. Observe that the output pulse shape $V_{out}(t)$ is independent of the fiber baseband frequency response $H_{fiber}(f)$. We assume that we have chosen $V_{out}(t)$ from the raised cosine family[1,2] with parameter $\beta = 1$. Figure 2 shows pictures of $V_{out}(t)$ and its associated "eye diagram." (The eye diagram is defined in the Appendix.)

The rms noise at the receiver output is dependent upon the fiber baseband frequency response (through the equalization) and the type of amplifier being used. If we normalize the eye opening to unity, we obtain an expression for the required optical power at the receiver input to achieve a 10^{-9} error rate of the following form[1]:

$$P_{\text{optical required}} = \frac{12h\Omega}{\eta} Z^{\frac{1}{2}}, \tag{1}$$

where

$\frac{h\Omega}{\eta}$ = photon energy/detector quantum efficiency

Z = normalized mean-square receiver output noise.[1]

In eq. (1), Z is an increasing function of the required equalization and is written in the following form:

$$Z = \gamma_1^2 \int_0^B |F_R(f)|^2/|H_{\text{fiber}}(f)|^2 df + \gamma_2^2 \int_0^B |F_R(f)|^2 f^2/|H_{\text{fiber}}(f)|^2 df, \tag{2}$$

where $F_R(f)$ depends upon the desired receiver output pulse and the transmitted pulse and is typically close to unity in value,

B = bit rate

γ_1, γ_2 = constants depending upon the amplifier being used.

In eq. (2), if the term involving γ_1 dominates, we have a low-impedance front end. If the term involving γ_2 dominates, we have a high-impedance front end.

Using eq. (2), we can calculate curves of the increase in required optical power (sensitivity loss) as a function of the fiber delay distortion.

2.2 *Nonequalizing receivers*

A nonequalizing receiver is shown in Fig. 3. In this receiver, the output pulse shape depends upon the baseband frequency response,

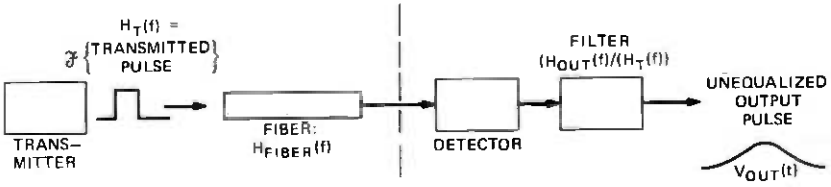

Fig. 3—Nonequalizing receiver.

but the rms noise, $Z^{\frac{1}{2}}$, does not. To calculate the receiver sensitivity, we must know the eye opening at the sampling time. We shall assume that in the absence of delay distortion in the fiber, $H_{\text{fiber}}(f) = 1$, the receiver output pulse is a raised cosine $\beta = 1$ pulse, as shown in Fig. 2. The output pulse and eye pattern resulting after delay distortion is included can be calculated in a straightforward manner. The required power to achieve a 10^{-9} error rate is given by

$$P_{\text{optical required}} = 12 \frac{h\Omega}{\eta} (\theta)^{-1} (Z_1)^{\frac{1}{2}}, \tag{3}$$

where

θ = eye opening at the sampling time ($\theta = 1$ corresponds to a completely open eye)

Z_1 = the value of mean squared thermal noise Z when there is no fiber delay distortion, i.e., Z of equation (2) with $H_{\text{fiber}}(f) = 1$.

2.3 Examples

Having defined the equalizing and nonequalizing receivers, we can now present computational results for the effects of fiber delay distortion. To make such calculations, we must specify the shape of the fiber impulse response $h_{\text{fiber}}(t)$, which is the Fourier transform of the fiber frequency response $H_{\text{fiber}}(f)$. In the examples below, we shall consider a variety of impulse response shapes.

2.3.1 Gaussian-shaped impulse response

In the absence of detailed knowledge of the fiber impulse response, we can begin by assuming a gaussian shape. Such a shape is appropriate for long fibers with mode mixing, and is given by the expression

$$h_{\text{fiber}}(t) = \exp - [\{(t/T)/(\sigma/T)\}^2/2], \tag{4}$$

where t/T is the time variable normalized to the units of time slots, and σ/T is the "rms width" of the impulse response in time slots.

Figure 4 shows curves of the deterioration of the receiver sensitivity as a function of σ/T. Curves are given for a nonequalizing receiver, a high-impedance equalizing receiver, and a low-impedance equalizing receiver. All curves are normalized to zero sensitivity loss for $\sigma/T = 0$ (sensitivity loss is the increase in required optical power in dB to maintain a fixed error rate). The curves do not show the relative performances of high- and low-impedance receivers but only the added effects of delay distortion. Figures 5 through 8 show receiver output eye diagrams and pulse shapes for $\sigma/T = 0.35$ and $\sigma/T = 0.55$ and a nonequalizing receiver.

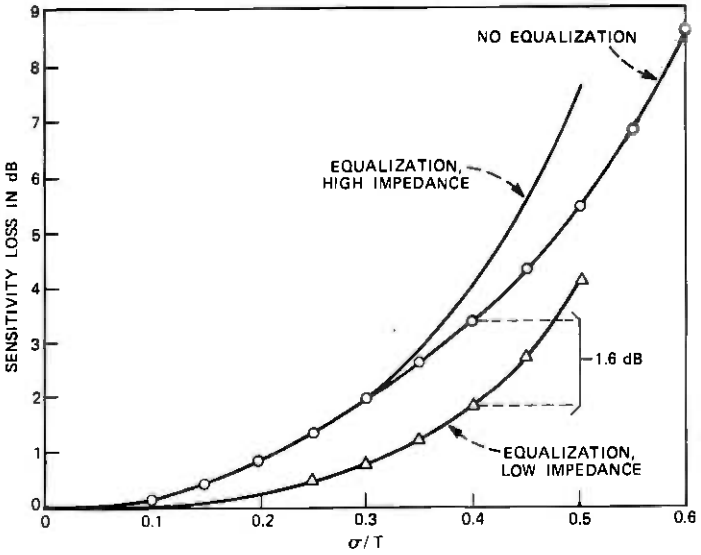

Fig. 4—Sensitivity losses vs σ/T for a gaussian impulse response, thermal noise limited.

In this example, we see that the nonequalizing receiver may be better or worse than the equalizing types depending upon the front-end design. (The optimal receiver would be some partial equalization

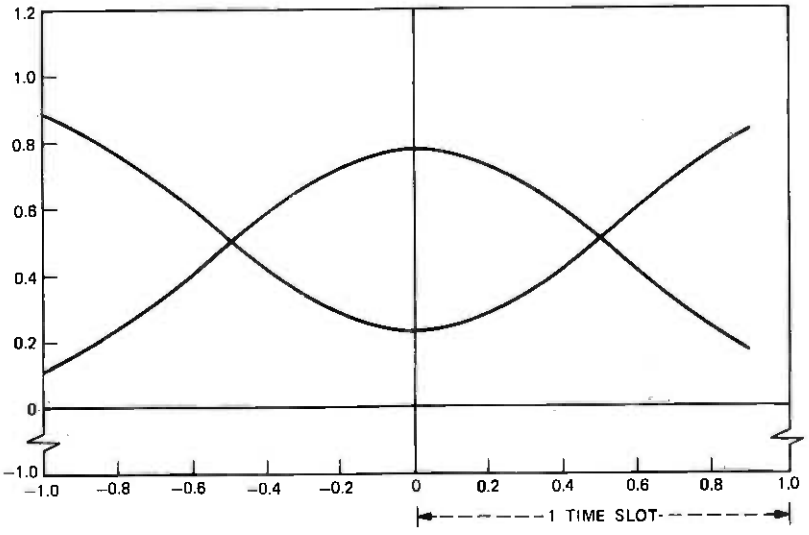

Fig. 5—Eye diagram for gaussian impulse response; $\sigma/T = 0.35$.

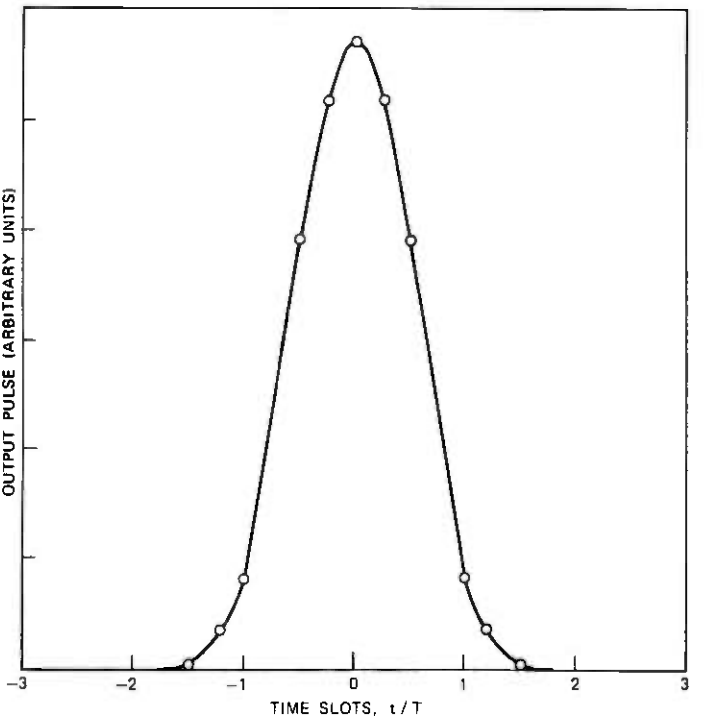

Fig. 6—Receiver output pulse for gaussian impulse response; $\sigma/T = 0.35$.

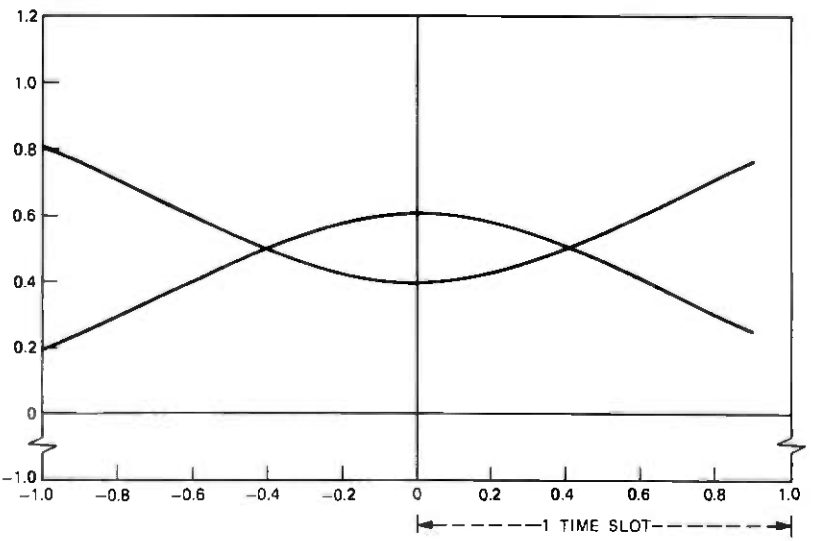

Fig. 7—Eye diagram for gaussian impulse response; $\sigma/T = 0.55$.

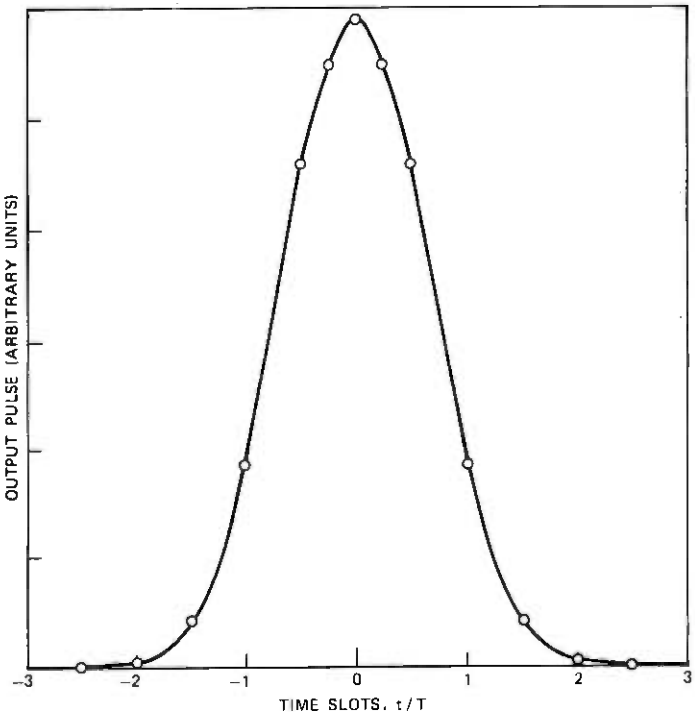

Fig. 8—Receiver output pulse for gaussian impulse response; $\sigma/T = 0.55$.

compromise between noise enhancement and intersymbol interference reduction.) The nonequalizing receiver does not deteriorate in performance at a significantly faster rate than the equalizing receiver.

2.3.2 Skew-shaped experimental pulse

Figure 9 shows a pulse response measured on an actual fiber. The fiber was 740 meters long. This pulse has an rms width $\sigma = 0.77$ ns. If we vary the bit interval T, we can calculate the receiver sensitivity loss for equalizing and nonequalizing receivers. The results are shown in Fig. 10. Figures 11 and 12 show the receiver output eye diagrams for $\sigma/T = 0.24$ and $\sigma/T = 0.6$. In Fig. 10, it is assumed that the nonequalizing receiver decision circuit samples the receiver output signal at the peak eye opening. This assumption is subject to further investigation concerning the design of timing recovery circuits.

We can propose a receiver which equalizes only the phase of the fiber baseband frequency response, leaving the amplitude rolloff uncompensated. Figure 13 shows the receiver sensitivity loss of such a phase-equalizing receiver vs σ/T. Also shown are the curves given in

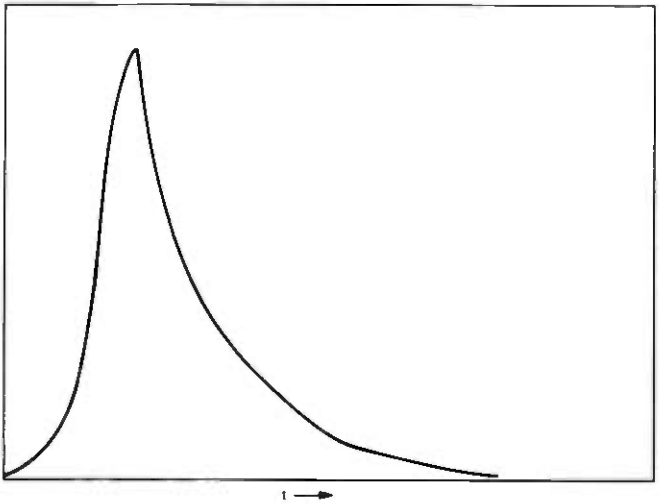

Fig. 9—Impulse response of borosilicate fiber 740 meters long.

Fig. 10. We note that the phase-equalizing receiver has no significant benefit over the nonequalizing receiver, except that sampling at the peak of the eye opening may be easier. Figure 14 shows the receiver output eye diagram for $\sigma/T = 0.6$ for the phase-equalizing receiver. This can be compared to Fig. 12.

2.3.3 Gaussian pulses on a pedestal

In fibers with graded indices, it is sometimes observed that the impulse response can be divided into two parts: (*i*) a narrow part

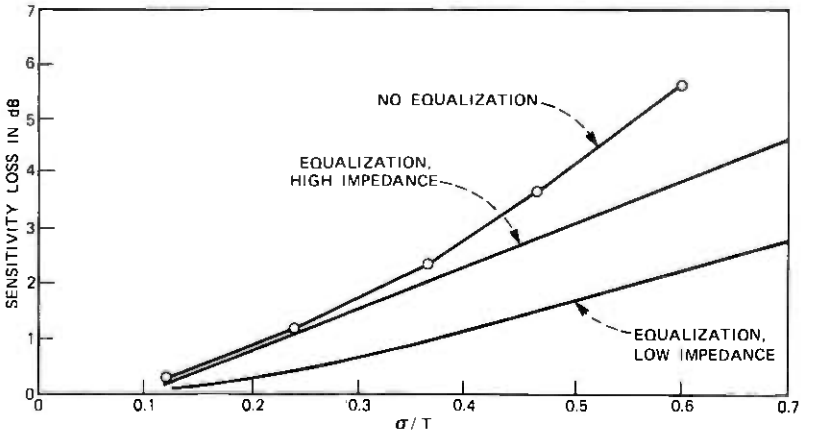

Fig. 10—Sensitivity losses vs σ/T for borosilicate fiber.

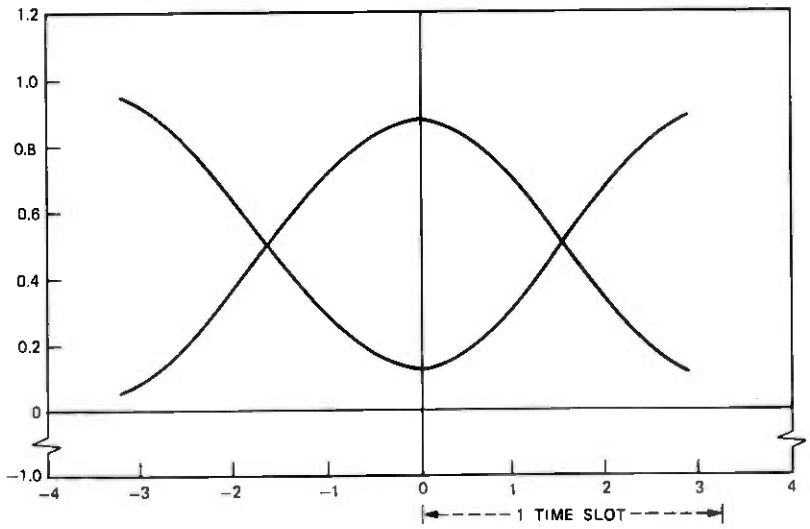

Fig. 11—Eye diagram for borosilicate fiber; $\sigma/T = 0.24$.

containing (hopefully) most of the energy and (*ii*) a wider part (tail) corresponding to high-order modes with long delays, or cladding modes coupled to the core modes. To simulate the effect of such a fiber impulse response on the system, we model it as the sum of a gaussian-

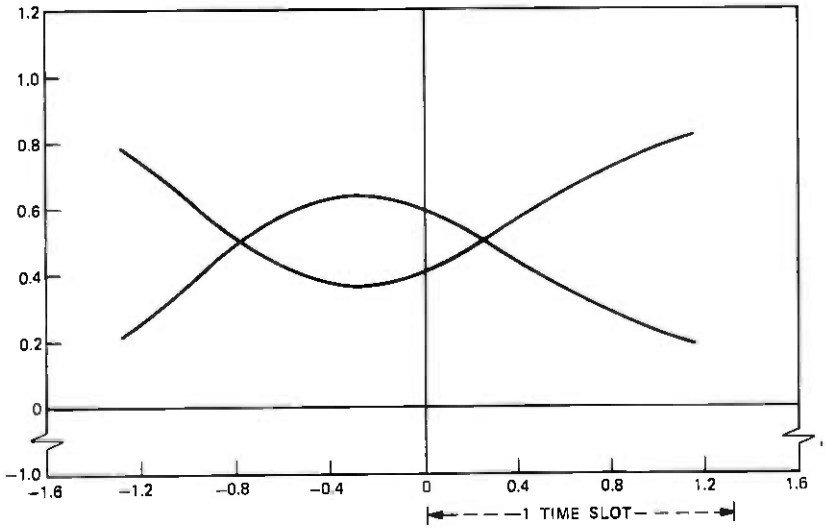

Fig. 12—Eye diagram for borosilicate fiber 740 meters long; $\sigma/T = 0.60$.

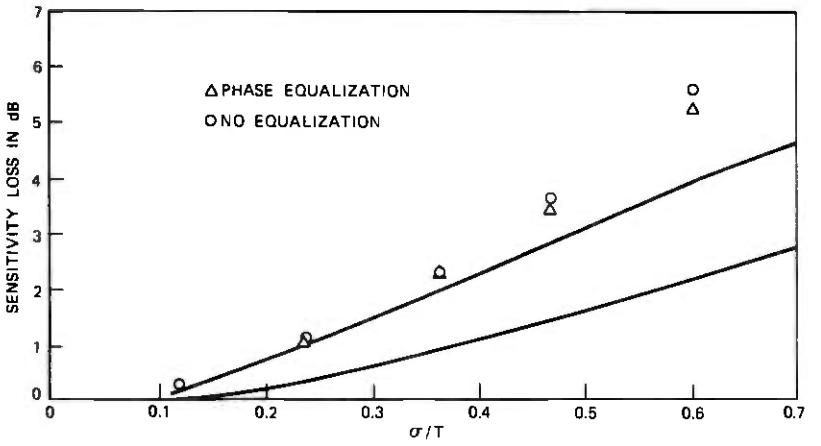

Fig. 13—Sensitivity losses vs σ/T for borosilicate fiber (includes phase equalization).

shaped pulse of area $(1 - \Delta)$ and rms width σ and a rectangular pulse of area Δ and full width W. An example is shown in Fig. 15.

Because of the uncertainty in the values of Δ, σ/T, and W/σ, which will be encountered in practice, we shall consider two cases:

Case 1: $W/\sigma = 6.4$, $\sigma/T = 0.5$, and $0 \leqq \Delta \leqq 0.2$.
Case 2: $W/\sigma = 12.8$, $\sigma/T = 0.25$, $0 \leqq \Delta \leqq 0.34$.

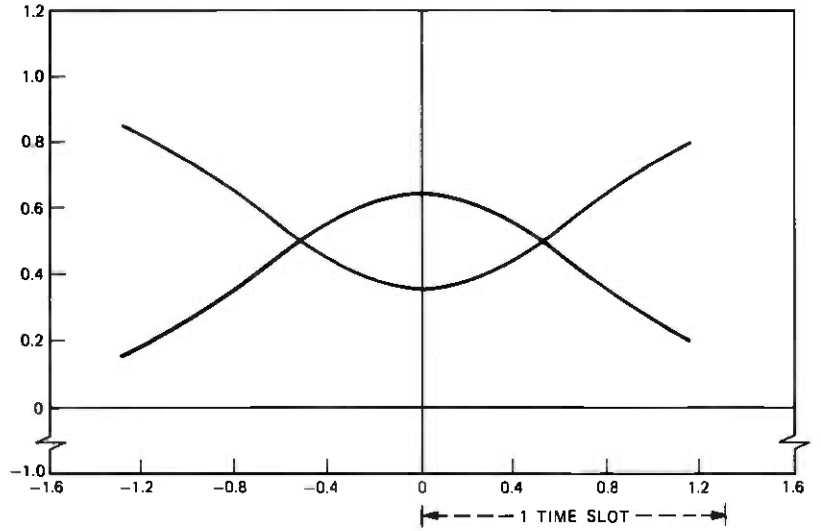

Fig. 14—Eye diagram after phase equalization for borosilicate fiber 740 meters long; $\sigma/T = 0.60$.

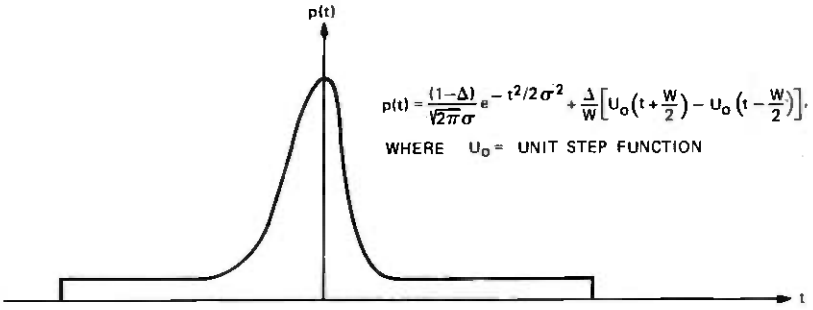

Fig. 15—Gaussian pulse on a pedestal.

Figures 16 and 17 show calculations of receiver sensitivity loss (relative to a very-narrow-shaped fiber impulse response) as a function of Δ for cases 1 and 2, respectively, and for different receivers. Also shown are curves of 10 log $[1/(1 - \Delta)]$ which correspond to the loss of total pulse energy to the pulse tail. We observe that tails affect the nonequalizing receiver more than the equalizing receiver. However, more calculations must be made to understand fully the effects of tails and how to combat those effects. Before these calculations can be made, more data on the impulse response of real fibers are needed.

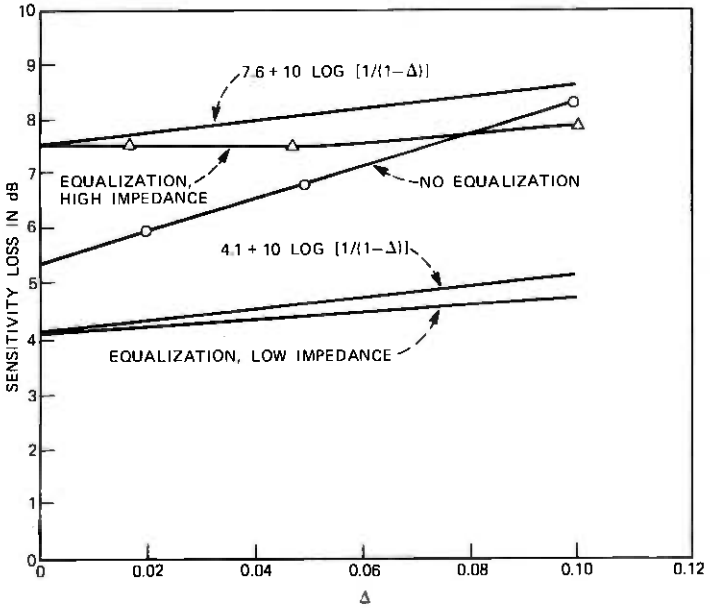

Fig. 16—Receiver sensitivity loss for Case 1: $\sigma/T = 0.5$ and $W/\sigma = 6.4$.

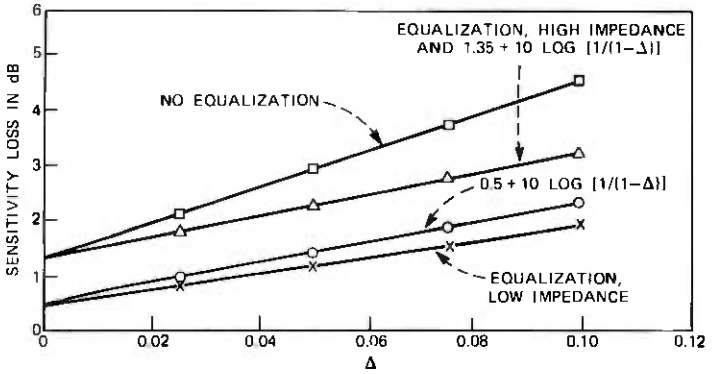

Fig. 17—Receiver sensitivity loss for Case 2: $\sigma/T = 0.25$ and $W/\sigma = 12.8$.

III. SHOT-NOISE-LIMITED SYSTEMS (AVALANCHE GAIN)

The extension of the previous results to shot-noise-limited systems requires one to take into account the signal dependence of shot noise. A rough approximation suitable for comparing nonequalizing and equalizing receivers in the following. For equalizing receivers, we can use the techniques described in Ref. 1 to calculate receiver performance degradation with increasing fiber delay distortion. Nonequalizing

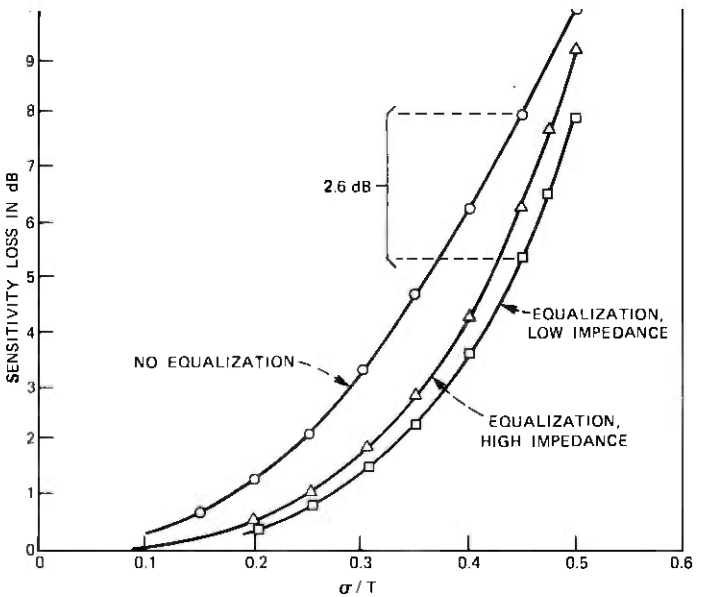

Fig. 18—Sensitivity losses vs σ/T for a gaussian impulse response, shot noise limited.

receivers can be studied by assuming that the shot noise at the receiver output is proportional to the average optical power falling on the detector, but is only weakly dependent upon the shape of the received pulses. In that case, the required received optical power increases approximately as $-50/6$ log (eye opening).[1] This can be compared to the thermal-noise-limited receiver where the required optical power increases as $-30/6$ log (eye opening).

An example of a receiver with avalanche gain is shown in Fig. 18. The figure shows a plot of receiver sensitivity loss vs σ/T for a gaussian fiber impulse response and for equalizing and nonequalizing receivers.

IV. ACKNOWLEDGMENT

The author gratefully acknowledges the work of Diane Vitello in writing programs to perform many of the above calculations.

APPENDIX

Receiver Output Eye

The output of the optical fiber receiver consists of a sequence of pulses plus noise:

$$V_{\text{out}}(t) = \sum_{k=-\infty}^{\infty} a_k h_{\text{out}}(t - kT) + n(t), \tag{5}$$

where

a_k = 0 or 1 represents the information
T = pulse spacing
$n(t)$ = noise.

In general, these pulses overlap, a characteristic which is referred to as intersymbol interference. Once every T seconds, the output is sampled (observed) to decide whether or not a pulse is present ($a_k = 1$ or $a_k = 0$). In the absence of intersymbol interference, the ability to make this decision is limited by the noise. However, due to intersymbol interference, the receiver output at the sampling time can be smaller or larger than it would be if only one pulse were present. Pessimistically, we can calculate the smallest value that $V_{\text{out}}(t)$ can assume given that the pulse we are looking for is on ($a_k = 1$), and we can also calculate the largest value that $V_{\text{out}}(t)$ can assume given that the pulse we are looking for is off ($a_k = 0$); h_{out} both of these neglect noise $n(t)$.

$$\begin{aligned} V_{\text{min on}}(t) &= h_{\text{out}}(t - kT) + \sum_{k' \neq k} [\text{min of } h_{\text{out}}(t - k'T) \text{ and } 0] \\ V_{\text{max off}}(t) &= \sum_{k' \neq k} [\text{max of } h_{\text{out}}(t - k'T) \text{ and } 0]. \end{aligned} \tag{6}$$

The "eye diagram" is a plot of $V_{\text{min on}}(t)$ and $V_{\text{max off}}(t)$ on the same abscissa (see Figs. 5 and 6). The maximum difference between the upper and lower curves (before they cross) is called the eye opening. This maximum difference occurs at a point in time where the best chance to distinguish between "pulse present" and "pulse absent" exists. The ratio of this peak eye opening to the peak height of an isolated pulse represents a loss in noise immunity and is called the fractional eye opening.

REFERENCES

1. S. D. Personick, "Receiver Design for Digital Fiber Optic Communications Systems," B.S.T.J., *52*, No. 6 (July-August 1973), pp. 843–886.
2. R. Lucky, J. Salz, and E. J. Weldon, *Principles of Data Communications*, New York: McGraw–Hill, 1968.
3. S. D. Personick, "Baseband Linearity and Equalization in Fiber Optic Digital Communication Systems," B.S.T.J., *52*, No. 7 (September 1973), pp. 1175–1194.

THE BELL SYSTEM TECHNICAL JOURNAL
Vol. 55, No. 7, September 1976
Printed in U.S.A.

Derivative Measurements of Light-Current-Voltage Characteristics of (Al,Ga)As Double-Heterostructure Lasers

By R. W. DIXON

(Manuscript received February 17, 1976)

A modulation and detection scheme for applying derivative techniques to the investigation of stripe geometry (Al, Ga)As double-heterostructure lasers is described. Modulating at constant modulation index allows the quantities $I(dV/dI)$ and $I^2(d^2V/dI^2)$ to be directly obtained in the same apparatus at the first and second harmonic of the modulation frequency, respectively. Particularly strong indications of laser action and other optical interactions in the laser are contained in the second harmonic voltage response. The same apparatus may be used to obtain derivatives of the light-current relation. These are found to sensitively reveal light-current nonlinearities that are believed caused by filaments and other spatial inhomogeneities and instabilities.

I. INTRODUCTION

Derivative techniques are employed in many fields of science and engineering. Reasons for their use range from the enhancement of signal-to-noise ratio, as in nuclear magnetic resonance and optical reflectivity investigations of band structure, to the convenience of direct measurement of dynamic transistor characteristics. Usually the techniques measure system response to a small ac modulation, often using phase detection for signal enhancement.

These techniques have recently been successfully applied to an analysis of the current-voltage characteristics of GaAs injection lasers. The first derivative dV/dI has been shown to be useful, both in homojunction[1] and in double-heterostructure lasers,[2] for measuring the parameters entering the I–V characteristic as well as for extracting lasing threshold and other features intimately related to the lasing process.

This paper describes a modulation and detection technique which has the advantage of allowing the direct measurement of $I(dV/dI)$,

which is often the desired quantity (rather than dV/dI). The technique also allows direct measurement of $I^2(d^2V/dI^2)$. Very strong second-derivative signals near and above lasing threshold are observed. Additionally, derivatives of the light-current characteristic are displayed and, as anticipated, show much sharper detail, near lasing threshold, and when filamentary instabilities occur, than does the light-current characteristic itself. All of these properties can be measured in the same apparatus.

II. SIMPLE THEORY

Much of the value of the experimental technique results from the modulation of the laser current at constant modulation index, $m = \Delta I/I = \text{constant}$, rather than alternatives such as constant modulation amplitude, ΔI. To appreciate the reasons for this advantage consider a laser modeled as an ideal p–n junction in series with a resistance of value R_s.[1,2] The current-voltage characteristic of this idealized device would be

$$I = I_0[e^{\beta(V-IR_s)} - 1], \tag{1}$$

where conventionally $\beta \equiv q/nkT$, and the other parameters have their usual meanings. Solving eq. (1) for V, neglecting in this context the -1 term, and the current dependences of the parameters of eq. (1), and differentiating yields[1,2]

$$\frac{dV}{dI} = \frac{1}{I\beta} + R_s \tag{2}$$

and

$$\frac{d^2V}{dI^2} = -\frac{1}{\beta I^2}. \tag{3}$$

For many purposes,[2] the preferred forms of eqs. (2) and (3) are

$$I\frac{dV}{dI} = \frac{1}{\beta} + IR_s \tag{2a}$$

and

$$I^2\frac{d^2V}{dI^2} = -\frac{1}{\beta}, \tag{3a}$$

thus allowing the direct extraction of the parameters β and R_s without having to deal with the inverse current dependences. (See Appendix.) Also, the forms (2a) and (3a) lend themselves to the investigation of the small I-V changes which occur because of the optical-electrical interactions in the laser. It is worth emphasizing that direct measurements of the quantities $I(dV/dI)$ and $I^2(d^2V/dI^2)$ are desired as

opposed to the synthesis of these quantities from other measured parameters. This improves both the measurement accuracy and the experimental simplicity.

To see how this is possible consider that a current of the form, $I_T = I + \Delta I \cos \Omega t$ is applied to the diode, the response voltage is expanded in a Taylor series, and coefficients in Ω and 2Ω collected. The result is

$$V(\Omega) = mI \frac{dV}{dI} \tag{4}$$

and

$$V(2\Omega) = \left(\frac{m}{2}\right)^2 I^2 \frac{d^2V}{dI^2}, \tag{5}$$

where $m \equiv (\Delta I/I)$ is the modulation index, and only lowest-order terms have been retained.* Thus, if the laser can be modulated keeping the modulation index constant, the desired quantities may be obtained directly at the frequencies Ω and 2Ω.

III. EXPERIMENTAL

3.1 Detection at the modulation frequency (Ω)

The experimental apparatus used is shown in Fig. 1. The key component is the current source. It has, as an offshoot of the feedback circuitry that maintains a constant current for varying load impedance, the property that it can be easily modified so that modulation *at constant* m occurs when an appropriate low-frequency (<1 kHz) ac signal is applied. When the phase detector is tuned to the modulation frequency Ω [mode (a) in Fig. 1], laser response voltages like that labeled $I(dV/dI)$ in Fig. 2 are obtained. This curve has features analogous to those seen previously.[1,2] These include y-axis intercept [equal to $1/\beta$ on the simple theory, eq. (2a)], the slope (proportional to series resistance R_s on the simple theory), and an indication of voltage saturation near lasing threshold. System response was checked both with resistors and with a silicon diode replacing the laser, and the known values of R and β were reproduced very well. The signal $V(\Omega)$ was also confirmed to be linearly proportional to m as expected from eq. (4). Many different lasers were measured and their results seemed generally similar although major deviations from slope linearity below threshold were sometimes observed, as were significant differences among the forms of the $I(dV/dI)$ responses near and above lasing threshold. Voltage saturation was almost never complete, and

* Higher-order corrections depend on higher powers of m and are not significant for m small.

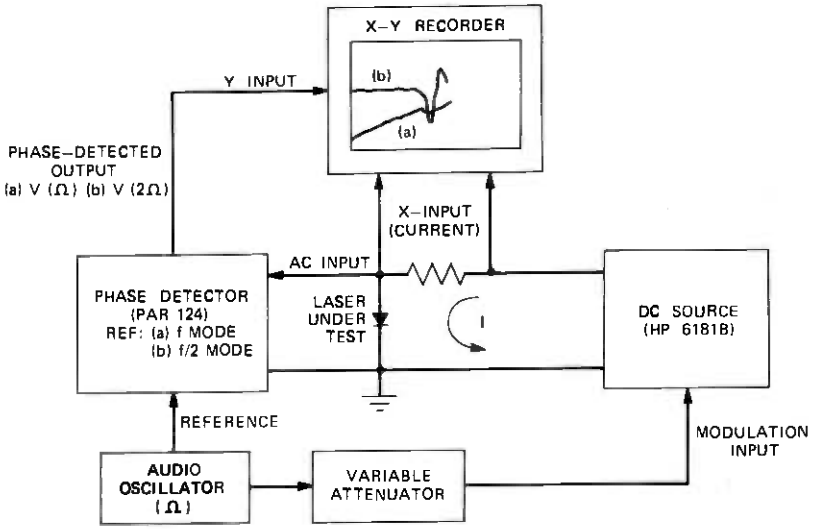

Fig. 1—Schematic diagram of apparatus used to obtain voltage and light derivatives in (Al, Ga)As double-heterostructure lasers. Mode (a) detects $V(\Omega) \propto I(dV/dI)$ and mode (b) detects $V(2\Omega) \propto I^2(d^2V/dI^2)$.

filament changes resulted in complex $I(dV/dI)$ responses. The experimental technique, however, seems accurate, easily calibrated, and simple to use.

3.2 Detection at twice the modulation frequency (2Ω)

An important advantage of this technique is that it can also be used to measure the voltage response at frequency 2Ω and thus to obtain the second derivative $I^2(d^2V/dI^2)$. Detection at frequency 2Ω was accomplished by operating the phase detector in the $f/2$ mode [mode (b) in Fig. 1]. In this mode, the instrument produces an internal reference frequency at exactly twice the frequency of the externally applied reference, thus making the detection system sensitive to $V(2\Omega)$.

Trace (b) of Fig. 2 shows a typical signal detected with the system operated in the 2Ω mode. As anticipated, the signal-to-noise ratio is very large. The initial shape (with current increasing) seems quite reproducible from laser to laser while the structure at higher currents is laser-dependent. Again, the signal appears greatly affected by filamentary laser operation. When the laser was shorted or replaced by a resistance, a horizontal straight line resulted, as expected. As an additional check, the dependence of $V(2\Omega)$ on modulation index was measured below threshold over the range $0 \leqq m \leqq 0.10$ and confirmed to be accurately m^2, consistent with theory [eq. (5)]. Thus, there is

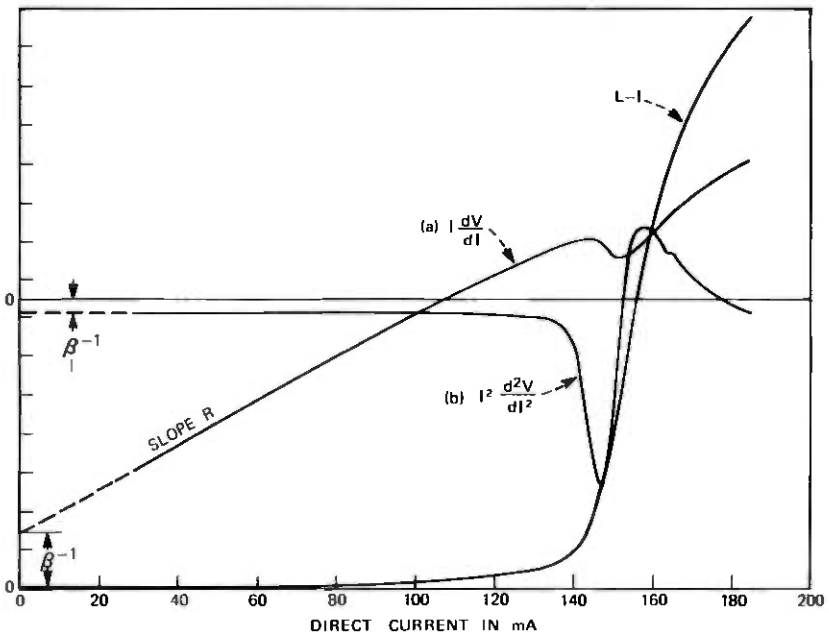

Fig. 2—Typical $V(\Omega)$ and $V(2\Omega)$ responses [curves (a) and (b)] as functions of laser current measured using apparatus of Fig. 1. The zero current intercept of $I(dV/dI)$ and the initial negative offset of $I^2(d^2V/dI^2)$ are proportional to $\beta^{-1} \equiv (nkT/q)$ when the simple model described in the text is valid. Note voltage saturation in $I(dV/dI)$ and the very strong second-derivative signal near threshold.

little indication of feedthrough from the first harmonic or of harmonic distortion of the modulating frequency affecting the detected voltage at the second harmonic. If very accurate measurements were contemplated, this would merit more serious investigation (see, for example, Korb and Holonyak[3*]).

3.3 *Light-current derivatives*

Using the circuit depicted in Fig. 1, the derivatives $I(dL/dI)$ and $I^2(d^2L/dI^2)$ can also be directly obtained. This was accomplished by placing the laser in a holder in which the optical emission from each mirror face could be separately monitored with silicon photodiodes. The photodiode current then served as the input to the phase detector. This more traditional application of derivative techniques may prove to be a useful adjunct to $L(I)$ measurements, not only to provide

* Also, T. L. Paoli has considered a more complex technique wherein modulation is provided at two frequencies Ω_1 and Ω_2 and the system response is sought at frequency $|\Omega_1 - \Omega_2|$, thus eliminating the harmonic relationship with the interfering signals.

accurate measurement of parameters, such as differential quantum efficiency [$\propto (dL/dI)$], but also to investigate filaments and other spatial inhomogeneities in the laser cavity. Typical derivative signal responses are shown in Fig. 3 along with a light-output-current characteristic measured in the same apparatus. A device with significant curvature in the L-I was used as an example to illustrate the enhancement of such slope changes using the derivatives. As expected from earlier results,[4] the emission from the two laser mirrors was often unsymmetric and was usually very unsymmetric when L-I kinks[5] were present. These kinks are thought[4] to be associated with spatial inhomogeneities in the laser cavity. This nonsymmetry was also present in the light-current derivatives. Very sharp derivative structure was seen near the light-current kinks. These observations strongly suggest that light-current derivatives, either alone or in combination with voltage derivatives, will prove very useful for investigating light-current nonlinearities, spatial inhomogeneities, and their relationship in injection lasers.

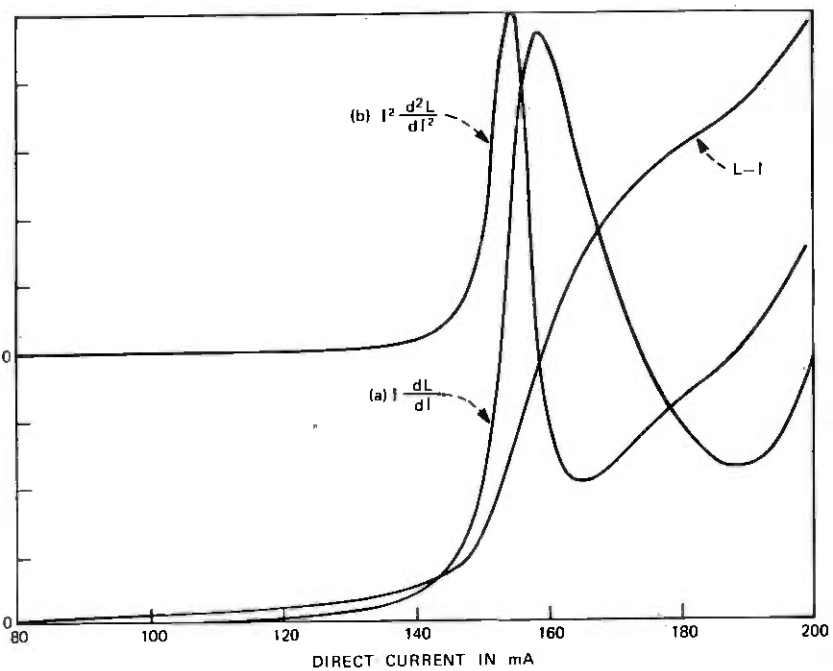

Fig. 3—Typical results for $I(dL/dI)$ and $I^2(d^2L/dI^2)$ vs current in an (Al, Ga)As double-heterostructure laser taken with the apparatus shown in Fig. 1, except that the signal input to the phase detector was obtained from a silicon detector monitoring the light emission from the laser.

IV. SUMMARY AND CONCLUSION

An experimental technique has been described which allows modulation of an (Al, Ga)As double-heterostructure laser at constant modulation index. Derivative techniques were then discussed which illustrate the usefulness of this property in measuring the derivatives $I(dV/dI)$ and $I^2(d^2V/dI^2)$ to extract the parameters describing a laser's I-V relation and to investigate lasing-related voltage changes in this relation. Derivatives of light with respect to current were also obtained in the same apparatus. These results support the conclusion that derivative techniques will be very helpful in studying (Al, Ga)As lasers and similar devices.

V. ACKNOWLEDGMENTS

The author wishes to thank Y. P. Lai and J. F. Svacek for their technical assistance.

APPENDIX

The neglect of the -1 term is not thought to be significant. However, the assumptions of β, R, and i_0 independent of current may sometimes be unjustified. If β depends on current through the parameter n, the first-order correction to the derived value of n is

$$\Delta n(I) = \frac{q}{kT}(V - IR_s)\frac{I}{n}\frac{dn}{dI}.$$

This correction can be large for quite reasonable I-V characteristics. Equivalently we find instead of eq. (2a)

$$I\frac{dV}{dI} = \frac{1}{\beta} + V\frac{I}{n}\frac{dn}{dI} + IR_s\left(1 - \frac{I}{n}\frac{dn}{dI}\right). \tag{2b}$$

Thus, both of the derived parameters β and R_s are sensitive to the assumption of β independent of current.

Analogous comments apply in the second derivative case where (3a) is replaced by

$$I^2\frac{d^2V}{dI^2} = -\frac{1}{\beta}\left(1 - 2\frac{I}{n}\frac{dn}{dI}\right) + (V - IR_s)\frac{I^2}{n}\frac{d^2n}{dI^2}. \tag{3b}$$

Expressions applicable when $R = R(I)$ or $I_0 = I_0(I)$ are easily derived.

REFERENCES

1. P. G. Eliseev, A. I. Krasil'nikov, M. A. Man'ko, and V. P. Strakhov, "Investigation of dc Injection Lasers," in *Physics of p–n Junctions and Semiconductor Devices*, ed. S. M. Ryvkin and Yu. V. Shmartsev, New York: Plenum, 1971, p. 150.

2. T. L. Paoli and P. A. Barnes, "Saturation of the Junction Voltage in Stripe-Geometry (Al, Ga)As Double-Heterostructure Junction Lasers," Appl. Phys. Lett., *28*, No. 12 (June 1976), pp. 714–716.
3. H. W. Korb and N. Holonyak, Jr., "Measurement System for Derivative Studies," Rev. Sci. Instrum., *43*, No. 1 (January 1972), pp. 90–94.
4. R. W. Dixon, F. R. Nash, R. L. Hartman, and R. T. Hepplewhite, "Improved Light-Output Linearity in Stripe-Geometry Double-Heterostructure (Al, Ga)As Lasers," Appl. Phys. Lett., *29*, No. 6 (September 15, 1976), pp. 372–374.
5. See, e.g., R. L. Hartman and R. W. Dixon, "Reliability of DH GaAs Lasers at Elevated Temperatures," Appl. Phys. Letters, *26*, No. 5 (March 1975), pp. 239–242.

THE BELL SYSTEM TECHNICAL JOURNAL
Vol. 55, No. 7, September 1976
Printed in U.S.A.

On Kailath's Innovations Conjecture Hold

By V. E. BENEŠ

(Manuscript received October 30, 1975)

With $z_\cdot$ a signal process, $w_\cdot$ a Brownian motion, and $y_t = \int_0^t z_s ds + w_t$ a noisy observation, the innovations problem is to determine whether $y_\cdot$ is adapted to the innovations process $\nu_\cdot$, which is also a Brownian motion, and is defined using the estimate $\hat{z}_t = E\{z_t | y_s,\ 0 \leqq s \leqq t\}$ by $y_t = \int_0^t \hat{z}_s ds + \nu_t$. The closely related σ-algebras problem in stochastic DEs is to determine, for a given causal drift α, when a solution of $d\xi = \alpha(t, \xi)dt + dw$ is a causal functional of $w_\cdot$. Previous results on these problems are reviewed and extended. In particular, we broach and answer positively the physically important case of the innovations problem in which the signal satisfies a stochastic DE with drift depending in part on the noisy observations. This case is important because it models a system observed through noise and controlled by feedback of these noisy observations. The last part of the paper shows that the innovations problem has a positive resolution if and only if on some probability space there is a Brownian motion W and a causal solution ξ of $d\xi = \alpha(t, \xi)dt + dW$, where α expresses the estimator $\hat{z}$; that is, α is a causal functional such that $\hat{z}_t = \alpha(t, y)$.

I. INTRODUCTION

Estimation of signals from past observations of them corrupted by noise is a classical problem of filtering theory. The following is a standard mathematical idealization of this problem: The signal $z_\cdot$ is a measurable stochastic process with $E|z_t| < \infty$, the noise $w_\cdot$ is a Brownian motion, and the observations consist of the process

$$y_t = \int_0^t z_s ds + w_t. \tag{1}$$

Define $\hat{z}_t = E\{z_t | y_s, 0 \leqq s \leqq t\}$, the expected value of z_t given the past of the observations up to t. It can be shown[1] that if $\int_0^t z_s^2 ds < \infty$ a.s., then there is a measurable version of $\hat{z}_\cdot$ with $\int_0^t \hat{z}_s^2 ds < \infty$ a.s. The *innovations process* for this setup is defined to be

$$\nu_t = \int_0^t (z_s - \hat{z}_s) ds + w_t,$$

and it is a basic result of Frost[2] and also of Kailath[3] that, under weak conditions, $\nu_\cdot$ is itself a Wiener process with respect to the observations. Thus, (1) is equivalent to the integral equation

$$y_t = \int_0^t \hat{z}_s ds + \nu_t, \tag{2}$$

which reduces the general case (1) to that in which $z_\cdot$ is adapted to $y_\cdot$, a special property useful in questions of absolute continuity in filtering and detection.

Since $\hat{z}_\cdot$ is of necessity adapted to $y_\cdot$, Eq. (2) purports to define $y_\cdot$ in terms of $\nu_\cdot$; the *innovations problem*, first posed by Frost,[2] is precisely to determine whether it really does. Frost asked: Do the innovations contain all the information in the observations? [By (2) they do not contain more.] In the language of probability this is to ask whether the σ-algebras that the processes generate are the same up to null sets; i.e., is

$$\mathcal{Y}_0^t \triangleq \sigma\{y_s, s \leqq t\} = \sigma\{\nu_s, s \leqq t\} \triangleq \mathcal{N}_0^t \pmod{P}?$$

II. THE σ-ALGEBRAS PROBLEM IN STOCHASTIC DEs

The innovations problem is equivalent to an apparently more general problem from the theory of stochastic DEs, sometimes called the σ-algebras problem: Given a causal drift $a(s, x)$, possibly depending on the past of the function x, and a weak solution of the DE $dx_t = a(t, x)ds + dw_t$, with $w_\cdot$ a Brownian motion, and $x_\cdot$ possibly nonanticipating with respect to $dw_\cdot$, to determine whether

$$\sigma\{x_s, s \leqq t\} = \sigma\{w_s, s \leqq t\} \qquad \pmod{P}.$$

Positive answers to both problems were widely conjectured.

The innovations problem has been outstanding, in both senses of the word, since about 1968, and it has drawn the attention of communications theorists and probabilists alike. The σ-algebras problem has been current in the Soviet Union since the late 1950s; there it has been the object of great effort and a source of stimulus far in excess of its simple origins.[4] Accounts of the innovations problem and its theoretical background are in lecture notes by Meyer[1] and in a paper by Orey.[5]

It is now known that the answer to the general problem is in the negative. B. Cirel'son has given a counterexample[6,17] for the following special case (this case shows, incidentally, that the innovations and σ-algebras problems are in fact the same): Suppose that the signal $z_\cdot$ is a causal functional $a(t, y)$ of the observations; i.e., the signal is entirely determined by feedback from the observations. Then $z = \hat{z}$, $w = \nu$, and the problem reduces to asking whether the observations are "well-defined" in the strong sense of being adapted to the noise;

for in this vestigial or degenerate case, the noise is the only process left. Cirel'son's disturbing example consists of a choice of $a(\cdot, \cdot)$ for which there is just one weak solution $y_\cdot$, which is nonanticipative in that the future increments of $w_\cdot$ are independent of the past of $y_\cdot$, but which cannot be expressed as a functional of $w_\cdot$, causal or not, over any interval.

Prior to this counterexample, several cases of the problems had been settled in the affirmative. J. M. C. Clark[7] proved that if noise and signal are independent and the signal is bounded (uniformly in t and ω), then observations are adapted to innovations. The author[8] extended Clark's method and result to the case where signal and noise are independent and the signal is almost surely (a.s.) square-integrable. The case of gaussian observations turns out affirmatively: here results of Hitsuda[9] imply that $\hat{z}_\cdot$ is a linear functional of the past of $y_\cdot$ and eq. (2) is solvable by a Neumann series. Zvonkin[10] has given an affirmative answer to the σ-algebras problem for the Markov case $a(s, y) = a(y_s)$ bounded and homogeneous in time, using the associated scale function to transform the state space; this result extends to time-dependent bounded $a(s, y_s)$ satisfying Dini's condition.

It should be remarked that although the innovations and σ-algebras problems are mathematically equivalent, they arise in different contexts, involve different emphases, and can be usefully contrasted, as discussed below.

The innovations problem arose in filtering theory, and it focuses especially on the nature of the filter or operator that gives $\hat{z}_t$ as a causal functional $\alpha(t, y)$ on the past of $y_\cdot$; from this point of view, the example of Cirel'son, in which there is no real filtering going on, is a bit wide of the mark; the *real* problem is to find out enough about the filter to be able to settle whether $\sigma\{y\} = \sigma\{\nu\}$ in cases where there is a real signal (determined in part by sources other than the noise, and in part possibly by control or feedback based on the observations), which it is desired to control, transmit, filter, or detect.

The σ-algebras problem arises in stochastic functional DEs, and is therefore more general in scope, since the drift functionals considered need no longer be filters or conditional expectations like $\hat{z}_t$; the emphasis is on dynamics, causality, and nonanticipation, with no admixture of estimation. If the drift functional to be considered is a filter, it may have special properties that are useful in the investigation. (See the method of Clark.[7])

III. SUMMARY

Relevant notions from stochastic DEs are defined in Section IV: causal functionals, weak solutions, causal solutions, and nonanticipa-

tive solutions. A n.a.s. martingale-type condition for validity of the innovations conjecture is given in Section V; as an application, this condition yields (Section VI) the (known) conjecture for the case of gaussian observations. Section VIII describes some of Zvonkin's positive results for the Markov case and an extension. In Section VIII, we investigate the problem of calculating the estimate $\hat{z}_\cdot$ and give various relationships based on absolute continuity of measures. Section IX is devoted to the physically important case of signals $z_\cdot$ that solve stochastic DEs with drift based on feedback of observations; we show that if this drift is Lip in the feedback of linear growth in the signal uniformly in the observations, then observations are adapted to innovations. In Sections X and XI, finally, we show that validity of the innovations conjecture is equivalent to the causal solvability, on some probability space, of the equation $d\xi = \alpha(t, \xi)dt + dW$, with W Brownian and α the (a?) functional, such that $\hat{z}_t = \alpha(t, y)$.

IV. CAUSAL SOLUTIONS OF STOCHASTIC DEs

A measurable functional $\gamma: [0, \infty) \times C[0, \infty) \to R$ is called *causal* if for each $t \in [0, \infty)$, $x_s = y_s$ for $s \leqq t$ implies

$$\gamma(s, x) = \gamma(s, y) \qquad x, y \in C[0, \infty).$$

The idea expressed by this definition is the physical one that $\gamma(t, \cdot)$ cannot depend functionally on any more than the past of its argument up to t; thus, it has the same value at t for two functions that agree for $s \leqq t$. In spite of the presence of the word "depend" in the previous sentence, causality of a functional is expressible as a measurability property, and has no immediate relation to any probability measure.

Let α be a causal functional. A *weak* solution of the stochastic DE,

$$dx = \alpha(t, x)dt + dW, \qquad \text{W. Brownian,} \tag{3}$$

is a process $\xi_\cdot$ such that

$$(T\xi)_t = \xi_t - \int_0^t \alpha(s, \xi)ds = \nu_t$$

is a Brownian motion on its own past. If $\xi_\cdot$ is adapted to $\nu_\cdot$; i.e., if for each t, ξ_t is measurable with respect to $\sigma\{\nu_s, s \leqq t\}$, then $\xi_\cdot$ is called a *causal* solution, and there is a causal functional φ such that $\xi_t = \varphi(t, \nu)$ at each t with probability one. A solution $\xi_\cdot$ is called *nonanticipative* if (roughly) the future increments of $\nu_\cdot$ are independent of the past of $\xi_\cdot$; i.e., for each t

$$\sigma\{\nu_u - \nu_t, u \geqq t\} \perp\!\!\!\perp \sigma\{\xi_s, s \leqq t\}.$$

This is a probabilistic property, and it is equivalent to ν's being a

martingale on the larger algebras $\sigma\{\xi_s, s \leqq t\}$. It can be seen that for (3), causal $\Rightarrow$ nonanticipative, but the converse is false: it is known that there are drift functionals α for which there exist nonanticipative weak solutions, but no causal solutions.[17]

V. A SEMI-MARTINGALE CONDITION

Theorem 1: $\sigma\{\nu_s, s \leqq t\} = \sigma\{y_s, s \leqq t\}$ *(mod P) for each* $t \geqq 0$ *iff there is a* $\mathcal{Y}_0$*-adapted martingale* x_t *and a causal functional* ψ*:* $[0, \infty) \times C[0, \infty) \to R$ *such that the observations are representable (as a semi-martingale on their own past) by*

$$y_t = x_t + \int_0^t \psi(s, x)ds.$$

Proof: The hypothesis on $y_\cdot$ and the equation $dy = \hat{z}dt + d\nu$ imply that

$$x_t - \nu_t = \int_0^t [\hat{z}_s - \psi(s, x)]ds. \tag{4}$$

The innovations process is a Wiener process with respect to the observations; thus, the left side of (4) is a continuous $\mathcal{Y}_0$-martingale. Since the right side is absolutely continuous in t, it follows that both sides vanish identically, so that $x_\cdot$ and $\nu_\cdot$ are indistinguishable processes, and

$$\int_0^t \hat{z}_s ds = \int_0^t \psi(s, x)ds = \int_0^t \psi(s, \nu)ds.$$

But the right-hand side is ν-adapted because ψ is causal. The theorem follows from $dy = \hat{z}dt + d\nu$. For the converse, we argue thus: if the σ-algebras coincide, there is a causal functional φ such that $y_t = \varphi(t, \nu)$. The innovations theorem makes $\nu_\cdot$ a $\mathcal{Y}_0$-martingale with

$$y_t = \nu_t + \int_0^t \hat{z} \circ \varphi ds;$$

then, take $x = \nu$ and $\psi = \hat{z} \circ \varphi$.

VI. APPLICATION TO GAUSSIAN OBSERVATIONS

The theorem just proved affords us a simple demonstration of the validity of the innovations conjecture for gaussian observations. Suppose that the signal $z_\cdot$ is square-integrable almost surely. Then, a theorem of Kailath and Zakai[11] implies that the measure induced by $y_\cdot$ is absolutely continuous with respect to Wiener measure. The class of gaussian processes absolutely continuous with respect to Wiener measure has been characterized in a causal way by Hitsuda[9]: a process $y_\cdot$ belongs to this class iff there is a Wiener process $W_\cdot$ adapted to $y_\cdot$.

and a Volterra kernel $m(\cdot, \cdot) \in L_2[0, 1]^2$ such that

$$y_t = W_t + \int_0^t \int_0^s m(s, u) dW_u ds.$$

Thus, $W_\cdot$ is a martingale on the past of $y_\cdot$ and in Theorem 1 we can set $x = W$, $\psi(s, W) = \int_0^s m(s, u) dW_u$, to conclude that ν is W and $\hat{z}$ is ψ. Iteration of the relation between y and W gives

$$\nu_t = y_t - \int_0^t \left(\int_0^s m(s, u) dy_u - \int_0^s m(s, u) \cdot \int_0^u m(u, v) du dy_v + \cdots \right) ds,$$

so that letting

$$l(t, s) = m(t, s) - \int_0^t m(t, u) m(u, s) du + \cdots$$

be the Neumann series or the resolvent of $m(\cdot, \cdot)$, we see that

$$y_t = \nu_t + \int_0^t \int_0^s l(s, u) dy_u ds$$

$$\hat{z}_t = \int_0^t l(t, u) dy_u.$$

Thus, the map $\hat{z}$ is linear in $y_\cdot$ when $y_\cdot$ is gaussian, as was expected.

VII. RESULTS OF ZVONKIN FOR THE MARKOV CASE

For a stochastic DE of the form $dy = a(y_t)dt + dw_t$, Zvonkin[10] has shown that if $a(\cdot)$ is bounded, then there is a causal solution $y_\cdot$. His procedure[12] is to look at the scale function

$$u(y) = \int_0^y \exp - 2 \int_0^s a(s) ds dz = \int_0^y \beta(z) dz \tag{5}$$

and to note that $\sigma\{y_s, s \leqq t\} = \sigma\{u(y_s), s \leqq t\}$ because $u(\cdot)$ is monotone. Then to show that $u(y_s)$ can be got causally from $w_\cdot$, he uses Ito's rule on $z_t = u(y_t)$ to get

$$\begin{aligned} dz_t &= \beta(y_t) dy_t - \beta(y_t) a(y_t) dw_t \\ &= \beta[u^{-1}(z_t)] dw_t. \end{aligned}$$

By calculus he finds $a(\cdot)$ bounded $\Rightarrow \beta(u^{-1}) \in \text{Lip}$; hence, $z_\cdot$ is a causal functional of $w_\cdot$ and so is $y_\cdot$.

Now this argument depends in part on the fact that u satisfies $\frac{1}{2}u'' + u'a = 0$, and at once suggests extensions to the inhomogeneous case $a(t, y) = a(t, y_t)$. We give an example based on Zvonkin's paper:[10]

Theorem 2: *Suppose that for some strictly increasing function* $k(\cdot)$ *there exists a solution* $u(t, y)$ *of the Cauchy problem*

$$u(0, y) = k(y)$$
$$u_1 + \tfrac{1}{2}u_{22} + a(t, y)u_2 = \mathfrak{L}u = 0^{\dagger}$$

such that $(\log u_2)_2$ *is bounded. Then, the stochastic* DE

$$dy_t = a(t, y_t)dt + dw_t \tag{6}$$

has a causal solution.

Proof: Since $k\uparrow$, it is clear that $u_y > 0$ and that the transformation $z_t = u(t, y_t)$ is bijective. Using Ito's rule, we calculate the stochastic differential of $z_\cdot$ as

$$\begin{aligned} dz_t &= (\mathfrak{L}u)(t, y_t)dt + u_2(t, y_t)dw_t \\ &= u_2[t, u^{-1}(t, z_t)]dw_t. \end{aligned} \tag{7}$$

Now

$$\begin{aligned} \frac{\partial}{\partial z} u_2[t, u^{-1}(t, z)] &= \frac{u_{22}[t, u^{-1}(t, z)]}{u_2[t, u^{-1}(t, z)]} \\ &= (\log u_2)_2|_{y=u^{-1}(t,z)} \text{ bounded.} \end{aligned}$$

Hence, by the usual Ito's theory of stochastic DEs, the martingale eq. (7) has a unique causal solution $z_\cdot$ which is a bijection of $y_\cdot$ pointwise in time. Hence, $y_\cdot$ is a causal functional of $w_\cdot$ too. The homogeneous case follows if we take $u(t, y) \equiv$ the scale function (5).

In a similar vein we can show this result:

Theorem 3: *If* $a(\cdot, \cdot)$ *is bounded and such that*

$$\frac{\partial}{\partial t} \int_0^y a(t, z)dz$$

exists and is bounded, then (6) *has a causal solution.*

Proof: Let

$$u(t, y) = \int_0^y \exp - 2 \int_0^z a(t, x)dxdz$$

so that $u_2 > 0$, and $z_t = u(t, y_t)$ is bijective. We have

$$dz_t = u_1[t, u^{-1}(t, z_t)]dt + u_2[t, u^{-1}(t, z_t)]dw_t. \tag{8}$$

By calculus obtain formally

$$\frac{\partial}{\partial z} u_1[t, u^{-1}(t, z)] = -2a(t, z)$$

$$\frac{\partial}{\partial z} u_2[t, u^{-1}(t, z)] = -2 \frac{\partial}{\partial t} \int_0^z a(t, x)dx,$$

---

† Numerical indexes show which variable is differentiated and how many times.

both bounded by hypothesis. Hence, (8), and so (6), has a causal solution, by Ito's theory.

Note that Zvonkin's Markov case is not relevant to Kailath's innovations problem, because the filter giving $\hat{z}_t$ will almost invariably depend with advantage on the whole past of the observation process.

VIII. CALCULATION OF THE ESTIMATOR $\hat{z}$

Let (Ω, B, P) be a probability space on which are defined the signal process $z_\cdot$, the noise $w_\cdot$, the estimate $\hat{z}_\cdot$, and the innovations process $\nu_\cdot$, related by

$$y_t = \int_0^t z_s ds + w_t = \int_0^t \hat{z}_s ds + \nu_t.$$

Under some mild technical assumptions, this setup has implicit in it a rich structure that allows us to give a "formula" for $\hat{z}$, *inter alia*. To penetrate deeper into the situation, it is convenient to introduce an absolutely continuous change of measure which makes the observation process Brownian. We shall restrict attention to the interval $0 \leqq t \leqq 1$, and assume that

(i) $$\int_0^1 z_s^2 ds < \infty \quad \text{a.s.}$$

(ii) There is a system of increasing σ-algebras $\mathfrak{F}_t$, $0 \leqq t \leqq 1$, to which $z_\cdot$ and $w_\cdot$ are adapted, and $w_\cdot$ is a Wiener process with respect to $(P, \mathfrak{F}_\cdot)$.

(ii) $$E \exp\left\{ - \int_0^1 z_s dw_s - \frac{1}{2} \int_0^1 z_s^2 ds \right\} = 1.$$

Then by Girsanov's theorem,[13] the observation process $y_\cdot$ is a Wiener process on $\mathfrak{F}_\cdot$ (and thus on $\mathcal{Y}_0 = \sigma\{y_s, s \leqq \cdot\}$) under the transformed measure P_0 defined on $\mathfrak{F}_1$ by

$$\frac{dP_0}{dP} = \exp\left\{ - \int_0^1 z_s dw_s - \frac{1}{2} \int_0^1 z_s^2 ds \right\}.$$

It is convenient to use the functional notation[5]

$$q(f, g)_t = \exp\left\{ \int_0^t f_s dg_s - \frac{1}{2} \int_0^t f_s^2 ds \right\}.$$

Then $(dP_0/dP)^{-1} = q(z, y)_1 > 0$ a.s. and for $A \in \mathfrak{F}_1$

$$P(A) = \int_A q(z, y)_1 \frac{dP_0}{dP} dP, \qquad \frac{dP}{dP_0} = q(z, y)_1$$

so that $P \ll P_0$ and so $P \sim P_0$. The following formula for $\hat{z}$ is then

readily justified: with $\mathcal{Y}_0^t = \sigma\{y_s, 0 \leqq s \leqq t\}$,

$$\hat{z}_t = \frac{E_0\{z_t q(z, y)_1 | \mathcal{Y}_0^t\}}{E_0\{q(z, y)_1 | \mathcal{Y}_0^t\}}.$$

For let $A \in \mathcal{Y}_0^t$, so that

$$\begin{aligned}\int_A z_t dP &= \int_A z_t \frac{dP}{dP_0} dP_0 = \int_A E_0\{z_t q(z, y)_1 | \mathcal{Y}_0^t\} dP_0 \\ &= \int_A \frac{E_0\{z_t q(z, y)_1 | \mathcal{Y}_0^t\}}{E_0\{q(z, y)_1 | \mathcal{Y}_0^t\}} E_0\{q(z, y)_1 | \mathcal{Y}_0^t\} dP_0 \\ &= \int_A \frac{E_0\{z_t q(z, y)_1 | \mathcal{Y}_0^t\}}{E_0\{q(z, y)_1 | \mathcal{Y}_0^t\}} dP, \end{aligned} \tag{9}$$

since for $A \in \mathcal{Y}_0^t$ and a $\mathcal{Y}_0^t$-measurable function $\mathfrak{N}$ integrable

$$\int_A \mathfrak{N} \frac{dP}{dP_0} dP_0 = \int_A \mathfrak{N} E_0\left\{\frac{dP}{dP_0} | \mathcal{Y}_0^t\right\} dP_0.$$

Thus, the ratio (integrand) in eq. (9) is a version of $\hat{z}_t$. The process

$$E_0\left\{\frac{dP}{dP_0} | \mathcal{Y}_0^t\right\}$$

is a positive martingale on the past of the Brownian (under P_0) motion $y_\cdot$ and can therefore be expected to have a special form. It can in fact be shown by arguments of Shiryaev and Liptser[14] that

$$E\left\{\frac{dP_0}{dP} | \mathcal{Y}_0^t\right\} = q^{-1}(\hat{z}, y)_t.$$

From this it follows that

$$E_0\left\{\frac{dP}{dP_0} | \mathcal{Y}_0^t\right\} = q(\hat{z}, y)_t.$$

It is obvious intuitively that $q(z, y)_1$ in eq. (9) can be changed to $q(z, y)_t$: since $q(z, y)_\cdot$ is an $\mathcal{F}_\cdot$-martingale, we have a.s.

$$\begin{aligned} E_0\left\{\frac{dP}{dP_0} q^{-1}(z, y)_t | \mathcal{F}_t\right\} &\equiv 1 \\ E_0\left\{\frac{dP}{dP_0} | \mathcal{F}_t\right\} &= q(z, y)_t \\ E_0\left\{z_t \frac{dP}{dP_0} | \mathcal{F}_t\right\} &= E_0\{z_t q(z, y)_t | \mathcal{F}_t\}. \end{aligned}$$

Hence, $\mathcal{Y}_0^t \subseteq \mathcal{F}_t$ gives

$$E_0\left\{z_t \frac{dP}{dP_0} | \mathcal{Y}_0^t\right\} = E_0\{z_t q(z, y)_t | \mathcal{Y}_0^t\}, \quad \text{a.s.}$$

Thus, the filtering $\hat{z}_\cdot$ can be represented as

$$\hat{z}_t = \frac{E_0\{z_t q(z, y)_t | \mathcal{Y}_0^t\}}{q(\hat{z}, y)_t}$$
$$= \frac{d/dt\langle y, q(\hat{z}, y)\rangle_t}{q(\hat{z}, y)_t}.$$

The last equation, it can be verified, is an identity valid for any $\mathcal{Y}_0^\cdot$-adapted, a.s. square-integrable functional, not just $\hat{z}_\cdot$. Thus, the meat of the formula is the numerator, as could be expected intuitively since the denominator is basically a normalizer.

IX. SIGNALS SOLVING ITO DEs WITH DRIFT BASED ON FEEDBACK OF OBSERVATIONS

The positive results of Clark,[7] based on the assumption of independence between signal and noise, seem adequate for many practical purposes of one-way communication or detection. For the more general physical applications to estimation and control, involving feedback of observations to control the signal, it would be pleasant to be able to weaken this assumption and allow some physically reasonable dependence between signal and noise. A natural setup to investigate is a generalization of the usual Kalman filter situation, in which the signal and the observation each solves a stochastic DE, with independent driving white noises, and with the drift for the signal equation depending on the observations. Thus, we let the signal $z_\cdot$ and observation $y_\cdot$ respectively solve

$$dz_t = b(t, z, y)dt + dW_t \tag{10}$$

$$dy_t = z_t dt + dw_t. \tag{11}$$

The second equation is, of course, eq. (1) differentiated; the functional b, causal in both z and y simultaneously, represents the deterministic dynamics of a system described by $z_\cdot$ and depending on the past of both signal and observation.

As noted at the end of Section I, the only way to make headway is to find out something about the form of the filter that gives $\hat{z}_\cdot$; we shall show that in the case of eqs. (10) and (11) an analog of the Kallianpur-Striebel[15] formula for $\hat{z}$ provides enough structure on which to hang a proof similar to Clark's.[7]

Let us assume, as is physically reasonable, that $b(t, z, y)$ grows at most linearly with $\sup_{0\leq s\leq t}|z_s|$, uniformly in y. Then

$$Eq[b(W, w), W]_t q(W, w)_t = 1,$$

and we can "solve" (10) and (11) by Girsanov's theorem in such a way that the joint solution process (z_t, y_t) is absolutely continuous with respect to the two-dimensional Brownian motion, here (W_t, w_t), with derivative $q[b(W, w), W]_t q(W, w)_t$. It is then easily seen that $\hat{z}_t$ should have the form

$$\hat{z}_t = \frac{\int M(dW) q[b(W, y), W]_t q(W, y)_t W_t}{\int M(dW) q[b(W, y), W]_t q(W, y)_t} = \alpha(t, y), \tag{12}$$

where M is the Wiener measure for W alone. Verification is left to the reader; either of two more or less equivalent methods will do: direct integration over $\mathcal{Y}_0^t$ sets using the absolute continuity or introduction of P_1 by $dP_1 = q(-z, w)q[-b(z, y), W]dP$, and a use of it similar to that of P_0 in Section VIII. Note that P_1 makes (z, y) a 2-dimensional Brownian motion.

Theorem 4: *If $z_\cdot$ and $y_\cdot$ are nonanticipating solutions of eqs. (10) and (11), and there exists a constant K such that for x, ξ, and $\eta \in C[0, \infty)$*

$$|b(t, x_1, \eta)| \leqq K[1 + \sup_{0 \leqq s \leqq t} |x_1(s)|], \tag{13}$$

$$|b(t, x, \eta) - b(t, x, \xi)| \leqq K \sup_{0 \leqq s \leqq t} |y - \xi|$$

then $\sigma\{y_s, s \leqq t\} = \sigma\{\nu_s, s \leqq t\}$ (mod P).

Remark: Eq. (13) $\not\Rightarrow$ (10) and (11) have a unique causal solution. In fact, our argument will not devolve on whether eqs. (10) and (11) have a strong solution at all; the unique (in law) nonanticipative solution *is* the Girsanov solution, with derivative $q[b(W, w), W]q(W, w)$, which determines $\hat{z}$ via eq. (12).

Proof: With the explicit form eq. (12) for $\hat{z}$ available, a form of argument previously used by the author[8] (and generalized from that of Clark[7]) can be used: we exhibit a sequence of $\nu_\cdot$-adapted processes converging to $\hat{z}_\cdot$; the result then follows from eq. (2): Let

$$S(m, t) = \{\sup_{0 \leqq s \leqq t} |W_s| \leqq m\}, \quad m = 1, 2, \cdots.$$

It can be seen that the approximations

$$\hat{z}_m(t) = \frac{\int_{S(m,t)} M(dW) q[b(W, y), W]_t q(W, y)_t W_t}{\int_{S(m,t)} M(dW) q[b(W, y), W]_t q(W, y)_t} = \hat{z}_m(y)_t, \tag{14}$$

approach $\hat{z}_t$ as $m \to \infty$, and that each one is adapted to $y_\cdot$; therefore, it

is enough to prove that each one is adapted to $\nu_\cdot$ itself. Now set

$$\hat{z}_t^{m,0} \equiv 0, \qquad m = 1, 2, \cdots$$

$$y_t^{m,n} = \int_0^t \hat{z}_s^{m,n} ds + \nu_t, \qquad m \wedge n \geqq 1$$

$$\hat{z}_t^{m,n+1} = \hat{z}_m(y^{m,n})_t,$$

$$y_t^m = \int_0^t \hat{z}_m(s) ds + \nu_t,$$

and note that $d(y^{m,n} - y^m) = (\hat{z}^{m,n} - \hat{z}_m)dt$ and

$$q(f, y^{m,n})_t = q(f, y^m) \exp \int_0^t f_s(\hat{z}^{m,n} - \hat{z}_m)_s ds.$$

With $\hat{z}^{m,n} - \hat{z}_m = \psi^{m,n}$ for short, we find from eq. (14) that

$$\psi_t^{m,n+1} = \int_{S(m,t)} M(dW) W_t \left\{ \frac{q[b(W, y^{m,n}), W]_t q(W, y^{m,n})_t}{A_t^m(y^{m,n})} - \frac{q[b(W, y^m), W]_t q(W, y^m)_t}{A_t^m(y^m)} \right\},$$

where

$$A_t^m(f) = \int_{S(m,t)} M(dw) q[b(w, f), w]_t q(w, f)_t.$$

Subtracting the two fractions on the right of $\psi_t^{m,n+1}$ above, and using the further abbreviation $p(f, g)_t$ for $q[b(f, g), f]_t$, we find

$$\psi_t^{m,n+1} = \int_{S(m,t)^2} M(dW) M(dw) w_t \cdot \frac{p(w, y^m)_t q(w, y^m)_t p(W, y^{m,n})_t q(W, y^{m,n})_t - p(w, y^{m,n})_t q(w, y^{m,n})_t p(W, y^m)_t q(W, y^m)_t}{A_t^m(y^{m,n}) A_t^m(y^m)}.$$

The numerator in the integrand is just

$$p(w, y^m)_t q(w, y^m)_t p(W, y^m)_t q(W, y^m)_t \cdot \left[\exp \left\{ \int_0^t [b(W, y^{m,n}) - b(W, y^m)] dw - \frac{1}{2} \int_0^t [b^2(W, y^{m,n}) - b^2(W, y^m)] ds + \int_0^t W_s \psi_s^{m,n} ds \right\} - \exp \left\{ \int_0^t [b(w, y^{m,n}) - b(w, y^m)] dw - \frac{1}{2} \int_0^t [b^2(w, y^{m,n}) - b^2(w, y^m)] ds + \int_0^t w_s \psi_s^{m,n} ds \right\} \right],$$

so we can use the inequality $|e^A - e^B| \leqq \frac{1}{2}(e^A + e^B)|A - B|$ to find that

$$|\psi_t^{m,n+1}| \leqq \frac{M}{2} \int_{S(m,t)^2} M(dW)M(dw)$$
$$\cdot \frac{p(w, y^m)_t q(w, y^m)_t p(W, y^{m,n})_t q(W, y^{m,n})_t + p(w, y^{m,n})_t q(w, y^{m,n})_t p(W, y^m) q(W, y^m)_t}{A_t^m(y^{m,n}) A_t^m(y^m)}$$
$$\cdot \Big| \int_0^t [b(W, y^{m,n}) - b(W, y^m)]dW$$
$$- \frac{1}{2} \int_0^t [b^2(W, y^{m,n}) - b^2(W, y^m)]ds + \int_0^t W_s \psi_s^{m,n} ds$$
$$- \int_0^t [b(w, y^{m,n}) - b(w, y^m)]dw$$
$$+ \frac{1}{2} \int_0^t [b^2(w, y^{m,n}) - b^2(w, y^m)]ds - \int_0^t w_s \psi_s^{m,n} ds \Big| .$$

The Lipschitz and growth conditions on b imply that on the range of integration, with $x = W$ or w

$$|b^2(x, y^{m,n}) - b^2(x, y^m)| \leqq 2K^2(1 + m) \sup_{0 \leqq u \leqq s} \Big| \int_0^u \psi_\tau^{m,n} d\tau \Big|$$
$$\leqq 2K^2(1 + m) \int_0^s |\psi_u^{m,n}| du,$$

where we have used $d(y^{m,n} - y^m) = \psi^{m,n} dt$. Hence, with

$$\theta_{mn}(W) = \int_0^t [b(W, y^{m,n}) - b(W, y^m)]dW,$$

we find

$$|\psi_t^{m,n+1}| \leqq m^2 \int_0^t |\psi_s^{m,n}| ds + 2K^2(1 + m) \int_0^t \int_0^s |\psi_u^{m,n}| du ds$$
$$+ 2 \int_{S(m,t)} M(dW) \theta_{mn}(W) \left[\frac{p(W, y^{m,n})_t q(W, y^{m,n})_t}{A_t^m(y^{m,n})} + \frac{p(W, y^m)_t q(W, y^m)_t}{A_t^m(y^m)} \right].$$

Since θ_{mn} is a stochastic integral, Schwarz's inequality implies that

$$\int_{S(m,t)} M(dW) \theta_{mn}(W) p(W, y^{m,n})_t q(W, y^{m,n})_t$$
$$\leqq K \left[\int_0^t \left(\int_0^s |\psi_u^{m,n}| du \right)^2 ds \right]^{\frac{1}{2}}$$
$$\cdot \left[\int_{S(m,t)} M(dW) p^2(W, y^{m,n})_t q^2(W, y^{m,n})_t \right]^{\frac{1}{2}}. \quad (15)$$

To bound the second factor on the right, we use

$$q^2(f, g)_t = q(2f, g)_t \exp \int_0^t |f|^2 ds$$

and the relations

$$y_t^m = \int_0^t \hat{z}^m ds + \nu_t$$

$$\int_0^t W_s d\nu = W_t \nu_t - \int_0^t \nu_s dW$$

to find that on $S(m, t)$

$$\begin{aligned}
&p^2(W, y^m)_t q^2(W, y^m)_t \\
&\quad = q[2b(W, y^m), W]_t q(2W, y^m)_t \exp \left\{ \int_0^t b^2(W, y^m) ds + \int_0^t W_s^2 ds \right\} \\
&\quad = q[2b(W, y^m) - 2\nu, W]_t \exp \left\{ \int_0^t [b(W, y^m)_s - 2\nu_s]^2 ds \right. \\
&\qquad \left. + 2\nu_t W_t + 2 \int_0^t W_s \hat{z}_s^m ds + \int_0^t W_s^2 \right\} \\
&\qquad \leqq q[2b(W, y^m) - 2\nu, W]_t \exp \left\{ 3m^2 t + 2m|\nu_t| \right. \\
&\qquad\qquad \left. + \int_0^t [K(1 + m) + |\nu_s|]^2 ds \right\}.
\end{aligned}$$

Since the q factor on the right integrates to 1 with respect to $M(dW)$, it can be seen that the square root of

$$\int_{S(m,t)} M(dW) p^2(W, y^m)_t q^2(W, y^m)_t$$

is bounded by a t-integrable function depending on m and ν. Since $|\hat{z}^{mn}| \leqq m$, the same result holds with y^{mn} for y^m in p and q. Also, by Jensen's inequality, with $S = S(m, t)$

$$\begin{aligned}
A_t^m(y^m) &= \int_S M(dW) q[b(W, y^m), W]_t q(W, y^m)_t \\
&\geqq M\{S\} \exp \left\{ M^{-1}\{S\} \int_S \left[\int_0^t b(W, y^m) dW - \frac{1}{2} \int_0^t b^2(W, y^m) ds \right. \right. \\
&\quad \left. \left. + \int_0^t W_s \hat{z}_s^m ds + \iint_0^t W_s d\nu_s - \frac{1}{2} \int_0^t W_s^2 ds \right] \right\} \\
&\geqq M\{S\} \exp \left\{ -\tfrac{1}{2}K^2(1 + m)^2 t - \tfrac{3}{2}m^2 t - m|\nu_t| \right. \\
&\qquad \left. \cdot \int_S M(dW) \int_0^t [b(W, y^m)_s - \nu_s] dW_s \right\}.
\end{aligned}$$

If $T = \inf s: |W_s| = m$, the integral in the exponent is bounded by

the square root of

$$\int M(dW) \int_0^t \chi_{T>s}[b(W, y^m) - \nu]^2 ds \leqq \int_0^t [K(1 + m) + |\nu_s|]^2 ds.$$

The same argument applies to $A_t^m(y^{m,n})$, since $|\hat{z}^{m,n}| \leqq m$.

It follows that

$$|\psi_t^{m,n+1}| \leqq m^2 \int_0^t |\psi_s^{m,n}| ds + 2K^2(1 + m) \int_0^t \int_0^s |\psi_u^{m,n}| du ds + F(t, m, \nu) \left[\int_0^t \left(\int_0^s |\psi_u^{m,n}| du \right)^2 ds \right]^{\frac{1}{2}},$$

where F is a t-integrable function depending only on m and ν. Thus, by arguments similar to those for Gronwall's inequality, it is seen that $\psi_t^{m,n}$ converge to zero. It follows that $\hat{z}_{m_\cdot}$ are $\nu_\cdot$-adapted, and so is $y_\cdot$ by eq. (2).

Remark: The reader is invited to speculate on how the above proof would be carried out if it were postulated that the dependence of $b(t, z, y)$ on y in eq. (10) came only through the estimate $\hat{z}$, as, for example, $b(t, z, y) = \beta(t, z, \hat{z})$. In this case, there is no longer a formula for $\hat{z}$, but only a functional equation.

X. DISCUSSION OF THE GENERAL PROBLEM

There is a general result of measure theory to the effect that a function x is measurable on the σ-algebra induced by another function y, iff it is representable by an explicit composition with y, that is, as a function of y: $x = \varphi \circ y$. This might be called the "explicit" function theorem, as opposed to the "implicit" function theorems, like Filippov's lemma. For here x and y are given and φ is to be found, while in Filippov's lemma x and φ are given and y is to be found. We suggest that the σ-algebras and innovations problems are very close in spirit to the ideas around the explicit function theorem. This suggestion only provides what we think is a *hilfsaussichtspunkt;* without more information (about $\hat{z}$ or $a(\cdot, \cdot)$, and more insight and work, it does not help settle any particular case. What it helps do, though, is place the problems and concepts into the general framework of stochastic equations, especially into the circle of ideas developed by M. P. Yershov.[16] See also Ref. 18.

Our final results on the innovations problem will clarify the role of the integral equation relating $y_\cdot$ and $\nu_\cdot$. Thus, for each t, $\hat{z}_t$ is measurable with respect to $\sigma\{y_s, s \leqq t\}$; hence, there is a causal functional α such that $\hat{z}_t = \alpha(t, y)$, or more precisely, such that some version of $\hat{z}_t$ is indistinguishable from $\alpha(t, y)$; then the relation between $y_\cdot$ and $\nu_\cdot$ is

essentially

$$y_t = \int_0^t \alpha(s, y)ds + \nu_t. \tag{16}$$

Thus, it is apparent intuitively, and can be proved, that if $y_\cdot$ is adapted to $\nu_\cdot$, then there is a causal solution to (4), namely $y_\cdot$ itself, expressible as $\varphi(\cdot, \nu)$ with φ causal. What we shall show is the converse, that causal solvability somewhere of the stochastic DE (16) implies a positive answer to the Frost-Kailath conjecture. In particular, we shall prove that $\sigma\{y_s, s \leqq t\} = \sigma\{\nu_s, s \leqq t\}$ (mod P) for each t iff on some probability space there is a Brownian motion $W_\cdot$ and a causal solution ξ of

$$\xi_t = \int_0^t \alpha(s, \xi)ds + W_t, \tag{17}$$

which induces the same measure as $y_\cdot$ does.

This result gives a necessary and sufficient condition for Frost and Kailath's innovations conjecture to hold, and it embodies the sense in which the innovations problem resembles the explicit function theorem. The direct part or necessity is obvious. For the sufficiency, we argue that if eq. (17) has a causal solution on some probability space, then it is expressible as a causal functional φ of a Brownian motion defined there. This functional can be "exported"; i.e., it can be applied to any other Brownian motion on any other space to give a causal solution. In particular, applying it to the innovations process $\nu_\cdot$ gives a causal solution $(\varphi\nu)_t = \varphi(t, \nu)$, which under weak conditions induces the same measure as $y_\cdot$ does. This, along with the properties

$$(\varphi\nu)_t - \int_0^t \alpha(s, \varphi\nu)ds \triangleq (T\varphi\nu)_t = \nu_t, \quad \text{a.s.} \tag{18}$$

$$\sigma\{\nu_s, s \leqq t\} \subseteq \sigma\{y_s, s \leqq t\}, \tag{19}$$

allows us to prove the basic property that for any integrable causal functional $\beta(t, y)$

$$E\{\beta(t, y) \mid \nu_s, s \leqq t\} = \beta(t, \varphi\nu) \quad \text{a.s.}$$

This result can be applied in several ways to give the desired final result that $y_\cdot$ and $\varphi\nu_\cdot$ are modifications of each other. We describe two—one a digressive application of martingales and the other short and direct.

XI. MARTINGALE ARGUMENTS USING P_0

In this section, we use some of the properties of the measure P_0 defined in Section VIII. We assume that α is a causal functional such

that $\hat{z}_t = \alpha(t, y)$; i.e., really such that $\hat{z}_t$ and $\alpha(t, y)$ are indistinguishable processes. We let $\mathcal{C}_t$ be the Borel σ-subalgebra of $C[0, \infty)$ generated by sets of the form $\{x : x_s \in B\}$, $s \leqq t$, B Borel, and $\mathfrak{N}_0^t$ is $\sigma\{\nu_s, 0 \leqq s \leqq t\}$, the σ-algebra generated by the innovations.

Theorem 5: *If there is, on some probability space, a Brownian motion W and a causal solution ξ of*

$$d\xi = \alpha(t, \xi)ds + W_t$$

given by a causal functional φ as $\xi_t = \varphi(t, W)$, and if $\varphi\nu$ and y are identical in law, then they are modifications of each other, and $\mathfrak{N}_0^t = \mathcal{Y}_0^t$ (mod P).

The proof is the sequence of lemmas which follow.

Lemma 1: $E\{(dP_0/dP) \mid \mathfrak{N}_0^t\} = q^{-1}(\alpha\varphi\nu, \varphi\nu)_t$.

Proof: Let $A \in \mathfrak{N}_0^t$, so that by the integral equation, A differs from a set of the form $\{Ty \in B\}$, $B \in \mathcal{C}_t$, by at most a null set. Then,

$$\int_A dP_0 \int E\left\{\frac{dP_0}{dP} \mid \mathcal{Y}_0^t\right\} dP = \int_{\nu \in T^{-1}B} q^{-1}(\hat{z}, y)_t dP$$

$$= \int_{\varphi\nu \in T^{-1}B} q^{-1}(\alpha\varphi\nu, \varphi\nu)_t dP = \int_{\nu \in B} q^{-1}(\alpha\varphi\nu, \varphi\nu) dP.$$

Thus, $q^{-1}(\alpha\varphi\nu, \varphi\nu)_t$ is measurable on $\mathfrak{N}_0^t$ and has the same integrals over $\mathfrak{N}_0^t$ sets as dP_0/dP; thus, it is a version of $E\{(dP_0/dP) \mid \mathfrak{N}_0^t\}$.

Lemma 2: *$\varphi\nu_t$ is a $\mathfrak{N}_0^t$-martingale under P_0.*

Proof: $y_\cdot$ is a (Brownian) martingale under P_0; since $\mathfrak{N}_0^t \subseteq \mathcal{Y}_0^t$, then

$$\int_A y_t dP_0 = \int_A y_s dP_0 \quad \text{if} \quad A \in \mathfrak{N}_0^s \quad \text{and} \quad s < t.$$

For $A \in \mathfrak{N}_0^s$, eq. (2) implies that there exists $B \in \mathcal{C}_s$ with $A = \{Ty \in B\}$. Since $y \sim \varphi\nu$ in law, there follows

$$\int_A y_t dP_0 = \int_{Ty \in B} y_t q^{-1}(z, y) = \int_{Ty \in B} y_t E\{q^{-1}(z, y)_t \mid \mathcal{Y}_0^t\} dP$$

$$= \int_{Ty \in B} y_t q^{-1}(\hat{z}, y)_t dP = \int_{T\varphi\nu \in B} (\varphi\nu)_t q^{-1}(\alpha\varphi\nu, \varphi\nu)_t dP$$

$$= \int_{\nu \in B} (\varphi\nu)_t E\left\{\frac{dP_0}{dP} \mid \mathfrak{N}_0^t\right\} dP = \int_A (\varphi\nu)_t dP_0.$$

Similarly, for $s < t$ and $A \in \mathfrak{N}_0^s$,

$$\int_A y_s dP_0 = \int_A (\varphi\nu)_s dP_0.$$

Hence, $A \in \mathfrak{N}_0^s$ implies $\int_A [\varphi\nu_t - \varphi\nu_s]dP_0 = 0$, and so $\varphi\nu_\cdot$ is a $(\mathfrak{N}_0^\cdot, P_0)$-martingale, being adapted to $\mathfrak{N}_0^\cdot$.

Lemma 3: $E_0\{y_t | \mathfrak{N}_0^t\} = \varphi\nu_t$ *a.s.*

Proof: This is shown in the same way as Lemmas 1 and 2, by integrating over $A \in \mathfrak{N}_0^t$, and using the adaptedness of ν to y, and the property $T\varphi\nu = \nu$ a.s.

Lemma 4: $\varphi\nu_\cdot$ *is a Brownian motion under* $(P_0, \mathfrak{N}_0^\cdot)$.

Proof: Let $\Delta_s = \hat{z}_s - \alpha(s, \varphi\nu)$

$$y_t - \varphi\nu_t = \int_0^t \Delta_s ds$$

$$(y_t - \varphi\nu_t)^2 = 2\int_0^t \Delta_s \int_0^s \Delta_u du ds.$$

However, since $y_\cdot$ and $\varphi\nu_\cdot$ are P_0-martingales on $\mathcal{Y}_0^\cdot$ and $\mathfrak{N}_0^\cdot$, respectively, the change of variables formula applied to each separately gives

$$y_t^2 = 2\int_0^t y_s dy_s + t \tag{20}$$

$$\varphi\nu_t^2 = 2\int_0^t \varphi\nu_s d\varphi\nu_s + \langle\varphi\nu\rangle_t. \tag{21}$$

Also

$$y_t\varphi\nu_t = y_t^2 - y_t \int_0^t \Delta_s ds.$$

The right-hand side is a product of semi-martingales on $\mathcal{Y}_0^\cdot$, and change of variables gives

$$y_t\varphi\nu_t = 2\int_0^t y_s dy_s + t - \int_0^t \Delta_s dy_s - \int_0^t y_s\Delta_s ds.$$

Using eqs. (20) and (21), we find that

$$(y_t - \varphi\nu_t)^2 = \langle\varphi\nu\rangle_t - t + 2\int_0^t \int_0^s \Delta du ds$$

$$- 2\int_0^t \left[y_s - \int_0^s \Delta du - \varphi\nu_s \right] dy_s$$

$$\langle\varphi\nu\rangle_t = t.$$

Thus, $\varphi\nu_\cdot$ is a continuous martingale with quadratic variation t, and so a Brownian motion, on $(P_0, \mathfrak{N}_0^\cdot)$.

Lemma 5: $E_0(y_t - \varphi\nu_t)^2 = 0$.

Proof: The processes $y_\cdot$ and $\varphi v_\cdot$ are Brownian under P_0 with respect to $\mathcal{Y}_0^\cdot$ and $\mathfrak{N}_0^\cdot$, respectively, so $E_0 y_t^2 = E_0\varphi\nu_t^2 = t$. Thus, by Lemma 3

$$
\begin{aligned}
E_0(y_t - \varphi\nu_t)^2 &= 2(t - E_0 y_t \varphi\nu_t) \\
&= 2(t - E_0 E_0\{y_t \mid \mathfrak{N}_0'\}\varphi\nu_t) \\
&= 2(t - E\langle\varphi\nu\rangle_t) \\
&= 0.
\end{aligned}
$$

The indicated expectation exists because both $y_\cdot$ and $\varphi\nu_\cdot$ are Brownian under P_0, on respective algebras $\mathfrak{Y}_0$ and $\mathfrak{N}_0$. This lemma shows that y and $\varphi\nu$ are modifications of each other under P_0 (and so under P), and completes the proof of Theorem 5.

XII. DIRECT PROOF OF THEOREM 5

It is possible to give a short proof of Theorem 5 not depending on the auxiliary measure P_0 or the representation for $\hat{z}$ given in Section VIII. This proof depends only on eqs. (18) and (19), the causality of φ, and the fact that $y \sim \varphi\nu$ in law; otherwise, it is just an exercise in integration.

By hypothesis there exists a causal functional φ, such that $T\varphi x = x$ for almost all x with respect to Wiener measure. Thus, the process $(\varphi\nu)_t = \varphi(t, \nu)$ (defined on the same probability space as $y_\cdot$ and $\nu_\cdot$) is identical in law to $y_\cdot$ such that $T\varphi\nu = \nu$ with probability one. Let β be a causal functional such that $E|\beta(t, y)| < \infty$ for each t. The next step is to prove that

$$
E\{\beta(t, y) \mid \nu_s, 0 \leqq s \leqq t\} = \beta(t, \varphi\nu), \quad \text{a.s.}
$$

Let then $A \in \sigma\{\nu_s, 0 \leqq s \leqq t\}$. A has the form $\{\omega: \nu \in B\}$ with B a Borel set of $C[0, t]$, so by the integral equation it differs from $\{\omega: y \in T^{-1}B\}$ by at most a null set. Then, since $\varphi\nu$ and y are identical in law, and $\varphi \subseteq T^{-1}$ on a set of Wiener measure one, we find

$$
\begin{aligned}
\int_A \beta(t, y)dP &= \int_{\{\nu \in T^{-1}B\}} \beta(t, y)dP = \int_{\{\varphi\nu \in T^{-1}B\}} \beta(t, \varphi\nu)dP \\
&= \int_{\{T\varphi\nu \in B\}} \beta(t, \varphi\nu)dP = \int_{\{\nu \in B\}} \beta(t, \varphi\nu)dP \\
&= \int_A \beta(t, \varphi\nu)dP.
\end{aligned}
$$

Thus, $\beta(t, \varphi\nu)$ has the same integrals as $\beta(t, y)$ over sets defined by $\nu_\cdot$ over $[0, t]$, and (since φ is causal) is measurable on $\sigma\{\nu_s, 0 \leqq s \leqq t\}$. Hence, it is a version of $E\{\beta(t, y) \mid \nu_s, 0 \leqq s \leqq t\}$. To complete the proof, let $\beta(t, x) = \alpha^+(t, x)^{\frac{1}{2}}$, where $a^+ = \max\{0, a\}$, to find, since $y \sim \varphi\nu$ in law, that

$$
\begin{aligned}
&E|\alpha^+(t, y)^{\frac{1}{2}} - \alpha^+(t, \varphi\nu)^{\frac{1}{2}}|^2 \\
&\quad = 2E\alpha^+(t, y) - 2E\alpha^+(t, \varphi\nu)^{\frac{1}{2}} E\{\alpha^+(t, y)^{\frac{1}{2}} \mid \nu_s, 0 \leqq s \leqq t\} = 0.
\end{aligned}
$$

Similarly, $E|\alpha^-(t, y)^{\frac{1}{2}} - \alpha^-(t, \varphi\nu)^{\frac{1}{2}}|^2 = 0$. Hence,

$$\alpha(\cdot, y) = \alpha(\cdot, \varphi\nu) \quad \text{a.s.} \quad \lambda \times P \quad (\lambda = \text{Lebesgue measure}),$$

so that for each t, by the integral equations,

$$y_t - (\varphi\nu)_t = \int_0^t [\alpha(s, y) - \alpha(s, \varphi\nu)]ds = 0 \quad \text{a.s.}$$

Since φ is causal, it follows that y_t is equal almost surely to a function measurable on $\sigma\{\nu_s, s \leqq t\}$. Since this is true for each t, it follows that for each t the algebras $\sigma\{\nu_s, s \leqq t\}$ and $\sigma\{y_s, s \leqq t\}$ are equal (mod P).

Remark 1: Since $\int_0^t \hat{z}^2 ds < \infty$ a.s., then if also

$$\int_0^t \alpha(s, \varphi\nu)^2 ds < \infty \quad \text{a.s.},$$

a theorem of Kailath and Zakai will imply that the respective measures induced by y and $\varphi\nu$ are each absolutely continuous with respect to Wiener measure with the same Radon–Nikodým derivative $q[\alpha(x), x]$. Hence, $y \sim \varphi\nu$ in law, as desired for the hypothesis of Theorem 5. Thus, the condition that y and $\varphi\nu$ induce the same measure is easily met, in comparison with the difficulty of finding a causal solution.

Remark 2: The condition in Theorem 5 that ξ be causal can be replaced, if we are content to work only over a finite interval $[0, T]$, by the conditions that ξ be a strong solution over $[0, T]$ in the sense of Ref. 16, and that it be nonanticipative. For it has been remarked by Yershov[6] that a strong (over $[0, T]$) nonanticipative solution is necessarily causal.

XIII. ACKNOWLEDGMENTS

The author is indebted to P. Frost, T. T. Kadota, T. Kailath, H. P. McKean, Jr., L. A. Shepp, and M. P. Yershov for useful discussions regarding the innovations and σ-algebras problems, and to the manuscript reviewer for several valuable comments and suggestions.

REFERENCES

1. P. A. Meyer, "Sur un problème de filtration, Seminaire de Probabilités VII," Springer Lecture Notes 321 (1973), pp. 223–247.
2. P. Frost, "Estimation in Continuous-Time Nonlinear Systems," dissertation, Stanford University, Stanford, Calif., June 1968.
3. T. Kailath, "Some Extensions of the Innovations Theorem," B.S.T.J., *50* (April 1971), pp. 1487–1494.
4. Y. Rozanov, personal communication.
5. S. Orey, "Radon-Nikodým Derivatives of Probability Measures: Martingale Methods." Notes from lectures at Tokyo University of Education, Spring 1974.
6. M. P. Yershov, personal communication.

7. J. M. C. Clark, "Conditions for the One-to-One Correspondence Between an Observation Process and Its Innovation." Tech. Report 1 (1969), Imperial College, London, England.
8. V. E. Beneš, "Extension of Clark's Innovations Equivalence Theorem to the Case of Signal z Independent of Noise, with $\int_0^t z_s^2 ds < \infty$ a.s.," unpublished work.
9. M. Hitsuda, "Representation of Gaussian Processes Equivalent to Wiener Process," Osaka J. Math., *5*, No. 2 (December 1968), pp. 299–312.
10. A. K. Zvonkin, "Transformation of the Phase Space of a Diffusion Process, Annihilating the Drift" (in Russian), Matematicheskii Sbornik, *93*, No. 1 (January 1974), pp. 129–149.
11. T. Kailath and M. Zakai, "Absolute Continuity and Randon-Nikodým Derivatives for Certain Measures Relative to Wiener Measure," Ann. Math. Stat., *42* (February 1971), pp. 130–140.
12. S. Watanabe, personal communication.
13. Cf. e.g. Orey, loc. cit., p. 7, Theorem 1.
14. R. Sh. Liptser and A. N. Shiryaev, "Statistics of Random Processes" (in Russian), Izdat, "Nauka," Moscow, 1974.
15. G. Kallianpur and C. Striebel, "Estimation of Stochastic Processes: Arbitrary System Processes With Additive White Noise Errors," Ann. Math. Stat., *39* (June 1968), pp. 785–801.
16. M. P. Yershov, "Extension of measures and stochastic equations" (in Russian), Teoriya Veroiatnostei i ee Prim., *19*, No. 3 (July, August, September 1974), pp. 457–471.
17. B. S. Cirel'son, "An Example of a Stochastic Differential Equation Not Possessing a Strong Solution" (in Russian), Teoriya Veroiatnostei i ee Prim., *20* (March–April 1975), pp. 427–430.
18. V. E. Beneš, "Weak and Strong Solutions for Stochastic Equations," unpublished work.

Contributors to This Issue

Václav E. Beneš, A.B., 1950, Harvard College; M.A. and Ph.D., 1953, Princeton University; Bell Laboratories, 1953—. Mr. Beneš has pursued mathematical research on traffic theory, stochastic processes, frequency modulation, combinatorics, servomechanisms, and stochastic control. In 1959–60, he was visiting lecturer in mathematics at Dartmouth College. In 1971, he taught stochastic processes at SUNY Buffalo, and from 1971–72, he was Visiting MacKay Lecturer in electrical engineering at the University of California in Berkeley. He is the author of two books in his field. Member, American Mathematical Society, Association for Symbolic Logic, Institute of Mathematical Statistics, SIAM, Mathematical Association of America, Mind Association, IEEE.

William E. Bracker, B.A. (Applied Physics and Information Science), University of California (San Diego); M.S. (Computer Science), Purdue University; Bell Laboratories, 1972—. Mr. Bracker has worked on the development of store-and-forward message systems, communications processors, and data communications. He is currently teaching as Visiting Professor of Electrical Engineering at the Tuskegee Institute.

Richard W. Dixon, A.B. 1958, Harvard College; M.A., 1960, and Ph.D., 1964, Harvard University; Bell Laboratories, 1965—. Mr. Dixon was initially concerned with the interaction of light and elastic waves in solids and liquids and with the development of acoustic light modulators. From 1968 to 1972, he supervised a group responsible for developing semiconductor light-emitting-diode devices. Since 1972, he has been a supervisor in the Gallium Arsenide Laser Department with responsibility for device aspects of gallium arsenide communications laser development. Member, American Physical Society, American Association for the Advancement of Science; Senior Member, IEEE.

D. Gloge, Dipl. Ing., 1961, Dr. Ing., 1964, Technical University of Braunschweig, Germany; Bell Laboratories, 1965—. Mr. Gloge is Research Head, Optical Systems Department. He has worked

on the design and testing of various optical transmission media. He is presently engaged in systems studies related to optical fiber telecommunications.

Douglas W. Hill, B.S., 1964, California Institute of Technology; M.S. (E.E.), 1965, Stanford University; Ph.D. (Mathematics), 1973, University of New Mexico; U. S. Air Force, 1965–1969; Bell Laboratories 1973—. Mr. Hill has worked on methods for evaluating the statistical accuracy of traffic-engineering procedures. He is currently developing new methods for trunk network administration. Member, SIAM, IMS, IEEE.

Roy Stephen Krupp, S.B., (Mathematics, Physics), 1960, Massachusetts Institute of Technology; M.I.T. Aerophysics Laboratory, 1960–65; S.M., 1967 and Ph.D., 1970 (Aeronautics and Astronautics), Massachusetts Institute of Technology; Bell Laboratories, 1970—. A member of the Toll Switching Systems Studies Department, Mr. Krupp has worked at modeling the toll network and on studies of time-division switching networks. His general interests include combinatorics, fluid mechanics, and various branches of applied mathematics.

Paul M. Lapsa, B.S. (EE), 1968, Carnegie-Mellon University; M.S. (EE), 1972, University of Minnesota; Detroit Edison Company, 1968–1970; Bell Laboratories, 1972—. Mr. Lapsa has been engaged in fundamental electromagnetic interference studies and is currently working on topics in loop transmission objectives for the Customer Services Studies Group. Member, Tau Beta Pi.

Dietrich Marcuse, Diplom Vorpruefung, 1952, Dipl. Phys., 1954, Berlin Free University; D.E.E., 1962, Technische Hochschule, Karlsruhe, Germany; Siemens and Halske (Germany), 1954–1957; Bell Laboratories, 1957—. At Siemens and Halske, Mr. Marcuse was engaged in transmission research and studying coaxial cable and circular waveguide transmission. At Bell Laboratories, he has been engaged in studies of circular electric waveguides and work on gaseous masers. He spent one year (1966–1967) on leave of absence from Bell Laboratories at the University of Utah. He is presently working on the transmission aspect of a light communications system. Mr. Marcuse is the author of three books. Fellow, IEEE; member, Optical Society of America.

Calvin M. Miller, BSEE, 1963, North Carolina State University; MSE, 1966, Akron University; Bell Laboratories, 1967—. Mr. Miller has developed equipment and methods for transmission line characterization. His present interests are in the area of fiber optics as a practical transmission medium. Member, Eta Kappa Nu, OSA.

Scotty R. Neal, B.A. (Mathematics), 1961, M.A. (Mathematics), 1963, and Ph.D. (Mathematics), 1965, University of California, Riverside; Research Mathematician, Naval Weapons Center, China Lake, California, 1964–1967; Bell Laboratories 1967—. Since coming to Bell Laboratories, Mr. Neal has been primarily concerned with the analysis of various aspects of telephone traffic systems. He has also worked on applications of optimal linear estimation theory and aspects of communication theory. Member, American Mathematical Society.

S. D. Personick, B.E.E., 1967, City College of New York; S. M., 1968, E.E., 1969, and Sc.D., 1969, Massachusetts Institute of Technology; Bell Laboratories, 1967—. Mr. Personick is engaged in studies of optical communications systems. He is currently supervisor of the fiberguide systems characterization group.

Edward R. Sears, B.S. (Mathematics), 1958, Saint Peter's College; M.S. (Computer Science), 1969, Stevens Institute of Technology; Bell Laboratories, 1965—. Mr. Sears has worked on the design and development of support software for the SAFEGUARD Meck Test System. He is currently engaged in communications software design, development, and maintenance for the BISCOM project.

Abstracts of Papers by Bell System Authors Published in Other Journals

CHEMISTRY

Analysis of the Air-Formed Oxide Film on a Series of Iron-Chromium Alloys by Ion-Scattering Spectrometry. R. P. Frankenthal and D. L. Malm, J. Electrochem. Soc., *123* (February 1976), pp. 186–191. Depth profiles were obtained for Fe-Cr alloys (5–25% Cr). Using suitable standards, atomic composition ratios were calculated as a function of depth. From variations of Cr/Fe with depth and with alloy composition, it is speculated that the distribution and bonding of cations differentiates stainless from non-stainless alloys or steels.

Electroetching of Platinum in the Titanium-Platinum-Gold Metallization on Silicon Integrated Circuits. R. P. Frankenthal and D. H. Eaton, J. Electrochem. Soc., *123* (May 1976), pp. 703–706. The periodically varying potential, which is applied to metallizations in 5 *M* HCl, was designed to overcome problems of platinum passivation and relatively high metallization resistances. The resolution of etched patterns is good using positive or negative photoresists. The process is applicable to etching of other metallizations on high-resistance substrates.

Kinetics of the Thermal Decomposition of $CaCO_3$ in CO_2 and Some Observations on the Kinetic Compensation Effect. P. K. Gallagher and D. W. Johnson, Jr., Thermochim Acta, *14* (March 1976), pp. 255–261. Dynamic and isothermal kinetic studies were made of the thermal decomposition of $CaCO_3$ in CO_2 atmosphere. Variations of activation energy with sample size and heating rate suggest thermal transport is rate determining. The linear relationship between activation energy and the log of the preexponential term is discussed.

Mechanism of Oxidation at a Copper-Polyethylene Interface. II. Penetration of Copper Ions in the Polyethylene Matrix. D. L. Allara, C. W. White, R. L. Meek, and T. H. Briggs, J. Polym. Sci.: Part A-1, Polym. Chem., *14*, No. 1 (January 1976), pp. 93–104. Two surface analysis techniques (Rutherford backscattering and surface composition by analysis of neutral and ion impact radiation) have been applied to the study of interfacial copper transport in the oxidation of polyethylene films over copper surfaces. The results clarify the roles of heterogeneous and homogeneous catalytic processes.

On Passivity of Iron and Its Alloys. R. P. Frankenthal, Boshoku Gijutsu, *24* (October 1975), pp. 537–545. This review assesses the current state of understanding of passivity of iron and its alloys, defines the areas of agreement and disagreement in the field, and poses the questions that must be answered to further our understanding.

Picosecond Recovery Dynamics of Malachite Green. E. P. Ippen, C. V. Shank, and A. Bergman, Chem. Phys. Lett., *38*, No. 3 (March 15, 1976), pp. 611–614. Using subpicosecond pulses from a mode-locked cw dye laser, we have studied ultrafast absorption recovery in the triphenylmethane dye malachite green after excitation to the first singlet. In methanol an exponential time constant of 2.1 ps is measured. As solvent viscosity is increased, recovery becomes slower and a two-component relaxation is evident.

COMPUTING

On the Sethi-Ullman Algorithm. S. Chen, Inter. J. Comp. Math., *5* (1975), pp. 37–55. A directed acyclic graph (dag) can be used to represent an arithmetic expression consisting of sequences of binary operations on arguments. The Sethi-Ullman algo-

rithm generates optimal object code for a machine with $N \geq 1$ registers and unlimited memory capacity when the dag is a binary tree. We define a subclass of dags, the 1-load binary dags, employing a tree-like grammar, and modify the Sethi-Ullman algorithm to include this subclass when $N = 2$ registers. The proof of optimality relies on the use of syntax directed translation schemas.

ELECTRICAL AND ELECTRONIC ENGINEERING

Asymptotic Theory of Scattering by a Rough Surface Progressing Over an Inhomogeneous Ocean. F. M. Labianca and E. Y. Harper, J. Acoust. Soc. Amer., *59* (April 1976), pp. 799–812. A general asymptotic theory of scattering by a moving rough surface is presented. The theory is valid for a slowly varying refractive index, and for ocean-surface wave heights that are small compared with the acoustic wavelength and the ocean-surface correlation length. In contrast with the Kirchhoff or physical optics approximation, this theory is valid when the acoustic wavelength and ocean-surface correlation length are of the same order.

Differential Addressing of Clusters of Changed Picture Elements for Interframe Coding of Videotelephone Signals. B. G. Haskell, IEEE Trans. Commun., *24* (January 1976), pp. 140–144. In a conditional replenishment coder for videotelephony only those picture elements (pels) which have changed significantly since the previous frame are transmitted.

Increased addressing efficiency for videotelephony results if clusters or changed pels are positioned not with respect to the beginning of the line, but with respect to another cluster in the previous line or previous frame which has already been transmitted. Results are given of computer simulations using digitally stored videotelephone signals which were carried out to evaluate such differential schemes.

Efficient, Lattice-Matched, Double-Heterostructure LED's at 1.1 μm from $Ga_xIn_{1-x}As_yP_{1-y}$. T. P. Pearsall, B. I. Miller, R. J. Capik, and K. J. Bachmann, Appl. Phys. Lett., *28* (May 1, 1976), pp. 499–501. The growth and operation of lattice-matched, double-heterostructure, $InP/Ga_{0.17}In_{0.83}As_{0.34}P_{0.66}/InP$ light-emitting diodes is reported. These diodes have an emission wavelength of 1.1 μm and quantum efficiencies of 4 percent.

Elastically Enhanced Nonradiative Recombination at $Al_xGa_{1-x}As$-GaAs Heterointerface. W. D. Johnston, Jr. and R. A. Logan, Appl. Phys. Lett., *28* (February 1, 1976), pp. 140–142. In the presence of an elastic strain gradient of order 10^{-5} μm^{-1}, the nonradiative recombination rate at an (LPE) $Al_xGa_{1-x}As$-GaAs heterointerface is observed to increase, reversibly, by as much as 100-fold.

Hopping Conductivity in C-Implanted Amorphous Diamond, or How to Ruin a Perfectly Good Diamond. J. J. Hauser and J. R. Patel, Solid State Commun. *18*, No. 7 (1976), pp. 789–790. The electrical properties of amorphous diamond layers produced by C implantation are similar to those of deposited amorphous carbon films. This suggests that amorphous C consists of a mixture of diamond and graphite bonds irrespective of the preparation method.

Low Frequency Transfer Efficience of *E*-Beam Fabricated Conductivity Connected Charge-Coupled Device. R. H. Krambeck, T. F. Retajczyk, and L. D. Yau, IEEE J. Solid-State Circuits, *SC-11* (February 1976), pp. 171–180. Theoretical calculations are made of low-frequency transfer inefficiency for the conductivity connected, charge-coupled device (C4D). The fabrication and testing of C4Ds with barrier lengths in the range 1.75 μm to 5 μm are described, and the measured transfer inefficiencies compare well with theoretical predictions.

Power Spectra Obtained From Exponentially Increasing Spacings of Sampling Positions. H. D. Helms, IEEE Trans. Acoust. Speech Signal Process, *ASSP-24* (February 1976), pp. 63–71. An estimate of the spectrum is based on the Laplace transform which is approximated at exponentially spaced samples and analysis frequencies. The numbers of samples and computations required for exponential spacing of samples and frequencies generally are less than those required for equidistant spacing.

Preparation of Thin Windows in Silicon Masks for X-Ray Lithography. C. J. Schmidt, P. V. Lenzo, and E. G. Spencer, J. Appl. Phys., *46* (September 1975), pp. 4080–4082. Thin Si windows approximately 1–4 cm in diameter and 1–5 μm thick are made for soft x-ray lithography using a rapid chemical etch process. Procedures are uncritical and lend themselves to semiautomated operation. Yield for the etching process alone is close to 100 percent.

Timing Recovery in Digital Synchronous Data Receivers. K. H. Mueller and M. Müller, IEEE Trans. Commun., *COM-24* (May 1976), pp. 516–531. A new class of fast-converging timing recovery methods for synchronous digital data receivers is investigated. Starting with a worst-case timing offset, convergence with random binary data will typically occur within 10–20 symbols. The input signal is sampled at the baud rate; these samples are then processed to derive a suitable control signal to adjust the timing phase. A general method is outlined to obtain near-minimum-variance estimates of the timing offset with respect to a given steady-state sampling criterion.

Wide-Band Partial Discharge Detector. E. A. Franke and E. Czekaj, IEEE Trans. Elec. Insul., *EI-10* (December 1975), pp. 112–6. A wideband (30 MHz) peak-voltage detector has been constructed for measuring partial discharges from high-voltage, power-separation filters. An inexpensive, low-resolution, amplitude-distribution analyzer can be assembled by combining several detectors for the special requirements of high-voltage dc laboratory investigations.

MATERIALS SCIENCE

Mechanical Properties at Elevated Temperature of CuBath* Electroplated Copper for Multilayer Boards. A. Fox, J. Test. Eval., *4*, No. 1 (January 1976), pp. 74–84. The mechanical properties of CuBath* electroplated copper, including creep, stress-relaxation, monotonic tensile properties, and cyclic strain ratcheting were studied as a function of temperature and plating thickness to provide design information as to the material response of PTHs in MLBs during differential thermal expansion and contraction. * Sel Rex Company, the Division of Oxy Metal Finishing Corporation.

PHYSICS

Combined Radiation and Developing Laminar Free Convection Between Vertical Flat Plates With Asymmetric Heating. J. R. Carpenter, D. G. Briggs, and V. Sernas, J. Heat Transf., *98* (February 1976), pp. 95–107. A numerical investigation of the interaction of radiation with developing laminar free convection in vertical parallel plate channels with asymmetric heating is presented. Radiation to the inlet-exit and the cooler opposing entrance wall alters the nonradiation results by reducing the wall temperature by as much as 50 percent.

Continuous Operation of 1.0-μm-Wavelength $GaAs_{1-z}Sb_z/Al_yGa_{1-y}As_{1-z}Sb_z$ Double-Heterostructure Injection Lasers at Room Temperature. R. E. Nahory, M. A. Pollack, E. D. Beebe, J. C. DeWinter, and R. W. Dixon, Appl. Phys. Lett., *28* (January 1, 1976), pp. 19–21. Double-heterostructure $GaAs_{1-z}Sb_z/Al_yGa_{1-y}As_{1-z}Sb_z$ injection lasers have been operated continuously at room temperature for the first time. Emission was near 1.0 μm. The lowest threshold current density observed was 2.1 kA cm^{-2} dc.

Effects of Buffer Gases on Optically Pumped CH_3F FIR Laser. T. Y. Chang and C. Lin, J. Opt. Soc. Amer., *66*, No. 4 (April 1976), pp. 362–369. The effects of buffer gases on the performance of a 496-μm, optically pumped CH_3F laser are studied both experimentally and theoretically. A 55-percent increase in output power can be obtained by adding *n*-hexane vapor to an equal amount of CH_3F.

4F Virtual Bound State Formation in $CeAl_3$ at Low Temperatures. K. Andres, J. E. Graebner, and H. R. Ott, Phys. Rev. Letters, *35* (December 29, 1975), pp. 1779–1782. Specific-heat and electrical resistivity measurements in $CeAl_3$ below 0.2 K reveal enormous magnitudes of the linear specific-heat term $C = \gamma T$ ($\gamma = 1620$ m/mole K^2) and the T^2 term in $\rho = AT^2$ ($A = 35$ μΩ cm/K^2). We conclude that the $4f$ electrons

obey Fermi statistics at low temperature because of the formation of virtual bound $4f$ states.

Laser Action at 12.812 μm in Optically Pumped NH_3. T. Y. Chang and J. D. McGee, Appl. Phys. Letters, *28*, No. 9 (May 1, 1976), pp. 499–501. Optical pumping of the aR(6,0) line of the ν_2 fundamental vibrational band of NH_3 has led to laser action on the aP(8,0) line at 12.812 μm of the same vibrational band. A 5-kW pulsed output has been obtained by using 1.5 MW of pump power at 9.294 μm from a CO_2 laser.

Modulation Spectroscopy at Non-Normal Incidence With Emphasis on the Vacuum-uv Spectral Region. D. E. Aspnes, C. G. Olson,* and D. W. Lynch,* J. Appl. Phys., *47* (February 1976), pp. 602–607. Expressions are given to analyze modulation spectra taken at non-normal incidence. These expressions are used to determine the optimum angle of incidence to maximize the signal-to-noise ratio. Significant improvements are shown to be obtained in the vacuum-uv spectral region by making measurements at relatively large angles of incidence. * Iowa State University.

New Nanosecond Continuum for Excited-State Spectroscopy. C. Lin and R. H. Stolen, Appl. Phys. Lett., *28* (February 15, 1976), pp. 216–218. A new nanosecond continuum is generated by nonlinear optical processes in fiber waveguides pumped with a 20-kW 10-ns dye-laser pulse of broad spectral width. The continuum bandwidth is several thousand cm^{-1} in the visible with a total power ~1 kW. This continuum is useful for nanosecond time-resolved excited-state spectroscopy.

Strength of 0.04-50-m Lengths of Coated Fused Silica Fibers. C. R. Kurkjian, R. V. Albarino, J. T. Krause, H. N. Vazirani, F. V. DiMarcello, S. Torza, and H. Schonhorn, Appl. Phys. Lett., *28*, No. 10 (May 15, 1976), pp. 588–590. Tensile strength measurements have been made on coated fused silica fibers at gage lengths up to 50 m. At gage lengths between 0.04 and 10 m, the average strength is essentially constant at about 5 GN/m^2 (700 ksi). At gage lengths greater than 20 m the length dependence becomes important and by 50 m the strength has decreased to about 2 GN/m^2 (300 ksi). The minimum strength recorded in the testing of samples taken continuously from a length of 1031.6 m was 0.43 GN/m^2 (64 ksi). A "weakest link" model appears to be obeyed.

Virtual Bound States of Pd in Cu, Ag, and Au, and of Pt in Ag. S. Hüfner, G. K. Wertheim, and J. H. Wernick, Solid State Commun., *14* (December 15, 1975), pp. 1585–1590. The positions and widths of the virtual bound states of Pd in Cu, Ag, and Au and of Pt in Ag have been measured by XPS. The spin–orbit splitting of the Pt state in Ag is comparable to the spectroscopic atomic value. The host lattice d-band structure is perturbed in the alloys.

SYSTEMS ENGINEERING AND OPERATIONAL RESEARCH

Combined Primal-Dual and Penalty Methods for Convex Programming. B. W. Kort and D. P. Bertsekas, Siam J. Contr. Optim., *14* (February 1976), pp. 268–294. We propose and analyze a class of combined primal-dual and penalty methods for constrained minimization which generalizes the method of multipliers. We provide convergence and rate-of-convergence analysis for these methods for the case of a convex programming problem. We prove global convergence in the presence of both exact and inexact unconstrained minimization, and we show that the rate of convergence may be linear or superlinear with arbitrary Q-order of convergence, depending on the problem at hand and the form of the penalty function employed.